

UNIVERSITY OF NAPLES FEDERICO II

**DOCTORATE IN
MOLECULAR MEDICINE AND MEDICAL
BIOTECHNOLOGY**

XXXV CYCLE



**The role of NSP6 in the biogenesis of the SARS-CoV-2
replication organelle**

Tutor

Prof.ssa Maria Antonietta De Matteis

Candidate

Simona Ricciardi

2019-2023

Summary

Abstract	4
1. Background	6
1.1 COVID-19	6
1.1.1 Coronavirus pandemics	6
1.2 SARS-CoV-2 and its variants	8
1.2.1 SARS-CoV-2 emerging variants	8
1.2.2 SARS-CoV-2 genome	9
1.3 SARS-CoV-2 life cycle	11
1.3.1 Entry	12
1.3.2 Replication and transcription	16
1.3.3 Viral packaging and egress	20
1.3.3.1 N protein	20
1.3.3.2 M protein	21
1.3.3.3 E protein	22
1.3.4 The assembly and release of viral particles	23
1.4 Replication Organelle (RO)	25
1.4.1 RO in positive stranded RNA viruses	25
1.4.2 SARS-CoV2 RO ultrastructure	27
1.4.2.1 DMV biogenesis	28
1.4.2.2 The Role of non-structural proteins in DMV biogenesis	30
1.4.2.2.1 NSP3	30
1.4.2.2.2 NSP4	30
1.4.2.2.3 NSP6	31
2. Aims	33
3. Methods and statistics	34
3.1 Reagents and antibodies	34
3.2 Plasmid constructs	35
3.2 Cell culture, transfection, and RNA interference	37
3.3 Generation of HeLa Flag–NSP6 and HA–NSP6 doxycycline-inducible stable lines	37
3.4 SARS-CoV-2 infection and assays	37
3.5 Drug treatments	38
3.6 Western blot analysis	39
3.7 Immunofluorescence analysis	39
3.8 Confocal microscopy and image analyses	40
3.9 Quantification of the number and area of structures	40

3.10 Distribution of NSP4 puncta	40
3.11 Relative distribution of the NSP6 protein.....	41
3.12 Recruitment to NSP6 structures.....	41
3.13 Co-localization between NSP6 and DFCP1	41
3.14 Distance between particles	41
3.15 Measurements of NSP6 fluorescence intensity	41
3.16 CLEM.....	42
3.17 Electron tomography.....	43
3.18 EM quantification	43
3.19 NSP6 protein topology.....	43
3.20 Phylogenetic analysis.....	44
3.21 Statistics and reproducibility	44
4. Results	45
4.1 NSP6 promotes the formation of roundish structures.....	45
4.2 NSP6 induces ER zippering	47
4.3 NSP6 structures are selectively accessible to proteins and lipids	49
4.4 NSP6 homodimers zipper ER membranes.....	51
4.5 K22 interferes with the zipping activity of NSP6	56
4.6 NSP6(Δ SGF) has a higher ER-zippering activity	57
4.7 NSP6 connects DMVs with the ER	62
4.8 NSP6 organizes the DMVs cluster	66
4.9 K22 blunts the activity of NSP6 on DMVs and interferes with SARS-CoV-2 replication.....	70
4.10 NSP6 (Δ SGF) exerts more organization on DMVs than the reference one	73
4.11 NSP6 mediates replication organelle–LD association	75
4.12 DFCP1 tethers LDs to the ROLS compartment	77
4.13 DFCP1 recruitment to NSP6 structures is independent of PtdIns3P	79
4.14 LDs fuel SARS-CoV-2 replication via the NSP6 protein	81
5. Discussion	83
6. Conclusion	91
7. List of publications:.....	93
8. Bibliography.....	93
9. List of tables and figures.....	103

Abstract

Coronavirus disease 2019 (COVID-19) is caused by severe acute respiratory syndrome coronavirus 2 (SARS-CoV-2). Like other coronaviruses, it is an enveloped virus with a large (about 30kb) single-stranded positive RNA genome. An important feature of viruses belonging to this family is the expression of a surface protein called Spike, which is responsible for receptor binding and membrane fusion. Specifically, SARS-CoV-2 Spike protein binds, via its S1 domain, the angiotensin-converting enzyme 2 (ACE2) on host cells, promoting infection. Subsequent proteolytic cleavage of the S2' site of Spike, operated by the TMPRSS2 (transmembrane protein serine 2) protease located in the plasma membrane, leads to its activation, i.e., exposure of the fusogenic peptide, resulting in fusion of the virus membrane with the host plasma membrane. Alternatively, in case that target cells do not express TMPRSS2, the virus can be internalized via endocytosis and activated in endosomes, where cathepsins cleave the S2' site and promote the fusion of the viral membrane with the endosomal membrane. Upon fusion, SARS-CoV-2 releases its genome into the cytoplasm of the host cells to be translated to generate all the proteins that allow its replication. Two-thirds of human coronaviruses genome translates for two overlapping open reading frames (ORF1a and ORF1b), which generate two polyproteins (pp1a and pp1ab) to generate all the components needed for the replication. The polyproteins are then further processed by two viral proteases to generate 16 nonstructural proteins (nsp1-16), which are involved in different stages of the replication cycle. Of these, the nonstructural membrane proteins NSP3, NSP4, and NSP6, have been shown to play critical roles in cell membrane rearrangement, promoting the formation of replication organelles (ROs). In this compartment, viral RNA synthesis occurs. Many aspects of this process are still unclear, mainly how SARS-CoV-2 can use the cellular machinery to perform its functions.

Therefore, we analyzed the process of RO biogenesis by expressing NSP3, NSP4, and NSP6 proteins alone or in combination. In particular, while the role in the formation of DMVs has been reported for NSP3 and NSP4, we focused on analyzing the unidentified role of NSP6.

To monitor the formation of ROs, we exploited advanced microscopy techniques such as electron microscopy (EM), immuno-EM (IEM), and correlated light electron microscopy (CLEM) that allowed us to dissect the structural features of ROs. The NSP6-induced structures are composed by zippered ER with no luminal space .

Electron microscopy analysis of SARS-CoV-2-infected cells showed structures similar to those observed expressing NSP3, NSP4, and NSP6 proteins, confirming the relevance of our observations obtained with recombinant viral proteins.

Furthermore, FRAP analysis experiments on NSP6 transfected cells, determined this compartment as a molecular filter, accessible only to membrane proteins with small luminal tracts and especially lipids, that support replicative niche formation. The amphipathic tail of NSP6 could play the leading role in contacting LDs and bringing them closer to ROs. The zippering activity of NSP6 was associated with the ability of the protein to homodimerize, analyzed by immunoprecipitation experiments. The higher the homodimerization efficiency, the higher the zippering activity, as we found in the NSP6(Δ SGF). Interestingly, by interfering with the formation of NSP6 structures using K22 compound, DMVs results altered , both on transfected and infected cells.

In conclusion, we unveiled NSP6 as a key player during the ROs formation that could be targeted to identify novel treatments for COVID-19 disease.

1. Background

1.1 COVID-19

1.1.1 Coronavirus pandemics

Coronaviruses are large, positive-stranded, enveloped RNA viruses belonging to Nidovirales. The Nidovirales can be divided into three families: *Arteriviridae*, *Roniviridae*, and *Coronaviridae*. The last includes the *Toroviridae* and *Coronaviridae*. The *Coronaviridae* (called CoVs) are divided into 4 genera: alpha, beta, delta, and gamma (ICTV Virus Taxonomy: 2019 Release). Among them, CoV alpha and beta are known to infect humans¹. In particular, four HCoV strains (HCoV 229E, NL63, OC43, and HKU1) are known to be endemic globally and are responsible for 10-30% of upper respiratory tract infections in adults, generally causing mild upper respiratory illness²³. However, in the past two decades, spillover events, which cause a switch from a reservoir species to a new host species, have led to the emergence of as many as three highly pathogenic Coronaviruses in the human population that can cause severe respiratory illness: Severe Acute Respiratory Syndrome Coronavirus (SARS-CoV), which emerged in 2002, Middle East Respiratory Syndrome coronavirus (MERS-CoV), which appeared in 2011, and the most recent, Severe Acute Respiratory Syndrome coronavirus 2 (SARS-CoV-2), which emerged in 2019⁴. Unfortunately, nearly 20 years later, the factors associated with animal-to-human transmission remain poorly understood. The spread of SARS-CoV, associated with droplet exchange, showed low infection efficiency and high viral load required for transmission⁵. Symptoms encountered were fever, cough, dyspnea, and occasionally watery diarrhea. Mechanical ventilation was required in 20-30% of cases, and 10% died, with higher mortality rates in elderly patients

and those with medical comorbidities⁵. The only measure to contain the spread of SARS was a strict quarantine, as no vaccine was available. Unlike SARS-CoV, MERS was characterized by sporadic zoonotic transmission and limited human spread. Subsequently, it spread worldwide, mainly to 27 countries, showing a higher mortality rate (34%) than SARS-CoV. Related symptoms were much more severe than those observed for SARS, with prominent gastrointestinal symptoms and often acute renal failure. In 2017, SARS-CoV and MERS-CoV were listed as priority pathogens by the World Health Organization (WHO) to stimulate research and development of countermeasures against CoVs. After only two years, on December 31, 2019, cases of pneumonia were reported in Wuhan, China. The rapid spread and transmission of Coronavirus Disease-19 (COVID-19) among the global population has reached pandemic proportions affecting all continents. On March 11, 2020, the epidemic was declared a global pandemic.

Phylogenetic analysis of SARS-CoV-2 demonstrated that it belongs to the genera Betacoronavirus, subgenus Sarbecovirus⁶. Initial investigations showed that the sequence shares 79.6 % similarity with SARS-CoV and 50 % identity with the sequences of MERS-CoV⁷. Regarding the origin of MERS-CoV and SARS-CoV, it is hypothesized that they may have been derived from bats and were later associated with dromedary camels and palm civets, respectively, as intermediate hosts^{8,9}. The genome of SARS-CoV-2 shows a whole-genome similarity of 96.2% with a bat Coronavirus, BatCoV RaTG13¹⁰. Despite this, it has been suggested that the spread of BatCoV in humans may have been facilitated by the help of an intermediate host, and pangolins seem to be good candidate¹¹.

The observed mortality rate for SARS-CoV-2 appears to be lower than for SARS-CoV and MERS-CoV. Reported symptoms range from mild (chills, fever, cough, sore throat, loss of taste and smell, nausea, and diarrhea) to severe (dyspnea, chest pain, and, in some cases, even acute respiratory distress

syndrome - ARDS) to multi-organ failure in the most critical cases. Patients show an incubation period of 1 to 14 days, followed by a symptomatic phase of 7 to 14 days. Severe manifestations of the disease may occur in patients with other reported conditions, such as diabetes, heart disease, or chronic lung inflammation¹².

1.2 SARS-CoV-2 and its variants

1.2.1 SARS-CoV-2 emerging variants

Since the beginning of the pandemic, numerous mutations have been reported in the genome of SARS-CoV-2. SARS-CoV-2, like all members of the *Coronaviridae* family, has a single-stranded positive viral genome between 27 and 32 kb in length that is subsequently translated into large polyproteins, which are cleaved into viral proteins^{13, 7}. Interestingly, RNA viruses generally mutate rapidly due to the lack of correction activity during their replication cycle^{14,15}. Unlike other RNA viruses, Coronaviruses rarely acquire mutations because they have a correction mechanism mediated by the 3'-5' proofreading exoribonuclease NSP14 through its N-terminal domain¹⁶. The sequences of SARS-CoV-2 variants have been phylogenetically organized into clades and genetic lineages. Hence, the same viral variant is described by different names and mapped by software such as GISAID (Global Initiative on Sharing Avian Influenza Data), NEXTSTRAIN (an open-source project created to update publicly available pathogen genome data constantly), and PANGO (Phylogenetic assignment of the named global epidemic); recently WHO decided to label variants that follow the Greek alphabet.

In general, based on the severity that each viral variant presents to the population, this classification was drawn up by the Center for Disease Control and Prevention (CDC)¹⁷:

- Variants of Interest (VOIs) are the variants that are predicted to generate an epidemiological advantage, but without any evidence (Table 1).

WHO label	Lineage	Country first detected	Year and month first detected
Omicron	BA.2.75	India	May 2022
Omicron	BQ.1	n/a	n/a

Table 1. Summary of VOIs described in the last year.

- Variants of concern (VOCs) are the variants for which there is evidence for an epidemiological advantage (Table 2).

WHO label	Lineage	Country first detected	Year and month first detected
Omicron	BA.2	South Africa	November 2021
Omicron	BA.4	South Africa	January 2022
Omicron	BA.5	South Africa	February 2022

Table 2. Summary of VOCs described in the last year.

- Variants of High Consequence, for which there is evidence that preventive medical countermeasures (MCMs) significantly reduce their effectiveness compared to other circulating variants.

1.2.2 SARS-CoV-2 genome

The genome contains a 3' untranslated region (UTR) replication and transcription complex (RTC) binding site, which is essential for replication and transcription of the negative-sense intermediate RNA (-RNA) and also a 5'-GGAAGAGC-3' octanucleotide sequence with unknown function, and a nonessential hypervariable region (HVR)¹⁸. It is assumed that the polyadenylation process of viral RNA is performed by NSP8, the viral adenylyltransferase, although there is no canonical sequence of the AAAAA polyadenylation signal. Instead, at the 5' UTR of the SARS-CoV-2 genome there are a 5'-leader 72 nt long, a basic transcriptional regulatory sequence (TRSL, ACGAAC), cis-elements involved in viral translation, subgenome synthesis, and viral genome packaging, and elements for resistance to viral mRNA degradation^{19,20}.

The first two-thirds of the viral genome codes for two open reading frames (ORF1a and -b), from which all non-structural viral proteins (NSPs) are derived^{21,22} (Figure 1).

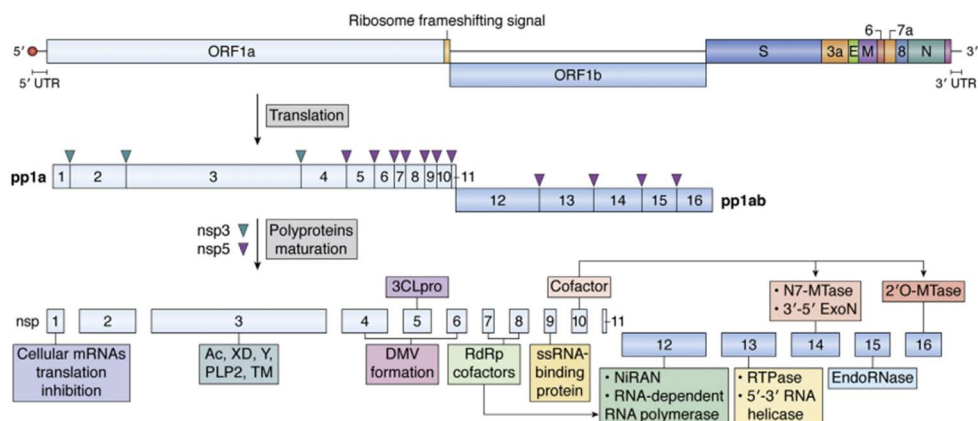


Figure 1. The RNA genome encodes NSPs, structural and accessory proteins. The nonstructural proteins are encoded by ORF1a and ORF1b. Cap-dependent translation begins at ORF1a and produces pp1a, formed by NSP1–11, or pp1ab, a more extended polypeptide that includes NSP12–16. The structural and accessory proteins are synthesized by translating their respective subgenomic mRNAs. Reprinted from “Replication of the coronavirus genome: A paradox among positive-strand RNA viruses”, Grellet et al., 2021, Journal of biological chemistry.

Specifically, the translation of ORF1a/b is subject to frameshift whereby it can produce either a shorter polyprotein (the 440-500-kDa pp1a, which includes NSPs 1-11) or a longer polyprotein (the 740-810-kDa pp1ab, which produces for NSPs 1-to-16), depending on the stop codon located in the overlap region between ORF1a and ORF1b²³. This is a highly controlled mechanism for producing the nonstructural proteins derived from ORF1a that perform their main primary action in preventing the initial immune response and act as cofactors in the replication and transcription processes to allow subsequent replication and transcription by ORF1b-encoded proteins. The proteolytic process of pp1a and pp1ab is required for the release of individual nonstructural proteins, which is carried out by NSP3, which contains a papain-like protease (PLpro) that catalyzes the proteolytic cleavage of NSPs upstream of NSP4; and NSP5 which contains a cysteine protease similar to chymotrypsin (3CLpro), which is considered the main protease and catalyzes the proteolytic cleavage of all NSPs downstream of NSP4 (Figure 1)²⁴. In addition to participating in the replication process, NSPs play an important role in generating the replicative compartment in which replication occurs. See the following section "Biogenesis of DMVs."

The genome also codes for structural proteins (S, E, M, and N) involved in virion formation and for accessory proteins (3a, 6, 7a, 7b, 8, and 9b) some of which are predicted to have anti-IFN activity²⁵.

How SARS-CoV-2 hijacks the host translation machinery to produce viral proteins remains largely unexplored.

1.3 SARS-CoV-2 life cycle

Nonstructural, structural, and accessory proteins control the life cycle of SARS-CoV-2 in host cells: Entry, Replication, Assembly and Egress (Figure 2).

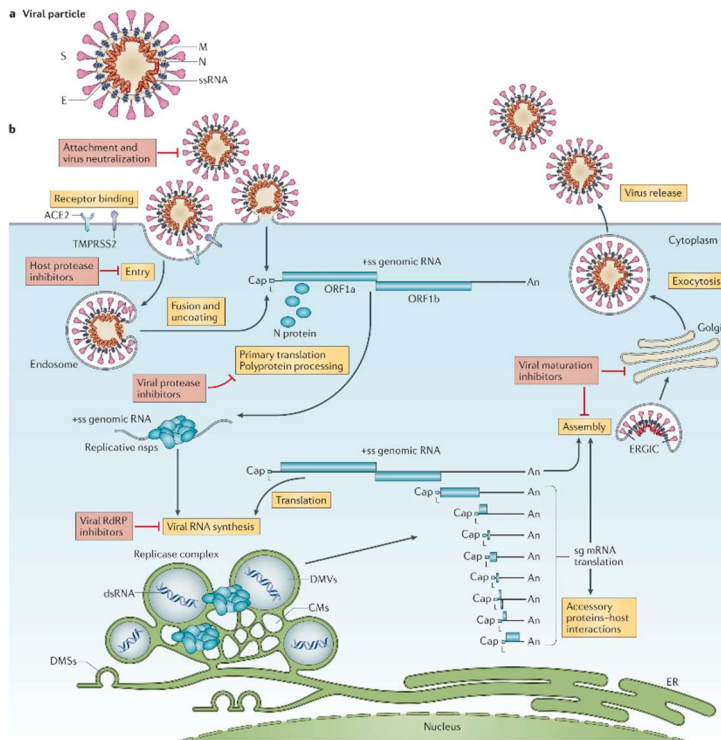


Figure 2. Schematic representation of SARS-CoV2 life cycle: Entry, Replication, Assembly and Egress. A, The coronavirus virion is composed of structural proteins: spike (S), envelope (E), membrane (M), nucleocapsid (N). Inside the capsid is located the single-stranded positive RNA genome. B, Entry is mediated by S interactions with cellular receptors such as angiotensin-converting enzyme 2 (ACE2), together with host factors (such as the cell surface serine protease TMPRSS2) or through the endosomal pathway. Once entered, the genome is released into the cytosol and genomic RNA is immediately translated into ORF1a and ORF1b from which the polyproteins pp1a and pp1ab are derived. Pp1a and pp1ab are processed into the individual nonstructural proteins (NSPs) that form the viral replication and transcription complex. The nsps direct the biogenesis of the viral replication organelles, the double membrane vesicles (DMVs). The translated structural proteins translocate to the ER-Golgi intermediate compartment (ERGIC), where RNA is encapsidated within the virion. Finally, virions are secreted from the infected cell by exocytosis. Reprinted from the "Coronavirus biology and replication: implications for SARS-CoV-2", V'kovski et al., 2020, nature reviews microbiology.

1.3.1 Entry

As previously mentioned, the SARS-CoV-2 genome is an approximately 30 kb (+) single-strand genome coated with nucleocapsid protein (N), which encloses and protects the viral genome. The high helical symmetry of the nucleocapsid protein makes it very flexible²⁶. Nucleocapsid is surrounded by lipid bilayer containing the three membrane proteins spike (S), membrane (M), and envelope (E), to form the viral particles. SARS-CoV-2 viral infectious particles can be spherical and pleomorphic, with a size of approximately 100 nm.

The virion envelope is enriched with Spike (S) proteins organized in trimers, giving the virion a characteristic bulb shape reminiscent of a solar crown-like appearance for which scientists have coined the name 'Coronavirus'²⁷.

The trimeric glycoprotein S is involved in host tropism, receptor binding, membrane fusion, and the induction of antibodies.

Each subunit of S consists of two domains, S1 and S2. S1 contains the N-terminal domain (NTD) and the receptor binding domain (RBD) and promotes binding to the host cell receptor. Differently, the S2 subunit is composed of the fusion-peptide (FP), the heptad repeat 1 (HR1), the central helix (CH), the connector domain (CD), the heptad repeat 2 (HR2), the transmembrane motif (TM) and the cytoplasmic tail (CT), and mediates membrane fusion to allow the virus to enter the host's cytoplasm (Figure 3). For entry to occur, the S protein fusion activity must be activated through a complex process that requires proteolytic cleavage at two sites. The first cleavage site, a short polybasic sequence (RRAR), is located at the S1/S2 boundary and leads to conformational changes in the S2 domain, placing the S1/S2 site in the prefusion conformation. The second cleavage site is located within the S2 domain (S2') before the fusion peptide (FP), which drives the fusion of viral and cell membranes to release the N-coated RNA genome into the cytoplasm.

The S protein recognizes ACE2, angiotensin converting enzyme-2 receptor. Recognition of ACE2 is mediated by the RBD sequence, which differs from that of SARS-CoV (Y442, L443, L472, N479, T487) by 5 crucial residues (L455, F456, F486, Q493, N501) in SARS-CoV-2 that increase its affinity for the

receptor. Notably, the RBD contains five antiparallel β -sheets that assemble to form the core. The receptor binding motif (RBM) is located between the β 4 and β 7 filaments, acting as a crucial element for binding to ACE2.

ACE2 is expressed in most organs, particularly lung and small intestinal epithelia. A cell surface peptidase hydrolyzes angiotensin II, the central player in the renin-angiotensin-aldosterone system (RAAS).

Once the S protein binds the ACE2 receptor, it is cleaved by the host cell surface transmembrane serine protease (Furin) at the S1/S2 and (TMPRSS2) at S2' sites, promoting structural changes of the S protein and its subsequent exposure of the fusion peptide (FP) (Figure 3)²⁸.

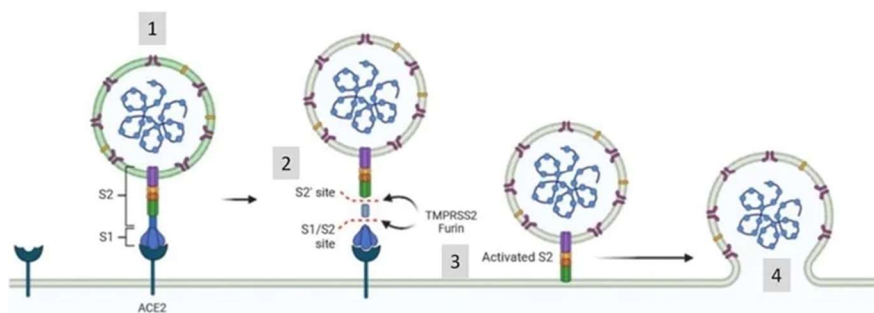


Figure 3. SARS-CoV-2 Spike protein binds to the angiotensin-converting enzyme 2 (ACE2) to enter target cells. After receptor binding (1), the virus S protein is cleaved by proteases such as furin/TMPRSS2 into S1 and S2 subunits (2) that mediates S2-assisted fusion (3) and the release of the viral genome (4)—reprinted from “In silico investigation of the new UK (B.1.1.7) and South African (501Y.V2) SARS-CoV-2 variants with a focus at the ACE2-Spike RBD interface”, by Villoutreix et al., 2021, International Journal of Molecular Sciences.

The cleavage of S protein by furin-like proteases leads to the formation of its pre-fusion conformation. The pre-fusion form of the S protein comprises three receptor binding domains (RBDs) surrounded by three copies of the N-terminal domain.

The prefusion conformation involves the exposure of the receptor binding domain (RBD), which is located above the fusion core formed by Spike trimers. In the closed prefusion conformation all three copies of the RBD occlude the receptor binding site, while in the open prefusion conformation one or more RBDs are raised to expose the receptor binding site. Once receptor binding has

occurred, it switches from the prefusion conformation to the post fusion conformation, where the fusion peptide and the transmembrane domain of ACE2 come together (Figure 4)²⁹.

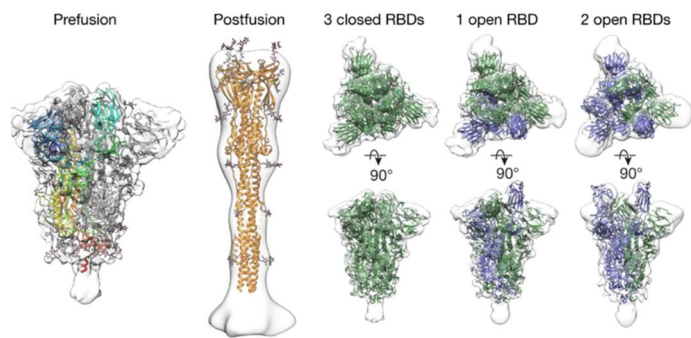


Figure 3. Structures of pre-fusion and post-fusion trimers of the S protein. (b) Possible conformations of the pre-fusion trimer. It is reprinted from "Structures and distributions of SARS-CoV-2 spike proteins on intact virions", by Ke, Z., et al., 2020, Nature, 588, 498–502.

Alternatively, the second virus entry mechanism into the host cell occurs through the endosomal pathway. In this case, the S2' cleavage of the S protein is carried out by endosomal "cathepsin" proteases. The S protein contains amino acid sequences susceptible to cleavage by cathepsins B, K, L, S, and V, which mediate the fusion of the viral envelope with the endosomal membrane³⁰. In either case, through the fusion of the plasma membrane or endosome, the viral RNA genome is released once the viral nucleocapsid enters the cytoplasm (Figure 5).

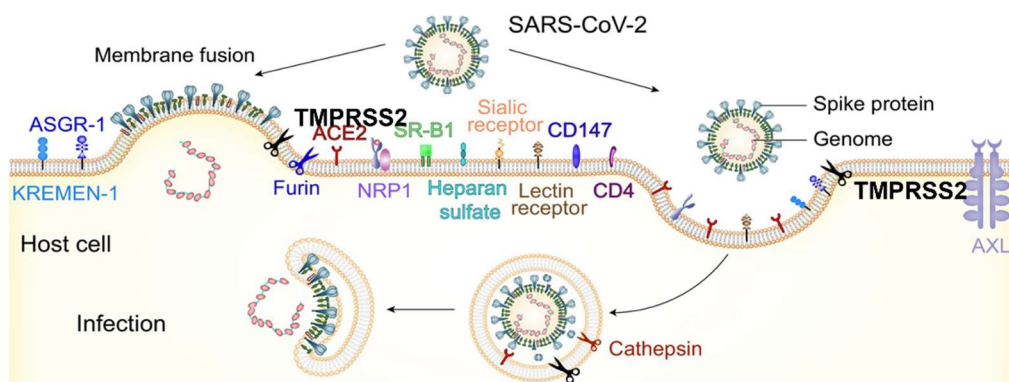


Figure 5. Entry of SARS-CoV-2. Membrane fusion, upon binding to the host cell receptor ACE2, the SARS-CoV-2 spike protein can be cleaved at the S1/S2 site by furin, which leads to conformational changes that expose the S2' site for cleavage by TMPRSS2, that results in viral-human cell fusion at the plasma

membrane. Endocytosis, if separation of both sites does not occur at the cell surface after receptor binding, the virion may be endocytosed. Cathepsins within the endosome or lysosome can then cleave the spike protein to activate the spike protein and, then, the membrane fusion. Reprinted from "Cell entry by SARS-CoV-2", by Peng et al., 2021, Trends in Biochemical Sciences.

1.3.2 Replication and transcription

The NSPs are involved in the formation of replication and transcription complexes (RTCs)³¹. Coronavirus genome replication synthesizes the negative-strand RNA, which becomes a template for generating positive-strand genomes that are subsequently packaged into virions.

Negative-strand synthesis is aided by the interaction of the N protein with the poly(A) tail and the 5' end of the genome to bring these elements closer³². RTCs are also involved in the synthesis of subgenomic mRNAs (sg mRNAs), which encode for ORFs located at the 3' end of the genome.

Specifically, sg mRNAs arise from the 5' end of the viral genome and inherit the same 5' leader sequence through a discontinuous transcription mechanism (Figure 6).

During negative-strand synthesis, the RNA-dependent RNA polymerase (RdRp) may stop at specific regions called transcription regulatory sequences (TRS), causing early termination of RNA synthesis. TRS regulatory elements are located downstream of the leader sequence at the 5' end of the genome (TRS-L) and at the 5' end of each viral ORF (TRS-B), except for ORF1a and ORF1b. The RdRp complex, once transcription is initiated at the 3' end of the positive-sense genome, copies the TRS-B sequences and can jump from a given TRS-B to TRS-L on the nascent sgRNA at the 5' end of the genome, thus allowing transcription of the 5'-terminal leader sequence and generation of a shorter sg negative strand, which is used to generate positive-stranded sg mRNA (Figure 6).

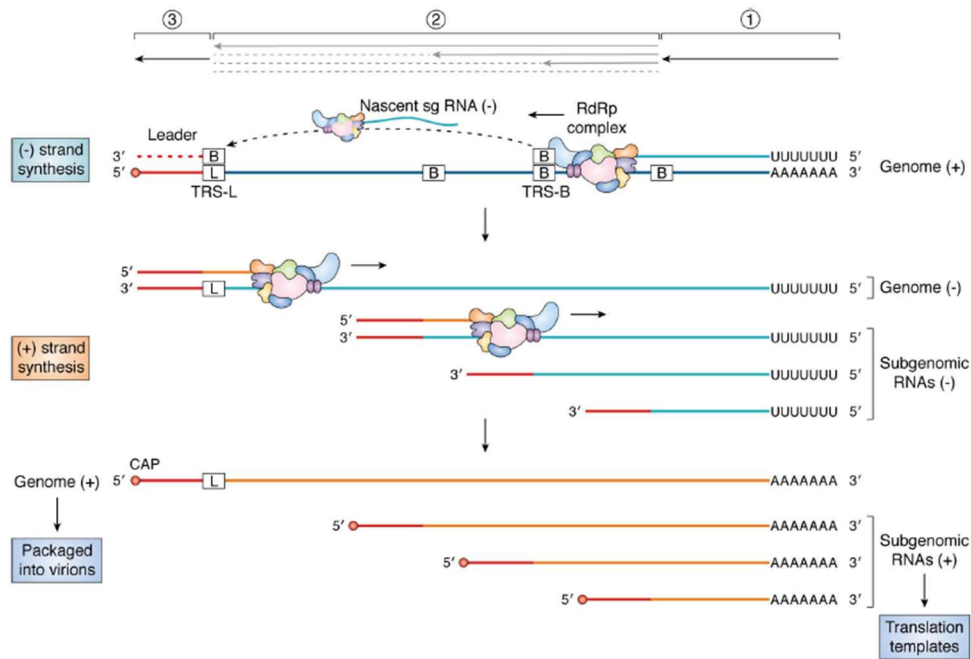


Figure 6. Discontinuous transcription. The RdRp complex initiates transcription at the 3' end of the positive-sense genome (1). Upon copying the TRS-B sequence (2), the RdRp complex may "jump" to the TRS-L sequence (3) owing to the complementarity between the TRS-B sequence on the nascent sg RNA and the end TRS-L sequence on the genome. Transcription is resumed on the new template, and the leader sequence (shown in red) is copied to complete the negative-strand sg RNA. The RdRp complex does not always switch templates at TRS-B sequences, resulting in the synthesis of genome-length negative-strand RNA. The negative-strand RNAs serve as templates for synthesizing genome-length positive-strand RNAs or sg mRNAs. Reprinted from "The molecular virology of coronaviruses" by Hartenian et al., 2020, JCB Review.

Coronavirus replication, transcription, and processing steps during infection are mediated by the replication complex.

For many RNA viruses, replication depends mainly on RdRp activity and a small number of cofactors. In contrast, coronaviruses use a multiprotein complex, which involves an RdRp (NSP12), viral cofactors (NSP7-8), a helicase (NSP13), a single-strand binding protein (NSP9), a correction exonuclease (NSP14), other cofactors (NSP10), and capping enzymes (NSP16) (Figure 7).

The binding of NSP8 facilitates the interaction of the NSP12-NSP7-NSP8 complex in binding RNA to NSP12 either as a single protein or as a heterodimer (NSP7-NSP8).

NSP8 has polyadenylation activity but cannot incorporate other nucleotides on heteropolymer templates, suggesting that it may not be a primase. In the RTC,

NSP8 interacts with NSP9, a single-stranded nucleic acid (ss) binding protein whose function is not yet known, probably to protect the viral genome from cellular nucleases. The RTC also consists of NSP13, a 5' → 3' helicase that interacts with NSP12 and various other components. In addition, NSP13 also possesses 5'-triphosphatase activity, suggesting a role in RNA capping³³.

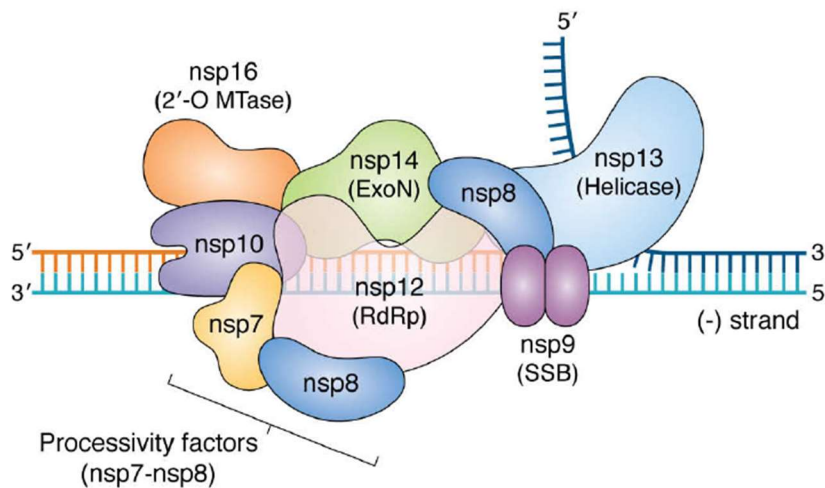


Figure 7. Shown is a model of how the different proteins in the coronavirus replisome come together on the viral negative-strand while synthesizing the positive-strand RNA. The core replicase is predicted to consist of the RdRp (NSP12), processivity factors (NSP7-8), and ExoN complex (NSP14, NSP10). The helicase is shown to be unwinding the dsRNA ahead of the replisome, and the SSB (NSP9) is shown as a dimer protecting single-stranded regions of the RNA. The 2'-O-MTase (NSP16), which is predicted to be involved in RNA capping, is also indicated. Reprinted from "The molecular virology of coronaviruses" by Hartenian et al., 2020, JCB Review.

As we have seen, the coronavirus genome encodes specialized mechanisms to contain the mutational load. Coronaviruses encode an NSP14 exonuclease that acts as a proofreader for high-fidelity replication and genome integrity.

As reported in the GISAID website, the mutation rates of SARS-CoV-2 are lower (10^{-7}) than in most RNA viruses (10^{-5}). Mutations at NSP14 alter the error rate, similar to that observed in other RNA viruses. NSP14 interacts with the tripartite NSP12-NSP8-NSP7 complex, reflecting its role in proofreading during transcription/replication. NSP10 is part of the exonuclease complex together with NSP14. Specifically, it participates in the catalytic activity of NSP14-ExoN to remove a mismatched nucleotide at the 3' end of the RNA. It also interacts

with NSP16 (2'-O-MTase, a potential RNA-modifying enzyme), which is predicted to be involved in RNA capping.

After transcription, all mRNAs produced are 5'-capped to assure viral mRNA stability, initiation of translation, and escape from the cellular innate immune system. Several enzymes are involved in RNA capping and are considered new attractive targets for novel antiviral drugs. Specifically: NSP13 acts as a 5'-triphosphatase removing the 5' γ -phosphate from the 5' nucleotide³⁴; NSP14 catalyzes the addition of a methyl group at the N7 position of the guanosine; NSP16 promotes the insertion of an additional methyl group at a 2'-O position on the ribose of the 5' nucleotide.

The first capping step begins with the hydrolysis of the γ -phosphate to the 5' end nucleotide by the NSP13 helicase. Subsequently, a guanosine monophosphate is added to the RNA diphosphate by a guanylyl transferase carried out by the NiRAN domain of NSP12. Then, guanosine is methylated at the N7 position, probably by the N7-methyltransferase (MTase) activity residing in the C-terminal part of NSP14. This step is essential to prevent recognition by the host antiviral mechanisms, which usually promote the degradation of uncapped RNA (recognized as "nonself" structures).

Finally, NSP16 methylates the first and second nucleotides at the 2'-O position on the ribose of the 5' nucleotide. The interaction between NSP16 and NSP10 improves RNA binding by NSP16³⁵ (Figure 8).

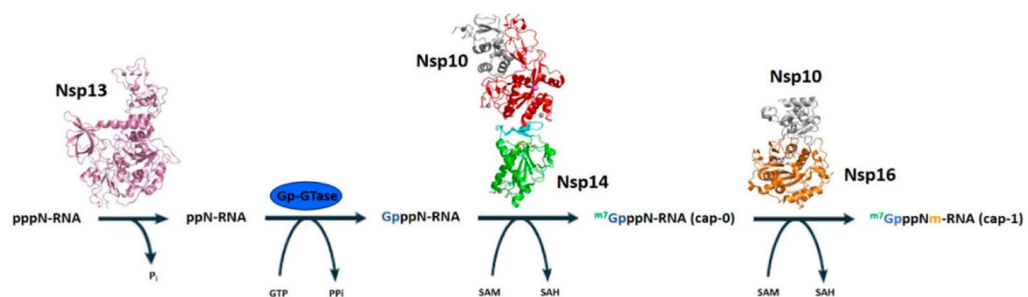


Figure 8. The sequential enzymatic action performed during viral mRNA 5' capping. NSP13 removes the 5' γ -phosphate from the 5' nucleotide generating the ppN-RNA; a GTase adds GMP to the 5'-terminus of ppN-RNA; NSP10 and NSP14 cooperate to add a methyl group to form the cap0 structure; NSP10 and

NSP16. Methyl donor group: S-adenosyl methionine (SAM). Reprinted from "A Structural View of SARS-CoV-2 RNA Replication Machinery: RNA Synthesis, Proofreading and Final Capping", Romano, M., et al., 2020, Cells, 9(5), 1267.

1.3.3 Viral packaging and egress

Viral packaging and egress involve several structural proteins that cooperate to keep the viral particles functional: Nucleocapsid (N), Membrane (M), Envelope (E), and Spike (S).

1.3.3.1 N protein

The Nucleocapsid protein (N) of SARS-CoV-2 is a 46 kDa monomeric protein composed of 419 amino acids; it is a cytosolic protein consisting of several domains: N-terminal region, which interacts with the viral RNA packaging signal, an RNA-binding region; a serine/arginine-rich region; a central region involved in phase separation; and the C-terminal region³⁶ (Figure 9).

Once the RNA is synthesized within the double membrane vesicles (DMVs, see below), it is immediately complexed by N. The N-RNA complex is organized into subcomplexes of about 12 N-proteins, surrounding about 800 nucleotides, forming a G-form known as ribonucleoproteins (RNPs)³⁷.

The central region of N and the RNA binding region are mainly involved in condensing N with viral RNA. In the presence of RNA, the N protein assembles into large oligomers, and these two regions play a central role in phase separation with viral RNA. This phenomenon is regulated by phosphorylation of the serine/arginine-rich region of N during the packaging process. The N-RNA complex undergoes this phase separation from liquid to gel condensates due to N-RNA interactions^{36,38}. Subsequently, N interacts with the membrane protein M. On the one hand, N-RNA forms the liquid condensate; on the other hand, the

interaction of N with M promotes incorporation into the particles forming the gel-like condensate, suggesting a dual role of the N protein³⁹.

1.3.3.2 M protein

M is a 222-amino acid glycoprotein of 25 kDa that localizes between the inner side of the envelope and the nucleocapsid.

Coronavirus M is a transmembrane protein that act as a "bridge" between the nucleocapsid and the lipid bilayer.

It is the most abundant structural protein. Its structure involves three transmembrane domains (TMDs), a short glycosylated N-terminal domain, and the C-terminal tail in the cytoplasm, also known as the endo-domain, which is located in the inner part of the virion (Figure 9).

The C-terminal domain of M is critical for particle formation⁴⁰. Experiments have shown that deletion of all domains except the C-terminal tail equally promotes vesicle release⁴¹.

The incorporation of the N-RNA complex into the particle is mediated by the direct involvement of the carboxyl and amino terminals of M and N rather than by the TMD or dimeric M-M interactions^{42, 43}.

Therefore, the interaction of RNA with M-N promotes the stability of the M tail by keeping the M protein in a favorable conformation, which is probably necessary to increase virion RNA genome stability and virion production^{44,45}.

When expressed alone, the M protein of SARS-CoV-2 localizes to the Golgi apparatus and along the secretory pathway⁴⁶. In the Golgi, the M protein can be N-glycosylated, as observed in infected cells⁴⁶. Since the assembly and packaging of viral particles occur in the ER-Golgi Intermediate Compartment (ERGIC), M protein may be transported into this compartment and assembled with E, N, and S. This step could be related to the role of the N-glycosylated form of M or exit from the Golgi through the secretory pathway.

1.3.3.3 E protein

SARS-CoV-2 E protein is a small transmembrane integral protein of about 8.4 kDa, composed of 75 amino acids. The protein structure consists of a short N-hydrophilic terminal domain, a large hydrophobic transmembrane domain containing an amphipathic alpha-helix involved in forming a conductive pore, and a C-terminal hydrophilic domain⁴⁷ (Figure 9). The E protein of SARS-CoV-2 is localized in the ERGIC apparatus and Golgi, both in cis and medial cisternae. Specifically, the N-terminus is oriented in the lumen of the ERGIC, and the C-terminus toward the cytosol.

Recent studies have shown that tagging the E protein at the C-terminus results in localization to the endoplasmic reticulum⁴⁸. This suggests that C-terminus may play a role in interacting with other structural proteins involved in virus assembly. One of the unique features of the coronavirus E protein is its ability to self-oligomerize to create a pentameric ion channel, making this protein a "viroporin"⁴⁹⁻⁵². TMDs are involved in ion channel formation because they are necessary for the oligomerization of E. The connections between E and M are considered crucial in viral particle formation. Specifically, the E protein interacts with M through its C-terminus^{43,44}. Still, the stability of this binding is related to ubiquitination changes at the N-terminus of M. Its C-terminus is also implicated in the binding of the N protein. Recently, it has been shown that the interaction between M and E increases the stability of M dimers by promoting better vesicle release⁴³. Optimal production of viral particles requires M, N, and E in the case of SARS-CoV and SARS-CoV-2 with or without S. Notably, while M and N are sufficient to form viral particles, the presence of E increases their production and release⁵³.

S has already been described in the section "Entry".

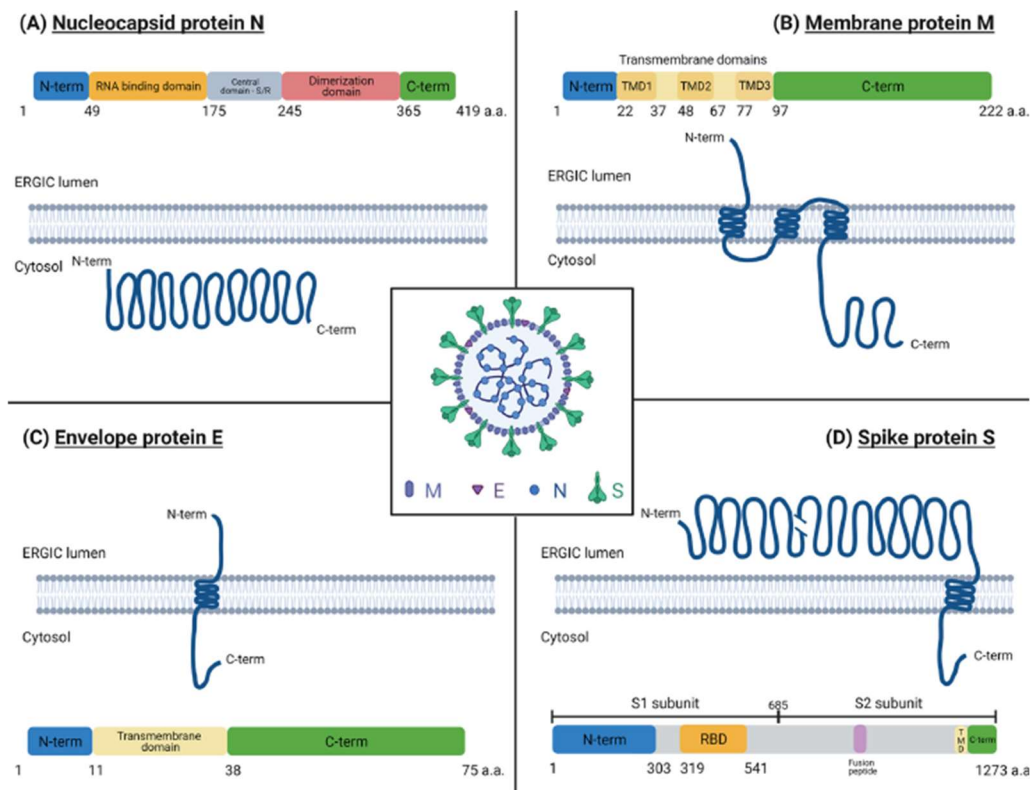


Figure 9. Schemes and membrane topology of the structural SARS-CoV-2 proteins nucleoprotein (N) (A), membrane (M) (B), viroporin envelope (E) (C), and spike (S). Reprinted from “Betacoronavirus Assembly: Clues and Perspectives for Elucidating SARS-CoV-2 Particle Formation and Egress” by Bracquemond et al., 2021, American Society for microbiology”.

1.3.4 The assembly and release of viral particles

Assembly is the process by which the viral RNA, wrapped in the nucleocapsid, joins the envelope to form a single viral particle.

Once viral structural glycoproteins M, E, and S are synthesized in the ER they move into the ERGIC where the assembly occurs.

N, along with viral RNA, is encapsulated in the forming virion in the membranes at the ERGIC, where the budding takes place.

In coronavirus infections, virion egress is still a poorly understood process. In particular, the cellular pathways that are used and the cellular co-factors that aid this process are not yet known.

Although there have been no extensive studies, it was initially hypothesized that Coronaviruses, similarly to other enveloped viruses, could follow the constitutive secretory pathway, Trans-Golgi-Network to PM, for exocytosis⁵⁴ (Figure 10, Route 1). This hypothesis was also supported by the observation of the progressive disruption of the Golgi structure during CoV infection⁵⁵.

In the work of Ghosh et al. (2020), a different egress mechanism from that observed for other +RNA genome viruses was reported. Specifically, virus particles assembled in the lumen of the ERGIC, trafficked to the TGN and subsequently to lysosomes. Exit would be favored by exocytic lysosomes to the PM. The process that promotes virion arrival at lysosomes is not established. Among the hypotheses, it could be a direct TGN-lysosome pathway via late endosomes/MVBs pathway, mediated by RAB7. Alternatively, retrograde transport could bring virions back from the TGN to the ER/ERGIC, from which they would traffic to lysosomes via late endosomes/MVBs⁵⁶ (Figure 10, Route 3). Differently, in the work of Saraste et al., 2019, an alternative mechanism is proposed involving the endosomal recycling system for egress in IBV coronavirus infection. Once assembly to the intermediate compartment is finished, RAB1-positive virions pass into less compact areas of the Golgi ribbon, through microtubules, and enter the endocytic recycling circuit to the plasma membrane (PM), which is regulated by Rab11⁵⁷ (Figure 10, Route 2).

As this remains a much-debated process for SARS-CoV2 infection, future work should serve to elucidate these aspects and discriminate whether there is a single egress pathway or whether several may exist.

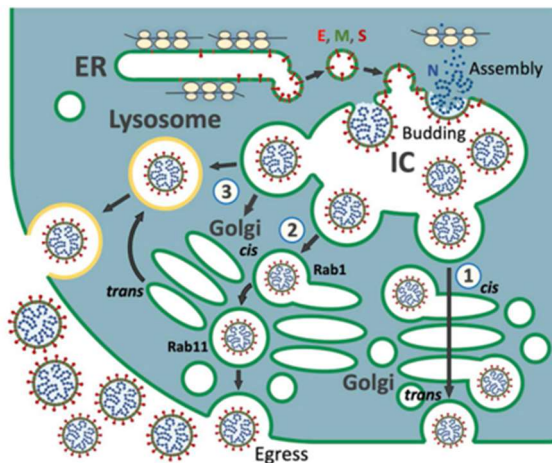


Figure 10. Egress of the CoV viral particles. Lower panel: After the replication of mRNAs in the DMVs, viral structural proteins mediate the formation of viral-like particles (VLP). Vesicle accumulation occurs at the intermediate compartment membranes and then is released to the extracellular space via 3 different routes. Reprinted from "The life cycle and enigmatic egress of coronaviruses", by Prydz et al., 2022, Molecular Microbiology.

1.4 Replication Organelle (RO)

1.4.1 RO in positive stranded RNA viruses

All positive-stranded RNA viruses induce significant rearrangement of host cell membranes to support every step of their life cycle. In particular, this process aims to create a safe microenvironment where the most delicate stages of replication can be carried out⁵⁸. Indeed, viral replication occurs in specific unique structures termed viral replication organelles (vROs) necessary to: concentrate viral replicase and associated host proteins and viral RNAs; to regulate the enzymatic activities and the replication process in space and time, protect viral RNAs from recognition and degradation by the host's innate immune defense. Thus, during infection, the RO becomes the niche where the genome can replicate safely. ROs are generated by several host cell membranous organelles, including the endoplasmic reticulum (ER), Golgi apparatus, mitochondria, lysosomes, and plasma membrane.

Among the + strand RNA viruses, many promote single-membrane vesicles (SMVs) as their RO, which consist of invaginated or evaginated spherules (about 50-200 nm in diameter) in the membranes of different organelles⁵⁹⁻⁶¹ (Figure 11A). These structures include a small pocket with a neck opening that would allow import and export of material with the cytosol. In this regard, the three-dimensional structure of ROs in flaviviruses has been solved by EM techniques. In the work of Welsch et al. (2009), it was shown that the replication compartment of DENV consists of 80-90 nm invaginated SMVs in the ER lumen. The SMVs structures can often be organized into clusters called vesicle packets (VPs).

Other single-strand positive RNA viruses, including Coronaviruses, promote RO formation as Double Membrane Vesicles⁶²⁻⁶⁴ (Figure 11B). (See the “The DMVs biogenesis” section).

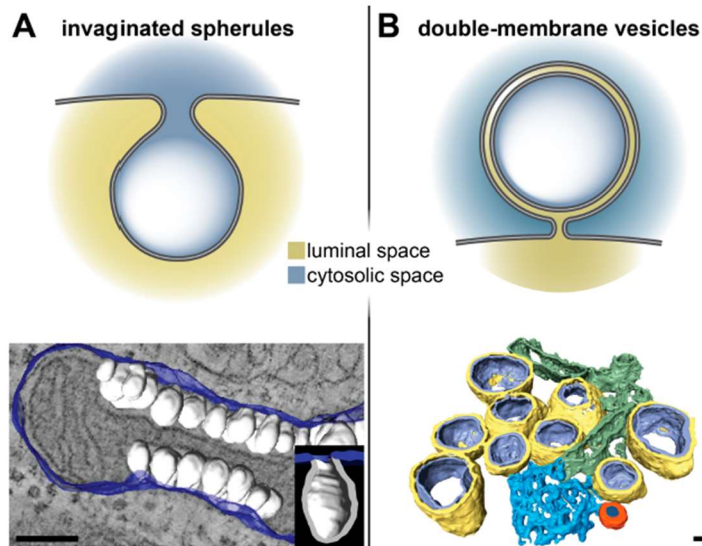


Figure 11. Invaginated spherules and double-membrane vesicles (DMVs) by electron tomography. Reprinted from “Multiscale Electron Microscopy for the Study of Viral Replication Organelles”, by Wolff et al., 2021, *Viruses*.

1.4.2 SARS-CoV-2 RO ultrastructure

Coronaviruses induce an elaborate vesicle-tubule network as ROs by exploiting the membranes of the secretory pathway. These structures appear as vesicles with a diameter between 200 and 400 nm and consist of an inner space surrounded by a double membrane, that is in connection with the ER (Figure 11-B)⁶⁵.

Recently, the work of Cortese et al. (2020) reported precise information on the structure of the RO of SARS-CoV-2 in infected Calu-3 cells by high-resolution electron tomography analysis.

In particular, the 3D architecture of the RO was determined. 24 hours after infection, DMVs with a diameter of 291 ± 48 nm is the dominant feature. Rarely these structures show an opening connecting the vesicle interior to the cytosol. The vesicles are formed by rough ER covered by ribosomes and are often interconnected or bound by ER membranes. Association with the ER occurs through smooth ER connectors with a narrow luminal space that connect DMVs to the rough ER. DMVs accumulate in the perinuclear region together with the fragmented and stacked membranes of the Golgi apparatus and peroxisomes⁶⁶.

Regarding the connectors of SARS-CoV-2, they appear to be structurally similar to the zippered ER structures reported for avian infectious bronchitis virus (IBV) gamma-CoV and, recently, for porcine delta coronavirus. It has been hypothesized that during infection, the lumen of the connector may collapse as a result of its elongation and form DMVs or that DMVs may form at one end first and thereafter there is a collapse of the connector lumen. The biogenesis of DMVs and connectors and how these may coexist has not yet been established, particularly whether these connectors can be a functional element in the formation of DMVs. RNA replication, as seen for MERS-CoV and SARS-CoV, occurs within DMVs. Electron microscopy experiments have revealed dsRNA

and de novo synthesized RNA labeled with [3H]uridine, and recently, cryo-electron microscopy experiments have confirmed this finding^{65,67,68}

1.4.2.1 DMV biogenesis

The biogenesis of DMVs remains a process that is still poorly understood. It is very difficult to discriminate which intermediates form the entire compartment since they are very rapid events difficult to capture by EM. In this regard, by observing the structures formed during the early times of infection, the different intermediates that would lead to the formation of ROs in Picornaviruses infections were hypothesized in the work of Melia et al. (2019) (Figure 12, Path 1). Specifically, intermediates involve the formation of a budded vesicle that, by membrane pairing, leads to the formation of a cisternae and then, due to the positive and negative curvature of the outer and inner membranes, leads to the formation of a closed DMV⁶⁹. Similarly, in the work of Snijder et al. (2020) a model of RO biogenesis is hypothesized for coronaviruses by observing the different structural intermediates that emerge during different time points of MERS-CoV infection, through EM experiments. In this case, DMVs arise from a tubular cisterna which curves to form an open DMV. Subsequently, this undergoes fission to give rise to DMVs connected to the organelle of origin. In addition, during infection, a small portion of DMVs may be observed floating, with no connection to the ER⁷⁰ (Figure 12, Path 2).

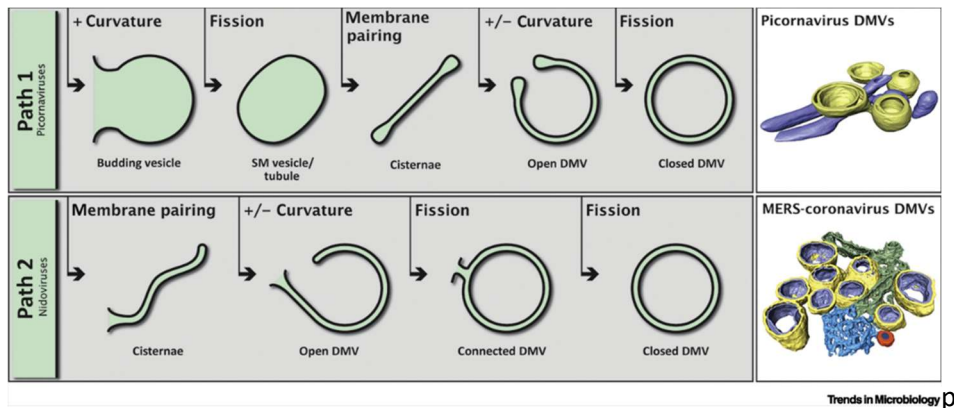


Figure 12. Pathways hypothesized for the formation of Double-Membrane Vesicle (DMV) and Representative 3D Models. Path1, possible intermediates observed during Picornavirus infection. Path2, hypothetical intermediates observed during Nidovirus infection. Reprinted from "Double-Membrane Vesicles as Platforms for Viral Replication," by Wolff et al., 2020, Trends in Microbiology.

The internal space of the DMVs represents an isolated environment for viral replication. Although many viruses have openings connecting the internal lumen to the external environment to exchange viral material with the cytosol, the DMVs induced by Coronaviruses have always been characterized as closed compartments. Only recently, in SARS-CoV-2 infected cells, pores on DMVs have been observed.^{71,72}

Of the nonstructural proteins, it has been reported that RO biogenesis is due to the role of some transmembrane nonstructural proteins, NSP3, NSP4 and NSP6, in SARS-CoV, MERS-CoV and SARS-CoV-2.^{73–77}

Expression of nonstructural proteins alone can induce DMV formation. In particular, the nonstructural proteins NSP3 and NSP4, which contain predicted transmembrane domains, have been identified as critical for the biogenesis of coronavirus DMVs. The interaction between the luminal loops of NSP3 and NSP4 would trigger this rearrangement of the host cell membrane⁷⁸.

Despite the knowledge accumulated in recent years, not only the biogenesis but also the lipid and protein composition of this compartment is unknown. Also, the roles of individual nonstructural proteins are still far from being determined. Future studies will need to unravel all features of the RO in order to use it as an antiviral target.

1.4.2.2 The Role of non-structural proteins in DMV biogenesis

1.4.2.2.1 NSP3

Nonstructural protein 3 (NSP3) is one of the largest proteins encoded by the SARS-CoV-2 genome, with a molecular mass of about 200 kDa.

NSP3 consists of different domains: ubiquitin-like domain 1 (Ubl1); the Glu-rich acidic domain (also called the "hypervariable region" HVR); macrodomain I (Mac1 or X); and the "Sars-unique domain" (SUD; composed of macrodomain II-Mac2 and macrodomain III-Mac3) preceding Ubl2 and PL2pro (DPUP); ubiquitin-like domain 2 (Ubl2); papain-like protease (PLpro); nucleic acid-binding domain (NBD); marker domain (MD); transmembrane regions (TM); the Y domain of unknown functions and two transmembrane regions, TM1 and TM2. NSP3 plays many roles in the viral life cycle; it is essential for forming RTCs and double-membrane vesicles (DMVs). The ubiquitin-like domain 1 (Ubl1) and the Glu-rich acidic region are located at the N-terminus of NSP3. The interaction with nucleocapsid (N) protein are mediated by Ubl1 domain⁷⁹⁻⁸¹.

In particular, the X domain (Mac1) is dispensable for RNA replication. Still, it plays a role in mediating the host's innate immune response in antiviral adenosine diphosphate-ribosylation signaling. It binds and removes ADP-ribose adducts from proteins in a posttranslational process. Mac2/3 domains are linked to RNA binding and preferentially bind oligo(G), which can form G-quadruplex⁸².

1.4.2.2.2 NSP4

SARS-CoV-2 NSP4 is a transmembrane protein of 44 kDa, with four transmembrane helices (TMD1-4), a large luminal domain (about 250 amino acids) between TMD1 and TMD2, a smaller luminal domain (approximately 30 amino acids) in the ER lumen between TMD3 and TMD4, and a C-terminal domain⁸³. The N- and the C-terminus reside in the cytosolic side of the ER membrane. Only the crystal structure of the C-terminal domain of NSP4 is known. All CoV NSP4 proteins have at least one predicted glycosylation site (N131). Interestingly, morphologically aberrant DMVs were observed in MHV-infected cells with a mutant form of NSP4 at the glycosylation site, where replication was impaired⁸⁴⁻⁸⁶. Furthermore, to promote proper membrane rearrangement, interaction with the terminal part of NSP3 (NSP3C) is required. In particular, in SARS-CoV, two amino acid residues, H120 and F121, play an essential role in binding NSP3 and promoting replication, whose site mutations cause complete rearrangement and membrane loss⁸⁷. NSP4 expression alone promotes the formation of paired membranes. These can be large areas of extensive accumulations or small regions of paired membranes, often ER-bound, devoid of ribosomes, and without spherules or DMVs. Probably, NSP4 is essential to induce a robust local bending of the ER membrane where, using NSP3, the viral pore is assembled.

1.4.2.2.3 NSP6

SARS-CoV-2 NSP6 is a 290 amino acid, 34 kDa membrane protein having 98.3 percent sequence similarity with that of SARS-CoV.

Angelini et al (2013) reported that SARS-CoV NSP6 induced the formation of small spherical single membrane vesicles, clustered around the microtubule organizing center. NSP3-4 alone produced convoluted maze-like bodies interspersed with double-membrane walled circular structures that were interpreted as closely packed double-membrane walled tubules, and that co-

expressing NSP6 appeared to partially resolve these tubules to produce DMVs⁷⁶. On the other hand, Oudshoorn, et al. (2017) found that NSP3-4 of MERS coronavirus efficiently produced DMVs, but co-expressing NSP6 had no effect⁷⁵. In general, it is assumed that NSP3-NSP4 promote and are necessary for the formation of DMVs, but the role of NSP6 is practically unknown, while SARS-CoV-2 NSP6 has not been studied at all. Adding to the problem, NSP6 has been reported as having several different topologies, predicted from bioinformatics studies, while the crystal structure of NSP6 has not been resolved.

In addition, NSP6, in several coronavirus species, has been reported to play a role in autophagy. However, despite multiple reports about an alteration in autophagic processes after infection, the specific involvement of (canonical) autophagy in DMV formation remains unclear. For example, Cottam et al., 2011, reported that NSP6 of MHV and IBV promote autophagosome formation, but these were smaller than the usual ones induced by starvation, and that NSP6 can limit autophagosome diameter. NSP6 in SARS has also been shown to induce Atg5- and LC3II-positive vesicle formation, in a starvation-independent manner, and, unlike what has been seen for the other coronaviruses, it shows discrete colocalization with LC3 puncta^{88,89}.

As for NSP6 of SARS-CoV-2, there are differing opinions on the autophagic aspect. Recently, in the work of Zhang et al., 2022, most of the viral proteins of SARS-CoV-2 were expressed in HEK293T cells to determine their effect on autophagy by detecting the protein levels of SQSTM1/p62 and LC3-II. In this case, NSP6 appears to induce no increase in LC3-II spots, suggesting no role in autophagy, unlike that shown for all other coronaviruses⁹⁰. Recently, Sun et al., 2022, reported the levels of endogenous and exogenous LC3 in Calu-3, A549, BEAS2B and 16HBE transfected with NSP1, NSP2 or NSP6 of SARS-CoV2 for 24h. LC3 levels were found to be increased in cells transfected with NSP6. Since, impairment of autophagic flux is observed only after 24h of transfection,

the authors of the paper suggest that NSP6 might impair autophagic flux at the late stage⁹¹.

In summary, if and how NSP6 contributes to and regulates autophagic flux remains controversial, and it remains to be determined whether there is its direct involvement in this biological process and whether this might be a pathway used to support RO formation.

2. Aims

Despite the RO being fundamental for SARS-CoV-2 replication and propagation, there was a relative dearth of knowledge regarding the viral proteins that were described as fundamental for their formation (NSP3 and NSP4), while the NSP6 protein had remained almost completely ignored. The first aim of my thesis was to elucidate the role of individual non-structural proteins NSP3, NSP4, and NSP6 in RO biogenesis, in particular the role and function of NSP6. Studying the cellular effects of a viral infection are multiple

and complex, in addition to requiring BSL-3 laboratory conditions, so initiating with a reductionist approach could help to control processes that are difficult to identify in a more complex system. A second aim was to use the knowledge gained to look for host factors that interact with or affect the processes mediated by the viral proteins. Building up a more integrated knowledge base would provide hypotheses to be validated in more relevant system such as SARS-CoV-2-infected cells. The long-term aim would be to find either viral or host targets for anti-viral therapy.

3. Methods and statistics

3.1 Reagents and antibodies

The following antibodies were used: mouse monoclonal anti-HA (BioLegend, 901503, dilution 1:600 for immunofluorescence (IF) and 1:1,500 for western blot (WB)), rabbit polyclonal anti-HA (Sigma-Aldrich, H6908, dilution 1:200 for IF), goat polyclonal anti-HA (Bethyl, A190-138A, dilution 1:600 for IF), rabbit polyclonal anti-actin (Sigma-Aldrich, A2066, dilution 1:10,000 for WB), rabbit polyclonal anti-NSP6 (ProSci, 9177, dilution 1:200 for IF and 1:1,000 for WB), sheep anti-NSP3 (The University of Dundee, DA126, dilution 1:100 for

IF and 1:1,000 for WB), rabbit polyclonal ADRP/Perilipin 2 (Proteintech, 15294-1-AP, dilution 1:200), rabbit monoclonal anti-DFCP1 (Cell Signaling, 38419, dilution 1:1,000 for WB), mouse monoclonal anti-Flag (Sigma-Aldrich, F1804, dilution 1:400 for IF and 1:1,500 for WB), goat polyclonal anti-Flag (Bethyl, A190-101A, dilution 1:200 for IF), mouse monoclonal anti-c-Myc (Santa Cruz, sc-40, dilution 1:200 for IF), mouse monoclonal anti-GAPDH (Santa Cruz, sc-32233, dilution 1:1,000 for WB), mouse monoclonal anti-LAMP1 (Hybridoma Bank, H4A3, dilution 1:200 for IF), rabbit monoclonal anti-EEA1 (BD Biosciences, 610456, dilution 1:1,000 for IF), sheep anti-human anti-TGN46 (BioRad, AHP500GT, dilution 1:750 for IF), rabbit polyclonal anti-GFP (Abcam, ab6556, dilution 1:250 for IF), mouse monoclonal anti-GFP (Santa Cruz, sc-9996, dilution 1:2,000 for WB), mouse monoclonal anti-mCherry (Abcam, ab125096, dilution 1:2,000 for WB), mouse monoclonal anti-V5 (Thermo Fisher Scientific, R960-25, dilution 1:200 for IF and 1:1,000 for WB), rabbit polyclonal anti-LC3 (Novus Biologicals, NB100-2220, dilution 1:200 for IF), mouse monoclonal anti-dsRNA (Scicons, 10010500, dilution 1:10 for IF), DAPI (Sigma-Aldrich, D9542, dilution 1:10,000 for IF), rabbit 1.4-nm gold-conjugated Fab' fragment (Nanoprobes, 2004, dilution 1:50), mouse 1.4-nm gold-conjugated Fab' fragment (Nanoprobes, 2002, dilution 1:50), Alexa Fluor-546 FluoroNanogold anti-mouse Fab' (7402, dilution 1:50) and Alexa Fluor-488-568-647 (Invitrogen, diluted 1:400), horseradish peroxidase (HRP)-conjugated goat anti-mouse or anti-rabbit IgG antibody (1:8,000, Merck Millipore, 401215 or 401315, respectively). Anti-GM130 (1:1,000 for IF) and anti-VAP-A (1:300 for IF) were produced in our laboratory as previously described⁹².

BODIPY 493/503 (4,4-difluoro-1,3,5,7,8-pentamethyl-4-bora-3a,4a-diaza-*s*-indacene), β -BODIPY FL C₁₂-HPC (2-(4,4-difluoro-5,7-dimethyl-4-bora-3a,4a-diaza-*s*-indacene-3-dodecanoyl)-1-hexadecanoyl-*sn*-glycerol-3 phosphocholine) and BODIPY 558/568-DA-C₁₂ (4,4-difluoro-5-(2-thienyl)-4-bora-3a,4a-diaza-*s*-indacene-3-dodecanoic acid) were purchased from Thermo Fisher Scientific (D3922, D3792 and D3835, respectively). Oil Red O solution was purchased from Merck (102419). K22 (N-[(1Z)-1-[[4-(4-bromophenyl)-4-hydroxy-1-piperidinyl]carbonyl]-2-phenylethenyl]-benzamide) was purchased from Cayman Chemical, the DGAT-1 inhibitor A922500 (A1737), wortmannin (3144), delipidated serum (S5394) and doxycycline hydrochloride (8D3447) from Sigma-Aldrich and the VPS34 specific inhibitor SAR405 from MedChemExpress (HY-12481). Puromycin dihydrochloride was purchased from Calbiochem (540411).

3.2 Plasmid constructs

All NSP constructs were made with the Gateway system (Thermo Fisher Scientific) using a modified pCDNA3.1 vector (containing a HA, Flag, Myc, GFP, or mCherry tag) for amino-terminal tagging, a modified pCDNA5/FRT/TO vector (containing 3×Flag) for carboxy-terminal tagging, unmodified pCDNA5/FRT/TO to clone untagged NSP6, and pLTD-Flag or pLTD-HA for stable doxycycline-inducible NSP6-expressing cell lines. P. Grumati provided all Gateway vectors. The donor plasmids were pDONR207 SARS-CoV-2 NSP3, pDONR223 SARS-CoV-2 NSP4, and pDONR223 SARS-CoV-2 NSP6 from Wuhan-Hu-1 SARS-CoV-2 (gifts from F. Roth, Addgene plasmids 141257, 141258 and 141260, respectively⁹³). For carboxy-terminal tagging of NSP6, the stop codon was removed using the oligo pairs NSP6 ns(+)/NSP6 ns(-) with the Agilent QuikChange kit. The Agilent QuikChange kit was used to make the following NSP6 N-terminally tagged mutant constructs: NSP6(1–157) (amino acids 1–157); NSP6-C80 (amino acids 211–290); the mutants in the amphiphilic alpha helix NSP6(F220Q/T222W) and NSP6-C80(F220Q/T222W); and the VOC mutant constructs NSP6(Δ SGF) and NSP6(Δ SGF)–NSP7.

The NSP6–NSP7 sequence was synthesized with flanking attB sequences by Thermo Fisher Scientific, a V5 tag was added to NSP7 by PCR, and the amplicon was cloned into the Gateway vector pDONR223 and recombined with destination vector pCDNA3.1 containing HA to produce pHA-NSP6-NSP7-V5. The IBV (avian infectious bronchitis virus, strain M41) NSP6 sequence (corresponding to Uniprot P0C6Y3 from position 3089 to 3381), optimized for human expression and synthesized with flanking attB sequences by Thermo Fisher Scientific, was cloned into the Gateway vector pDONR223 and recombined in Flag-containing Gateway destination vectors at the amino or carboxy terminus. Oligos NSP6-IBV ns(+)/NSP6-IBV ns(-) were used to remove the stop codon for the carboxy terminal-tagged construct.

mCherry-DFCP1 was a gift from D.-H. Kim (Addgene plasmid 86746). pEGFP-ATF6 was a gift from R. Prywes (Addgene plasmid 32955). mCherry-Calreticulin-N-16 (M. Davidson, Addgene plasmid 55006), pLenti-X1-Neo-GFP-ATL2 (J. Corn, Addgene plasmid 109020), pEGFPC-DFCP1 and pRUBY-N1-KDEL were provided by P. Grumati.

The Agilent QuikChange kit was used to make the following mCherry–DFCP1 mutant constructs: DFCP1(Δ 1–416) (lacking the amino terminus); DFCP1(W543A) (point mutation in the ER domain) and DFCP1(C654S/C770S) (mutations in the double FYVE domain; unable to bind PtdIns3P).

GST-tagged DFCP1 was constructed by amplifying the coding sequence from mCherry–DFCP1 with oligos DFCP1-p223(+)/DFCP1-p223(-) and cloning into the Gateway vector pDONR223 and subsequently into the Gateway vector pET60.

pEYFPC3-Cb5, constructed using YFP instead of mCherry, and pEGFP-VAP-A were made in our laboratory⁹⁴. pEGFP-ERGIC53 and p-KDEL-EGFP were gifts from A. Luini.

BP clonase and LR clonase for Gateway cloning were purchased from Thermo Fisher Scientific. All other reagents for molecular biology were purchased from New England Biolabs.

3.2 Cell culture, transfection, and RNA interference

HeLa cells were obtained from ATCC. Calu-3 cells (human lung adenocarcinoma), a gift from L. J. Galletta, were cultured in DMEM F-12 (Gibco), supplemented with 10% fetal bovine serum (Euroclone) 100 IU ml⁻¹ penicillin and 100 µg ml⁻¹ streptomycin (Thermo Fisher Scientific) and 2 mM L-glutamine (Thermo Fisher Scientific) in a humidified incubator at 37 °C and 5% CO₂. Cell lines were routinely tested for mycoplasma (Biological Industries). Cells were transfected with plasmids using either TransIT-LT1 (Mirus Bio) for HeLa cells or Lipofectamine LTX and PLUS Reagent (Thermo Fisher Scientific) for Calu-3 according to the manufacturer's instructions. Expression was maintained for 16–24 h before processing unless otherwise stated. For RNA interference, HeLa and Calu-3 cells were mock-treated or treated with DFCP1 siRNA (50 nM) for 96 h using Lipofectamine RNAiMAX (Thermo Fisher Scientific) for direct transfection.

3.3 Generation of HeLa Flag-NSP6 and HA-NSP6 doxycycline-inducible stable lines

To generate stably expressing clones, HeLa cells were transfected with the plasmids pLTD-Flag-NSP6, pLTD-Flag-NSP6(ΔSGF), pLTD-HA-NSP6 or pLTD-HA-NSP6(ΔSGF) and selected with complete medium containing 3 µg ml⁻¹ puromycin (Calbiochem). Single-cell cultures were isolated from the mixed populations, and protein expression was probed and induced with 1 µg ml⁻¹ doxycycline (Sigma-Aldrich) at different time points, as indicated. Samples were then processed by immunofluorescence analysis. All the cell lines generated in this study were authenticated through western blot and immunofluorescence.

3.4 SARS-CoV-2 infection and assays

SARS-CoV-2 infection, virus titration, and cell death assay through the activity of lactate dehydrogenase (LDH) were performed as elsewhere described⁹⁵. For

immunofluorescence experiments, Calu-3 cells were seeded on coverslips, left untreated or pre-treated for 2 h with K22 or with the DGAT-1 inhibitor A922500 at different concentrations, as indicated in the figures. Cell number and cell viability after treatment with either K22 or A922500 were assessed by crystal violet staining, cell morphology analysis, or LDH assay. No cytostatic or cytotoxic effect of the drugs was observed at the concentrations used. For immunofluorescence experiments and drug treatments, Calu-3 cells were seeded on coverslips and infected with SARS-CoV-2 early lineage (SARS-CoV-2/human/BRA/RJ01/2020, GenBank accession no. MT710714) at a multiplicity of infection (MOI) of 0.01 for 48 h. Infected cells were fixed with 3.7% formaldehyde and processed for immunofluorescence as described⁹⁵. For comparative analyses of NSP3–NSP6 proximity, cells were similarly infected with early lineage and Gamma variant (hCoV-19/Brazil/AM-L70-71-CD1739/2020, GISAID ID: EPI_ISL_1060902) SARS-CoV-2 at an MOI of 0.01 for 48 h.

For EM experiments, Calu-3 cells were infected with early lineage B.1 (hCoV-19/Italy/CAM-INMI-32803-66/2020, GISAID ID: EPI_ISL_493333) or Gamma variant (hCoV-19/Italy/CAM-IZSM-RD020483D54/2021, GISAID ID: EPI_ISL_2933105) SARS-CoV-2 strains at an MOI of 10 for 24 h. SARS-CoV-2-infected Calu-3 cells were processed for EM as described below. All procedures related to virus culture were handled at a biosafety level 3 (BSL3) multi-user facility, according to World Health Organization (WHO) guidelines.

3.5 Drug treatments

Flag–NSP6- and mCherry–DFCP1-transfected cells were treated with either 100 nM wortmannin or 1 μ M VPS34 inhibitor SAR405 for 3 h, then processed for immunofluorescence. For K22 treatment, cells were transfected, and after 30 min, dimethyl sulfoxide (DMSO) or 40 μ M K22 was added.

For co-immunoprecipitation experiments, 1.7 mg of cellular lysate from cells mock-transfected or co-transfected with HA–NSP6 together with GFP–NSP6, Flag–NSP6, GFP–ERGIC53, GFP–atlastin-2 or GFP–NSP6(1–157), or co-transfected with HA–NSP6(Δ SGF) and GFP–NSP6(Δ SGF), were incubated with appropriate antibody-conjugated beads (HA, Flag and GFP). After overnight incubation at 4 °C in 750 μ l binding buffer, samples were washed five times with binding buffer and once with a similar buffer without detergents, eluted, and analyzed by SDS–PAGE. To evaluate co-immunoprecipitation efficiency, a total of three independent experiments were analyzed. The co-immunoprecipitated GFP–NSP6 signal was divided by the GFP–NSP6 signal in the input and normalized by the immunoprecipitated primary antigen (HA) signal. Co-immunoprecipitation efficiency was reported as mean \pm s.e.m. of co-immunoprecipitated GFP–NSP6(Δ SGF) compared to GFP–NSP6.

3.6 Western blot analysis

Western blot analysis and densitometry were performed as previously described⁹⁶. Samples containing NSP6 were mixed with sample buffer (100 mM Tris pH 6.8, 25% glycerol, 2% SDS, 0.01% bromophenol blue, and 10% 2-mercaptoethanol) but were not boiled before loading.

3.7 Immunofluorescence analysis

Immunofluorescence analysis was performed as previously described⁹⁴.

Digitonin and Triton-X-100 permeabilization

HeLa cells transfected with Flag–NSP6 or NSP6–Flag were grown on coverslips and fixed with 4% PFA for 10 min, washed three times with buffer A (20 mM PIPES pH 6.8, 137 mM NaCl and 2.7 mM KCl) and permeabilized with 20 μ M digitonin (Calbiochem) diluted in buffer A for 5 min. Coverslips were blocked for 30 min with blocking solution (5% FBS (v/v) and 50 mM NH₄Cl in buffer A) without any additional permeabilizing agent and incubated with primary anti-Flag and anti-TGN46 antibodies diluted in blocking solution. The TGN46 antibody was raised against a luminal portion of the protein that is thus not accessible after digitonin permeabilization. This represents a control in that only the plasma membrane has been permeabilized. Coverslips were washed with buffer A and incubated with fluorochrome-conjugated secondary antibodies (Alexa Fluor-488 for Flag and Alexa Fluor 568 for TGN46 in buffer A) for 1 h at room temperature. After incubation, cells were fixed with 2% PFA for 5 min and washed once with 50 mM NH₄Cl in PBS. Coverslips were subsequently permeabilized with 0.1% Triton-X-100 in PBS for 5 min. Cells were then blocked with a blocking solution (0.05% saponin, 0.5% BSA, and 50 mM NH₄Cl in PBS) and incubated with the same primary antibodies used in the first step. Coverslips were then washed with PBS and incubated with fluorochrome-conjugated secondary antibodies (Alexa Fluor 405 for Flag and Alexa Fluor 633 for TGN46 in PBS) for 1 h at room temperature. The TGN46 epitope becomes accessible to the primary antibody under these conditions, confirming selective permeability and identifying luminal epitopes.

LD staining and assays

LDs were stained by adding 0.5 μ M BODIPY 493/503 (Thermo Fisher Scientific) to the fluorochrome-conjugated secondary antibody mix for 30 min after fixation and processed for immunofluorescence analysis.

To monitor lipid transfer from LDs to DMVs, we followed the protocol described previously⁹⁷. In brief, BODIPY 558/568-DA-C₁₂ at a final concentration of 1 μ M was added for 16 h to the culture medium of HeLa cells transfected with GFP-NSP4/HA-NSP3 or GFP-NSP4/HA-NSP3/Flag-NSP6. Cells were then washed and incubated with DMEM supplemented with delipidated serum (1%) for an additional 6 h. Coverslips were fixed and processed as described above. NSP4 puncta were identified using the 'Analyze particles' tool of Fiji (ImageJ) software, and the fluorescence mean intensity of Bodipy-DA-C₁₂ for each particle was determined. Particles with values equal to or higher than a similar ER area were defined as 'positive' particles. The percentage of NSP4 Bodipy-DA-C₁₂-positive particles was calculated for each cell.

3.8 Confocal microscopy and image analyses

Cells were imaged using a Plan-Apochromat 100 \times /1.4 oil objective on a Zeiss LSM800 or LSM880 confocal system equipped with an AiryScan module and controlled by the Zen blue software. Fluorescence images presented are representative of images collected from at least three independent experiments, unless otherwise stated (see 'Statistics and Reproducibility' for further details). The images used for phenotype quantification were acquired with the same parameters (that is, digital gain, laser power, and magnification) and processed with Fiji (ImageJ; National Institute of Health (NIH)) software. Brightness and contrast were adjusted with Adobe Photoshop, and figure panels were assembled with Adobe Illustrator.

3.9 Quantification of the number and area of structures

NSP6, NSP4, LC3, and LD structures were analyzed using the 'Analyze particle' function to determine their number per cell. For each experiment, images were acquired below the saturation limit, and the same threshold was chosen and applied to all of them. For the calculation of the size of the structures the 'Analyze particle' function was used, setting 'Area' as the measurement.

3.10 Distribution of NSP4 puncta

The 'Analyze particle' function was used to calculate the distribution of NSP4 puncta in each cell, considering a particle size between 0.1 and infinity and choosing the centre of mass as a reference for measurement. *X* and *Y* coordinates for each NSP4 puncta were obtained and plotted. A four-quadrant subdivision

was applied to the images using the *XY* coordinates of the centre of mass as the axis origin. The relative abundance of the NSP4 puncta for each quadrant is expressed as a percentage of the total identified structures for each cell.

3.11 Relative distribution of the NSP6 protein

To measure the cellular distribution of NSP6 fluorescence, the integrated density of NSP6 in NSP6 structures was calculated over the integrated density of total NSP6 in the whole cell.

Cells with comparable levels of total integrated fluorescence intensity were analyzed for each time point. Results were expressed as a percentage of the fluorescent NSP6 signal present in the NSP6 structures over the total fluorescence.

3.12 Recruitment to NSP6 structures

The fraction of VAP-A or NSP6(1–157) associated with NSP6-positive structures was measured as the ratio between the integrated density of each protein on the NSP6 structures and the integrated density in the whole cell.

3.13 Co-localization between NSP6 and DFCP1

Co-localization between NSP6 and wild-type or mutant DFCP1 was calculated using the JACoP plug-in⁹⁸.

3.14 Distance between particles

The relative distance between objects was determined with the DiAna plug-in⁹⁹. In brief, channels were thresholded and then segmented. For LD distance from NSP4 and NSP6 in transfected cells shown in Fig. 46, edge–edge distances between particles were measured in the whole cell. No values were excluded.

To calculate the distance between NSP3- and NSP6-positive structures in infected cells in Fig. 34, both centre–centre and edge–edge distances were measured.

3.15 Measurements of NSP6 fluorescence intensity

HeLa cells expressing Flag-tagged NSP6 were fixed and processed for immunofluorescence. Cells with similar expression were acquired using the same parameters and processed with the Fiji (ImageJ) software. The integrated density of each cell was measured.

Electron microscopy

For pre-embedding IEM, the cells were fixed, permeabilized and labeled as described previously¹⁰⁰. In brief, the cells were fixed with a mixture of 4% paraformaldehyde (PFA) and 0.05% glutaraldehyde prepared in 0.2 M HEPES buffer for 10 min (room temperature) and then with 4% PFA alone for 30 min (room temperature), followed by incubation with blocking/permeabilizing solution (0.5% bovine serum albumin (BSA), 0.1% saponin and 50 mM NH₄Cl in PBS) for 30 min.

Cells were incubated with a primary anti-HA monoclonal antibody (1:600, BioLegend) diluted in blocking/permeabilizing solution overnight, and then a secondary anti-mouse antibody (1.4-nm gold-conjugated Fab' fragment diluted 1:50, Nanoprobes) was added for 2 h. The GoldEnhance EM kit (from Nanoprobes) was used to enhance ultrasmall gold particles. For double labeling of cells expressing HA–NSP3, mCherry–NSP4, and GFP–NSP6, enhancement with the anti-HA antibody was performed for 3 min. Then a primary anti-GFP polyclonal rabbit antibody (1:250, Abcam) was added and processed as above using a secondary anti-rabbit antibody (1.4-nm gold-conjugated Fab' fragment diluted 1:50, Nanoprobes) for 2 h, followed by gold enhancement for an additional 3 min. The longer enhancement time for the anti-HA detection causes the formation of larger gold particles (clusters) with an irregular shape that distinguishes HA–NSP3 from the smaller GFP–NSP6 signals in doubly transfected cells.

For conventional EM, the cells were fixed with 1% GA prepared in 0.2 M HEPES buffer for 30 min (RT).

Cells prepared for IEM or conventional EM were scraped, pelleted, post-fixed in OsO₄ and uranyl acetate, dehydrated, embedded in Epon, and polymerized at 60 °C for 72 h. For each sample, thin sections were cut using a Leica EM UC7 ultramicrotome (Leica Microsystems). EM images were acquired from thin sections using a FEI Tecnai-12 electron microscope (FEI) equipped with a VELETTA CCD digital camera (Soft Imaging Systems). Morphometric analysis of the structures of interest was performed using iTEM software (Olympus).

3.16 CLEM

HeLa cells were transfected with HA–NSP6 or HA–NSP6(Δ SGF) or co-transfected with HA–NSP3/mCherry–NSP4/GFP–NSP6 or HA–NSP3/mCherry–NSP4/Myc–NSP6 where indicated. Transfected cells were treated or not with 40 μ M K22 30 min after transfection. After overnight expression, cells were fixed as for IEM and then labeled with an anti-HA antibody followed by detection with a secondary Alexa Fluor-546 FluoroNanogold anti-mouse Fab'. The structures of interest carrying different proteins were visualized using a Zeiss LSM800 station by confocal microscopy, and fluorescent images were recorded. Then the cells were post-fixed,

dehydrated, embedded in Epon, and polymerized as described above. Serial 60-nm sections were cut and analyzed using a FEI Tecnai-12 electron microscope. The same cell and structures of interest obtained by confocal microscopy were identified on EM images using Zen Connect software (Zeiss).

3.17 Electron tomography

Epon sections (250 nm thick) were collected on Formvar carbon-coated slot grids and analyzed using a Tecnai G2 Spirit BioTwin electron microscope (FEI) equipped with an automated tomography stage. The single tilt series of images were acquired in a range of -65° to $+65^{\circ}$ (at 1° interval) using Xplore 3D TEM Tomography software (FEI) at $40,000\times$ magnification unless otherwise stated. Tilt series were used with the open-source IMOD software to generate tomograms. At least 10 tomograms were analyzed per experimental condition. For 3D reconstruction, the surfaces of DMVs and surrounding ER membranes were rendered using the IMOD software.

3.18 EM quantification

The percentage of regular and zippered ER (or NE) surface was quantified in random thin sections from pellets of NSP6-transfected HeLa cells using morphometric grids with the iTEM software (Olympus SIS). Quantification of gold particles in thin sections from HeLa cells expressing HA-NSP6 or HA-NSP6(Δ SGF) and immuno-gold labeled for HA was performed with the touch count tool of the iTEM software. This quantification was further used to measure HA-NSP6 or HA-NSP6(Δ SGF) expression in each analyzed cell to normalize the surface area of zippered ER for the expression level of the corresponding HA-tagged NSP6 protein. To assess the effect of NSP6 or NSP6(Δ SGF) on the organization of DMVs, tomograms of DMV clusters were used to quantify the following parameters: DMV diameter, shape factor (ratio between long and short axes), density (number per DMV cluster area), length of ER-DMV connections, number of DMVs per connection and the overall number of ER-DMV connections per DMV cluster. A DMV cluster was defined as a group of DMVs whose distance from the nearest neighbor does not exceed two average DMV diameters. All measurements in tomograms were done with the 3D Manager plug-in of the open-source Fiji software. The same tools were used to quantify the length of zippered DMV connectors in tomograms from Calu-3 cells infected with the early lineage B.1 or Gamma variant of SARS-CoV-2.

3.19 NSP6 protein topology

NSP6 topology modeling was performed using the Constrained Consensus Topology prediction server (CCTOP, Institute of Enzymology). The amphipathic features of the α -helix were determined using HELIQUEST (<http://heliquest.ipmc.cnrs.fr>)¹⁰¹ and the mutations were introduced following the Genetic Algorithm-based module.

3.20 Phylogenetic analysis

The phylogenetic analysis of SARS-CoV-2 genomes deposited in the GISAID database (<https://www.gisaid.org/>) was performed on a set of 3,508 representative genomes sampled from December 2019 to July 2021, provided by Nextstrain¹⁰² (<https://nextstrain.org/ncov/global>). The percentages of genomes carrying the SGF deletion in the NSP6 protein were evaluated on samples deposited at GISAID up to 16 July 2021.

3.21 Statistics and reproducibility

Statistical analyses were performed using GraphPad Prism7 (GraphPad Software) or the R software environment for statistical computing (rstatix R package).

To test the normal distribution of the data and the homogeneity of variance across groups, the Shapiro–Wilk test, and Levene’s test were used on the ANOVA residuals. When measured variables were normally distributed, the statistical significance of the difference in measured variables between control and treated groups was determined by *t*-test or ANOVA followed by appropriate multiple comparisons post-hoc tests depending on the experiment. When the measured variables were not normally distributed, non-parametric Mann–Whitney or Kruskal–Wallis tests were performed followed by appropriate multiple comparison post-hoc tests depending on the experiment.

All the experiments for which statistics was derived were performed three times with similar results; *N* indicates the number of experiments and *n* the number of total measurements or observations. All of the replicates performed were biological and not technical. Detailed information for each experiment is provided below.

4. Results

4.1 NSP6 promotes the formation of roundish structures

NSP6 from other coronaviruses had previously demonstrated widespread distribution in the ER when it was C-terminally tagged^{76,88}. In this study, however, SARS-CoV-2 NSP6 was cloned with a C-terminal and N-terminal tag to understand the correct topology of the protein. In addition, an untagged version of SARS-CoV-2 NSP6 was cloned; an antibody against the viral protein NSP6 was used to analyze its localization.

Very interestingly, as shown in Fig.13, while the expression of the C-terminally tagged protein shows a diffuse ER localization, N-terminally tagged NSP6 and the untagged NSP6 protein both promote the formation of roundish structures.

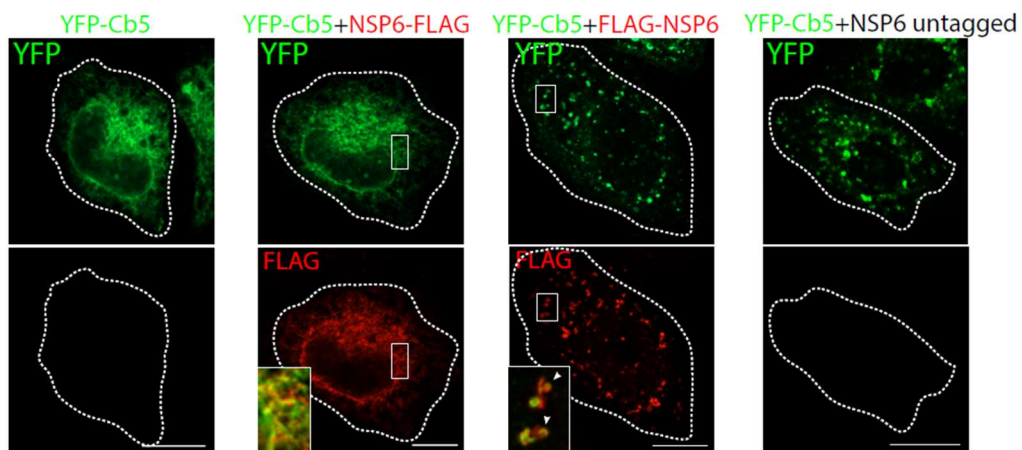


Figure 13. HeLa cells expressing YFP–Cb5 alone, co-expressing C- or N-terminally Flag-tagged NSP6, or co-expressing untagged NSP6. Insets, enlarged merged images of boxed areas; arrowheads, NSP6 compartments; dashed lines, cell boundaries. Scale bars, 10 μ m.

In particular, the NSP6-induced structures do not colocalize with endosomal, lysosomal, or autophagosomal structures. At the same time, they exhibit a preferential colocalization with the ER-reporter protein Cb5 (the C-terminal tail of cytochrome b5)¹⁰³ (Fig. 14).

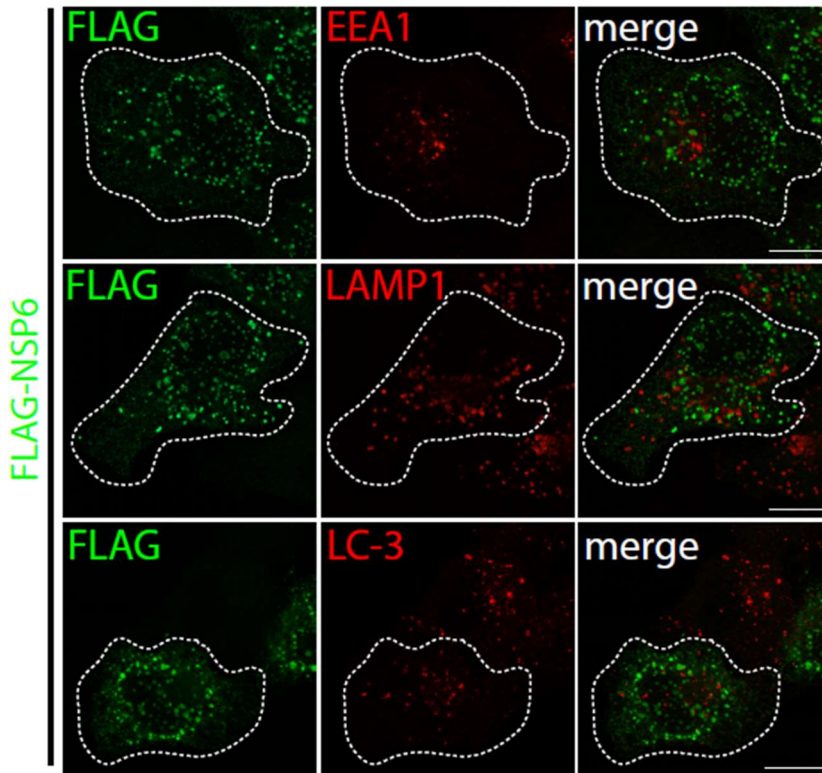


Figure 14. HeLa cells transfected with Flag-NSP6 immunostained with anti-Flag, lysosome marker (anti-LAMP1), endosome, and autophagosome marker (anti-EEA1 or anti-LC3). Scale bars, 10 μ m.

To investigate whether the formation of round structures of NSP6 was a general feature of NSP6 of coronaviruses, we examined the NSP6 protein of infectious bronchitis virus (IBV) by tagging it at the N- and C-terminus. From the results obtained, NSP6-IBV tagged at the N terminus also induces round structures that colocalize with Cb5 (Fig. 15).

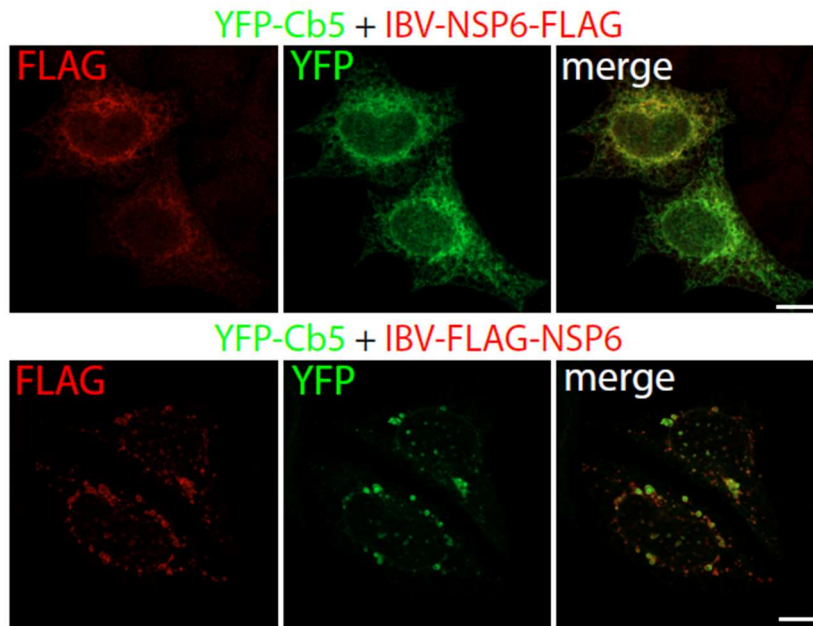


Figure 15. Fluoromicrographs of HeLa cells expressing YFP-Cb5 and either IBV NSP6-Flag (upper panels) or IBV-Flag-NSP6 (lower panels). Cells immunostained with anti-Flag antibody (red). Scale bars, 10 μ m.

4.2 NSP6 induces ER zippering

To identify the source membranes of NSP6 structures, we used immuno-electron microscopy (IEM) analysis. For this aim, HA-NSP6 overexpressing HeLa cells were fixed and immunogold labeled to reveal the HA signal. The NSP6 signal was highly enriched on ER cisternae. These roundish structures were formed by tightly juxtaposed boundary membranes, leaving a barely visible lumen (Fig. 16).

Interestingly, in NSP6-expressing cells, about 40% of the ER surface is zippered (Fig. 16). These zippered ER structures were linear or circular and capable of encapsulating the adjacent cytoplasm (Fig. 16).

Moreover, to establish if the zippered ER structures were connected to the regular ER, electron microscopy (EM) and electron tomography approaches were also used on HA-NSP6 overexpressing cells, where clear connections

between these zippered ER structures and regular ER could be observed (Fig. 16).

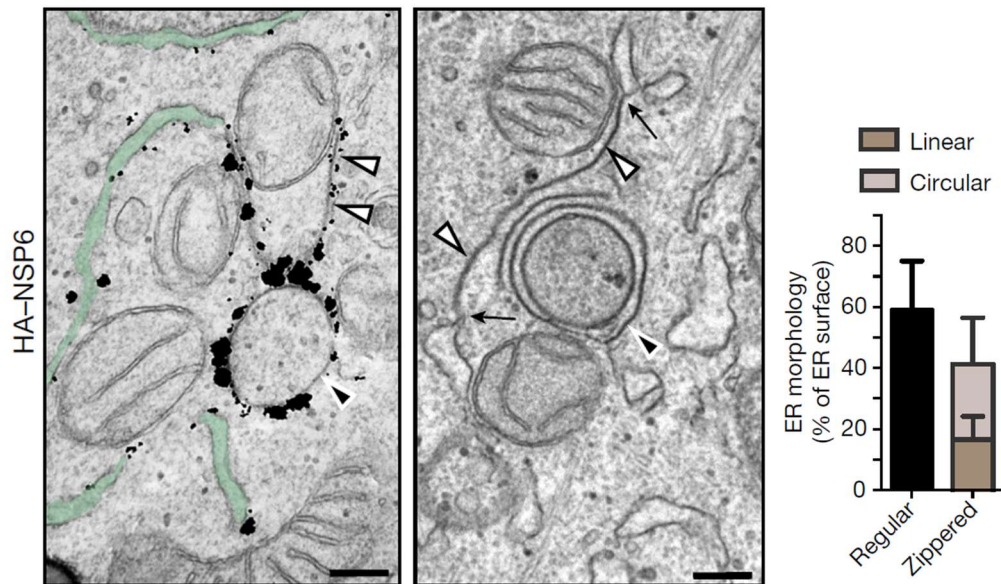


Figure 16. Left, IEM (anti-haemagglutinin (HA) immunolabelling) and EM of HeLa cells expressing HA-NSP6. White arrowheads, linear zippered ER membranes; black arrowheads, circular zippered ER membranes; black arrows, continuity between zippered and regular ER membranes. The regular ER is shown in green. The average size of circular NSP6-positive ER structures is 623 ± 231 nm. Right, Morphometric analysis of NSP6-expressing cells (percentage of the ER surface associated with regular cisternae or zippered domains). Mean \pm s.d. Scale bars, 120 nm. Experiments were performed by Roman and Lena Polishchuk.

Further, a correlative light and electron microscopy (CLEM) approach using HeLa cells expressing HA-NSP6 showed that the round or elongated structures of NSP6 visualized by immunofluorescence matched the circular or linear profiles observed by electron microscopy, including connections with the regular ER (Fig. 17).

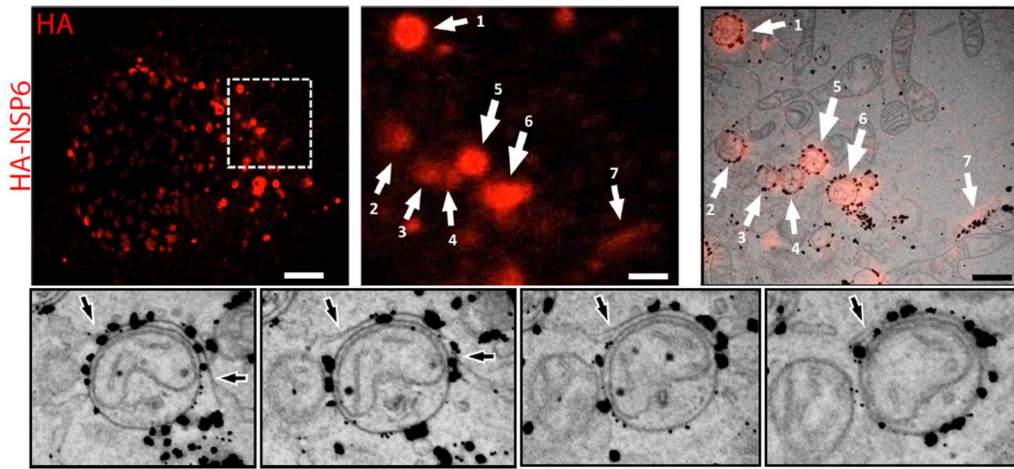


Figure 17. Upper, Immuno-CLEM analysis of the NSP6 compartments. Fluoromicrograph of HA-NSP6. With the enlargement of NSP6-labelled structures 1–7 that were identified on EM serial sections. Bottom, Serial sections of structure 6. Black arrows, NSP6-positive linear zippered membrane connections with ER cisternae. White arrows, NSP6-positive circular zippered structures. Scale bars, 4 μm (Upper, left); 1.1 μm (Upper, middle and right); 250 nm (Bottom). Experiments were performed by Lena Polishchuk.

4.3 NSP6 structures are selectively accessible to proteins and lipids

Since NSP6 can remodel ER membranes by promoting the formation of zippered, lumenless structures, we decided to better characterize the accessibility of this compartment to proteins and lipids by co-expressing GFP- or mCherry-NSP6 in HeLa cells with ER luminal proteins (such as mCherry-Calreticulin and the ER reporter GFP-KDEL) or with ER membrane proteins with bulky luminal domains (such as GFP-ERGIC53 and GFP-ATF6) (Fig. 18).

From live cell imaging experiments, no colocalization was observed; rather there was exclusion of proteins occupying a luminal fraction of the ER and NSP6 structures, suggesting “inaccessibility” of the zippered compartment.

Subsequently, we expressed mCherry-NSP6 with ER membrane proteins such as GFP-VAP-A, GFP-Atlastin-2, and GFP-KDEL receptor, which lack or possess small luminal tracts. Interestingly, complete localization of these

transmembrane proteins to the NSP6 compartment was observed, suggesting that these proteins can access zippered structures.

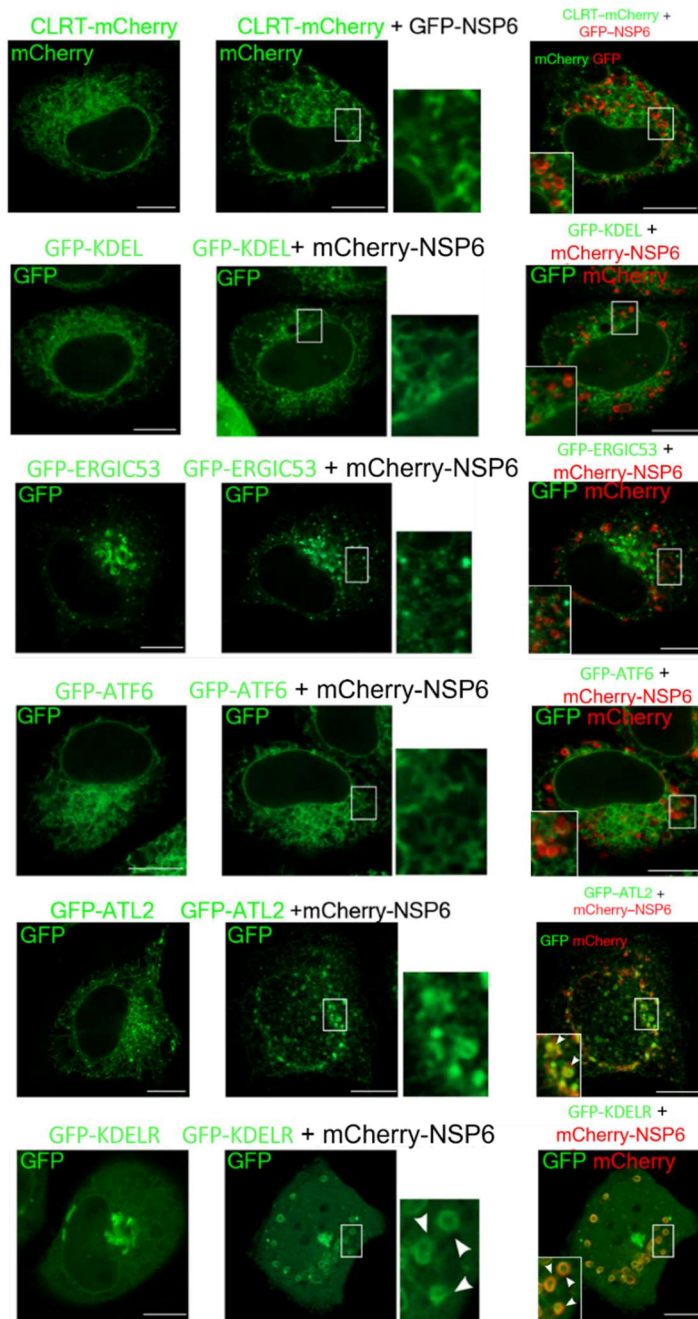


Figure 18. Fluoromicrographs of HeLa cells expressing CLRT-mCherry, GFP- KDEL, GFP-ERGIC53, GFP-ATF6, GFP-ATL2, GFP-KDELR alone (left panel) or with GFP-NSP6 and mCherry-NSP6 (middle and right panel). Small panels, enlargements of boxed areas, and arrowheads indicate co-localization. Scale bars, 10 μ m.

To validate the continuity between the NSP6 compartment and the ER, we decided to use the fluorescent recovery after bleaching (FRAP) technique. In particular, the choice of FRAP allowed us to monitor the recovery of fluorescence after bleaching performed in a region of interest. The diffusion movement of surrounding intact probes in the irreversibly bleached region is used to examine the kinetics of the protein of interest.

HeLa cells were co-transfected with mCherry-NSP6 and GFP-VAP-A or mCherry-NSP6 and YFP-Cb5. NSP6-induced structures were bleached to assess the fluorescence recovery of VAP-A or Cb5 within the compartment. Both VAP-A and Cb5 managed to re-enter the NSP6 compartment. However, the kinetics were slower than the recovery observed in the regular ER because the available luminal area is smaller in the zippered ER (data not shown).

Similarly, to understand whether zippered structures were accessible to phospholipids, HeLa cells transfected with mCherry-NSP6 and treated with a phosphatidylcholine fluorescent probe (BODIPY C12-HPC) were analyzed by FRAP. In this case, the fluorescence of BODIPY C12-HPC was recovered after bleaching, suggesting that the NSP6-zippered compartment is accessible to lipids. However, NSP6 showed limited FRAP, probably because it is engaged in stable protein complexes that result in its slow diffusion (data not shown).

4.4 NSP6 homodimers zipper ER membranes

As mentioned in the introduction, the structure of NSP6 has not been solved, and several topologies have been predicted. Both the N- and C-termini of NSP6 should face the cytosol since they must be accessible for processing by the cytosolic protease NSP5. To confirm this, HeLa cells were transfected with an NSP6 construct with the N- or C-terminus tagged with a FLAG epitope and then processed for immunofluorescence. The cells were treated with digitonin (without any additional permeabilizing agent) that permeabilizes only the plasma membrane. Then, the cells were probed with an anti-FLAG primary, so

if the portion of the protein is cytosolic and not luminal, it is accessible to the antibody. As shown in Fig. 20, both N- and C-terminally FLAG-tagged NSP6 are detectable, showing that they must be exposed to the cytosol. Controls included using an antibody against a luminal epitope of TGN46, which was not detected, and Triton-X-100 treatment, which allows access to luminal compartments (Fig. 19).

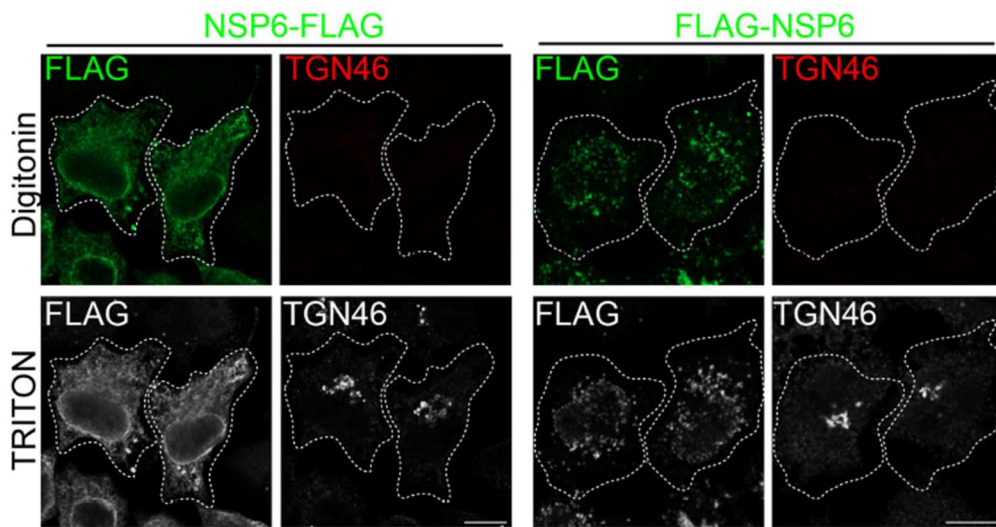


Figure 19. HeLa cells expressing C-terminal or N-terminal Flag-tagged NSP6 immunostained with anti-Flag antibody and an antibody against a luminal epitope of TGN46 after permeabilization with digitonin and subsequently with Triton-X-100. Scale bar, 10 μ m. Experiment performed by Andrea Maria Guarino.

Based on these data and biochemical analyses of other coronaviruses, we conducted topological predictions with the CCTOP13¹⁰⁴ server and assigned six transmembrane domains to NSP6 (Fig. 20). In addition, we hypothesized that the seventh predicted transmembrane domain, which is an amphipathic helix¹⁰¹, does not cross but remains associated with the membrane (Fig. 20).

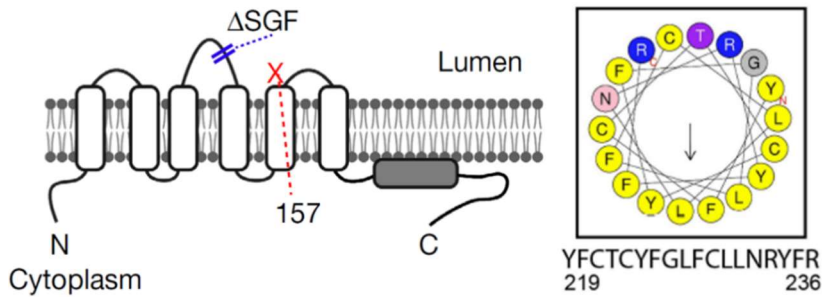


Figure 20. Left, Predicted secondary structure of NSP6. The Δ SGF deletion and truncation site (at residue 157) are indicated. Right, Model of the amphipathic helix of NSP6 according to HELIQUEST. Apolar residues are in yellow, and polar residues and glycine have been given different colors. The arrow indicates the hydrophobic moment ($\mu H = 0.409$). Numbers indicate the amino acid positions of the NSP6 protein.

As described above, the addition of a tag to the NSP6-C-terminus inhibits the induction of zippered structures and the bioinformatics analysis indicates that the C-terminal amphipathic tail associates with the membrane without crossing it. We therefore asked if the C-terminal portion was necessary for the proper localization of NSP6.

To test this, we cloned and expressed in HeLa cells either a NSP6 mutant (1-157) lacking the C-terminal part of NSP6, including the amphipathic helix, or a mutant in which two mutations were introduced into the C-terminal portion of NSP6, abrogating its amphiphilic properties (F220Q/T222W)¹⁰¹. Both mutants show widespread localization of NSP6 in the ER, suggesting that the amphipathic helix is required to induce ER remodeling (Fig. 21).

This suggests that, although necessary, the amphipathic helix is insufficient to promote the formation of NSP6 structures. To understand which other features of NSP6 are critical for generating the zippered compartment, we considered the EM data that showed the zippered structures as two membranes held together, almost completely excluding the lumen, and the low mobility of the NSP6 protein in the FRAP analysis, and hypothesized that NSP6 might be engaged in homodimeric binding which drives the formation of the zippered structures. To validate this hypothesis, co-immunoprecipitation experiments were performed using extracts from cells expressing HA-NSP6 co-expressed with GFP-NSP6 or FLAG-NSP6. The cell lysates (input) were immunoprecipitated (IP) with anti-HA, anti-Flag, or anti-GFP antibodies and probed by WB (Fig. 22), which showed that NSP6 can homodimerize.

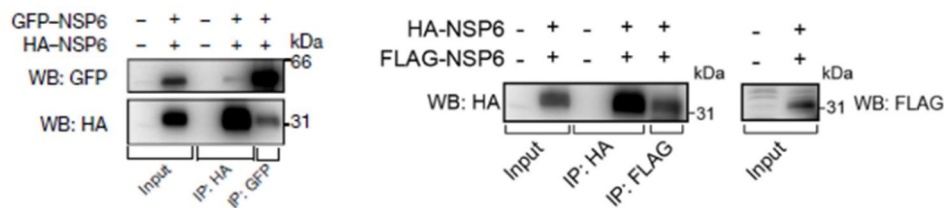


Figure 22. Left, Immunoprecipitation (IP) and western blot (WB) from GFP-NSP6 and HA-NSP6 co-expressing cells. Right, Cell lysates (input) and immunoprecipitates (IP, with anti-HA or anti-Flag antibodies) from HeLa cells, untransfected or expressing the indicated NSPs were analyzed by western blot with anti-HA, anti-Flag, or anti-GFP antibodies as appropriate. Images are representative of three independent experiments. Experiment performed by Giuseppe Di Tullio.

To corroborate the biochemistry data, we took advantage of a powerful tool to analyze the ability of NSP6 to interact with an additional NSP6 in vivo. Specifically, we used the Fluorescence resonance energy transfer (FRET) method, which is widely used and set up in Antonella De Matteis' laboratory, especially for studying ER-Golgi contact sites. This method analyzes the physical molecular distance from an excited molecular fluorophore (the donor) to another fluorophore (the acceptor) through a non-radiatively energy transfer. The FRET analysis was performed on HeLa cells expressing GFP-NSP6 and mCherry-NSP6 and confirmed the homodimerization of NSP6 (data not shown).

To understand whether dimerization involved amino acids 1-157 of the NSP6 protein, i.e. without the C-terminal part of the protein, NSP6(1-157) and full-length NSP6 were co-expressed in HeLa cells, and we found that the mutant protein is massively recruited and retained in the NSP6 compartment (Fig. 23). The interaction between NSP6(1-157) and NSP6 was also confirmed by FRET (data not shown) and co-immunoprecipitation experiments, indicating that the dimerization involves amino acids 1-157 of NSP6 (Fig. 24). Thus, it seems that both the C-terminal amphipathic helix and homodimerization of NSP6 (via amino acids 1-157) are necessary to generate the NSP6 compartment.

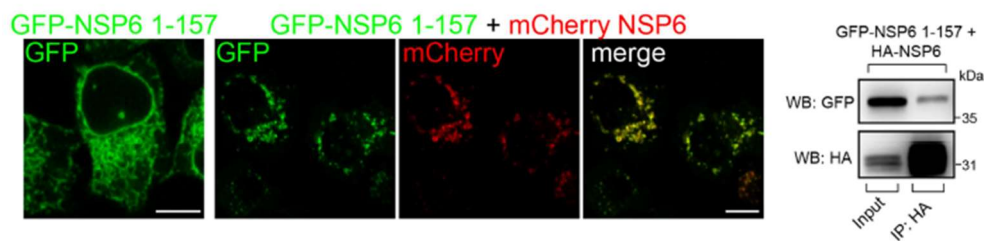


Figure 23. Left, Fluoromicrographs of HeLa cells expressing GFP-NSP6(1–157) alone or with mCherry-NSP6. Right, Cell lysates (input) and immunoprecipitates (IP, with anti-HA or anti-Flag antibodies) from HeLa cells, untransfected or expressing the indicated NSPs were analyzed by western blot with anti-HA, anti-Flag, or anti-GFP antibodies as appropriate Scale bar, 10 μ m. WB experiment was performed by Giuseppe Di Tullio.

4.5 K22 interferes with the zipping activity of NSP6

We searched the literature to see if there were any known compounds that were reported to target NSP6. A small molecule called K22 was described as interfering with the replication of several coronaviruses and it was hypothesized that NSP6 could have been the target, since K22-resistant human coronavirus strains such as coronavirus 229E (HCoV-229E) had mutations in NSP6¹⁰⁵.

To test K22 in our system to test whether it could also affect NSP6 of SARS-CoV-2. First, we used different concentrations of K22 in the NSP6-inducible cell

line and monitored its effects. Using a concentration of 40 μM , we observed a significant reduction in the number of regular NSP6 structures, as shown in (Fig. 24).

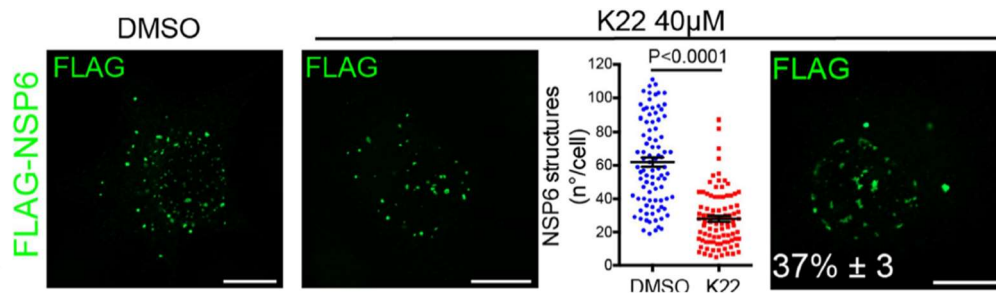


Figure 24. Stably transfected Flag-NSP6 clone induced with doxycycline and treated with DMSO or K22 for 24 h. K22 reduced the number of NSP6 structures and resulted in elongated structures in a percentage of the cells (right panel, number of cells exhibiting these structures. Mean \pm SD). Two-tailed unpaired t-test with Welch's correction. Scale bars, 10 μm . Experiment performed by Laura Giaquinto.

In addition, 37% of K22-treated cells showed a morphological change in the structures, becoming mainly elongated and perinuclear. To characterize these structures, we first used immuno-CLEM techniques. As shown in Fig. 25, the structures corresponded to extensive zippered areas of the nuclear envelope, which appears thinner and without a lumen. Therefore, K22 mediates an alteration in the compartment formation of NSP6 and its zippering activity, which seems to be shifted toward the nuclear envelope. Further analysis was performed for EM (data not shown).

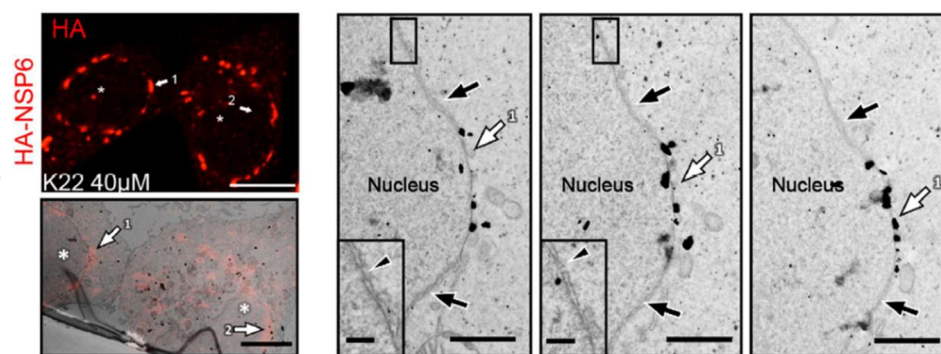


Figure 25. Immuno-CLEM of HA-NSP6-expressing cells treated with K22 for 24 h. Right, Fluoromicrograph showing NSP6 (anti-HA immunostaining) in elongated structures (arrows 1, 2) close to the nucleus (asterisk). Scale bars, 7.5 μm , inset 200 nm. Experiment performed by Lena Polishchuk.

4.6 NSP6(ΔSGF) has a higher ER-zippering activity

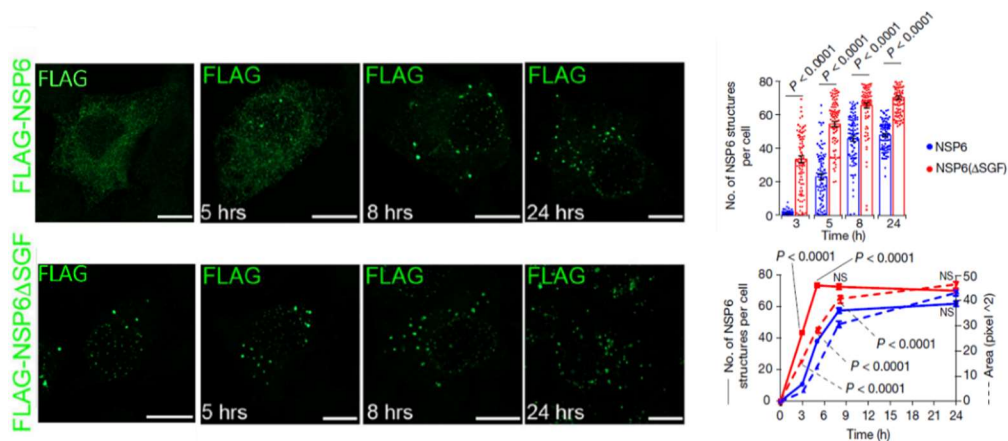


Figure 27. Left, Time course analysis of stably expressing Flag–NSP6 or Flag–NSP6(ΔSGF) cells induced with doxycycline. Fluoromicrographs at 3-5-8-24 h. Right, Quantification of the NSP6-structures. Upper number and areas of NSP6-positive structures. Bottom, NSP6 in structures as a percentage of the total NSP6 in the cell (mean ± s.e.m.). Scale bars, 10 μm. Experiments were performed by Laura Giaquinto.

Comparison of the protein levels of HA-NSP6 and HA-NSP6(ΔSGF) clones induced overnight with doxycycline by Western blot showed that they were expressed equally (data not shown).

To estimate if there was any difference in the half-life of the proteins, an experiment in which HeLa clones induced with doxycycline expressing HA-NSP6 or HA-NSP6(ΔSGF), or the parental cells (CTRL), were radiolabeled for 1 h with 35S-methionine/cysteine and chased for different times. The estimated half-life of both HA-NSP6 and HA-NSP6 (ΔSGF) was 5 h, with no differences between the proteins (data not shown).

Given the propensity of NSP6 (ΔSGF) to form more zippered structures, we decided to perform co-immunoprecipitation experiments in HeLa cells expressing GFP-NSP6 with HA-NSP6, or GFP-NSP6 (ΔSGF) with HA-NSP6 (ΔSGF). The cell lysates (input) were immunoprecipitated (IP) with an anti-HA antibody and probed by WB (Fig. 28). The more efficient immunoprecipitation of NSP6 (ΔSGF) suggests a greater propensity for homodimerization. In addition, we also evaluated resistance to detergent extraction, which was found to be higher in the NSP6 (ΔSGF) (data not shown).

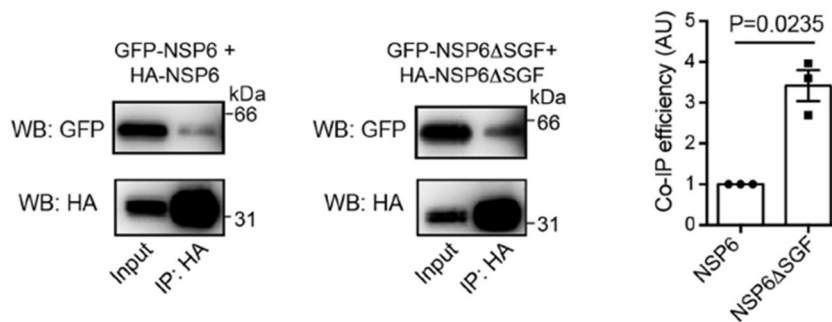


Figure 28. Cell lysates (input) of cells expressing GFP-NSP6 with HA-NSP6, or GFP-NSP6 (Δ SGF) with HA-NSP6 (Δ SGF), were immunoprecipitated (IP) with anti-HA antibody and analyzed by western blot with anti-HA and anti-GFP antibodies. The graph shows the co-IP efficiency of NSP6 (Δ SGF) relative to NSP6, which was set as 1. Mean \pm SEM, Two-tailed unpaired t-test with Welch's correction. Experiments were performed by Andrea Maria Guarino and Giuseppe Di Tullio.

Furthermore, the effect of K22 on NSP6 (Δ SGF) was slightly less sensitive than the reference NSP6 (Fig. 29).

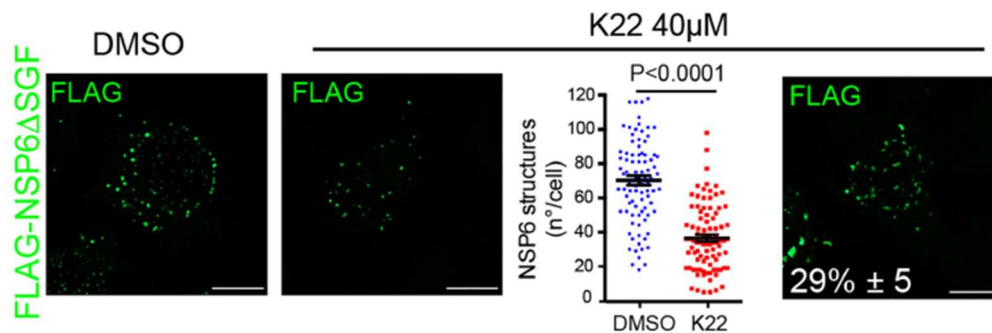


Figure 29. Doxycycline-induced clone expressing Flag-NSP6 (Δ SGF) treated with DMSO or K22 for 24 h. A number of NSP6 structures (middle panel) and cells with elongated NSP6 structures (right panel) induced by K22. The number indicates the percentage (Mean \pm SD) of cells exhibiting the elongated structures. Single values are plotted, Means \pm SEM is shown, and a two-tailed unpaired t-test with Welch's correction. Scale bars, 10 μ m. Experiments were performed by Laura Giaquinto.

Finally, to analyze the morphology of NSP6 (Δ SGF), we used EM, IEM, and CLEM. As shown in Fig. 30, NSP6 (Δ SGF) promotes the formation of both linear and circular zippered membrane compartments as well as NSP6. Morphometric analysis of the IEM revealed an increased association of NSP6 (Δ SGF) with zippered membrane domains, resulting in almost complete elimination from the regular ER.

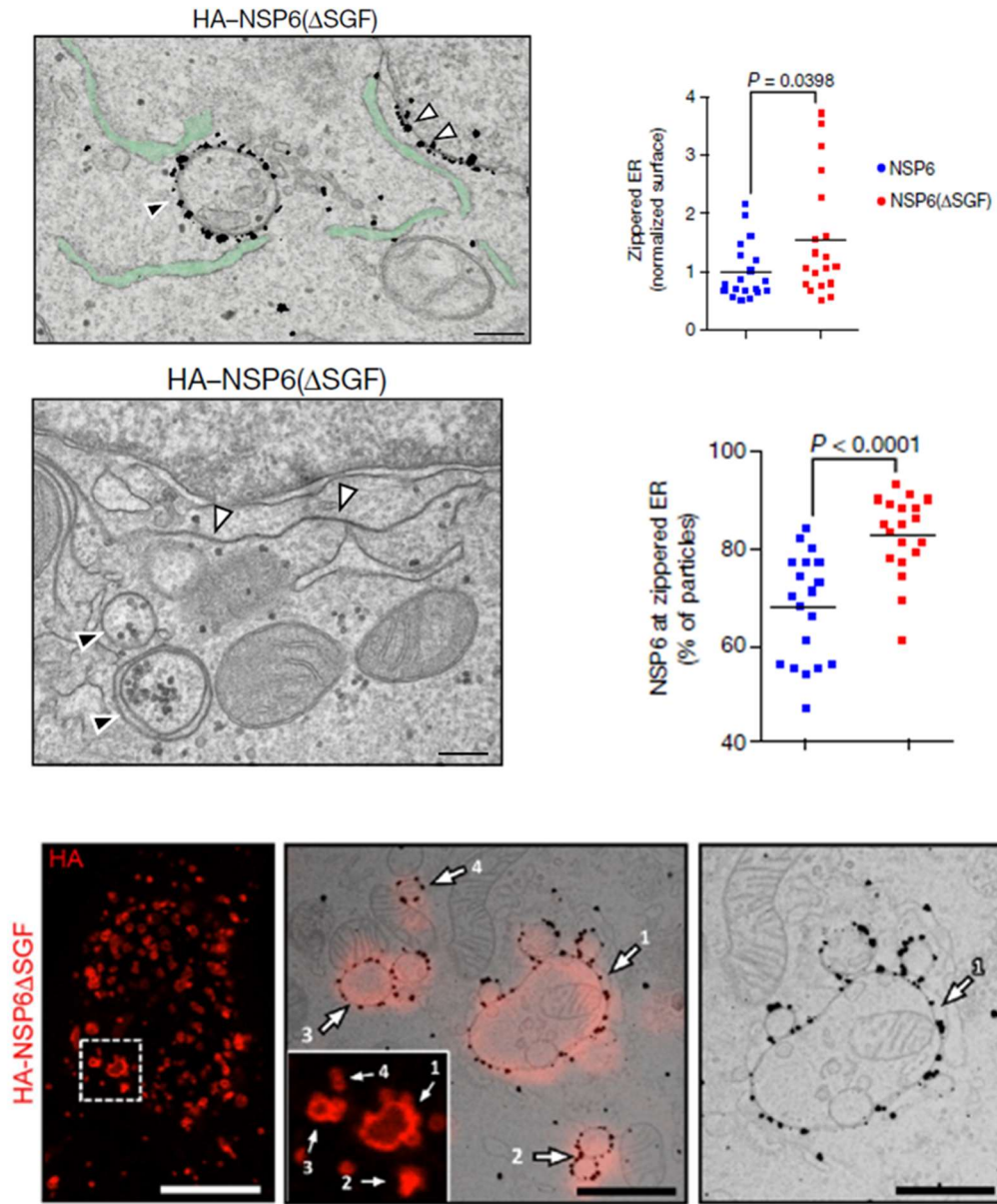


Figure 30. EM (Upper) and IEM (Middle) anti-HA immunolabelling of HA-NSP6(Δ SGF)-expressing HeLa cells. White arrowheads, linear zippered ER structures; black arrowheads, circular zippered ER structures. The regular ER is shown in green. Upper (Right), Morphometric analysis of IEM images. Quantification of gold particles at zippered ER. Middle (Right), the surface area of zippered ER normalized for the total number of gold particles. Bottom, Immuno-CLEM of cells expressing HA-NSP6(Δ SGF) with inset. and IEM, in which arrows 1–4 indicate overlap of the fluorescent and immuno-gold signals in the zippered NSP6-positive-structures. g, magnification of the structure indicated by arrow 1. Scale bars, 250 nm; 3.7 μ m; 480 nm; 250 nm. Unpaired two-tailed t-test. Experiments were performed by Roman and Lena Polishchuk.

During viral infection, NSP6 is generated by cleavage from the polyprotein by the NSP5 protease¹⁰⁶ (itself a part of the polyprotein) which cleaves between NSP5/6 and NSP6/7. Because we have shown that NSP6 forms the compartment only if its C-terminal is "free," we decided to compare the zipping activity of NSP6 and NSP6(Δ SGF) by comparing their putative precursors, namely NSP6-NSP7 and NSP6(Δ SGF)-NSP7. Cells were transfected with FLAG-NSP6-NSP7-V5, where the protein shows not only an ER distribution but also partial localization at the Golgi, suggesting that the precursor might visit the Golgi before cleavage triggers its ER zipping activity. In contrast, in FLAG-NSP6(Δ SGF)-NSP7-V5 transfected cells, the protein shows a purely ER localization and forms small round structures even before cleavage, supporting the enhanced ER-zipping activity of NSP6(Δ SGF) (data not shown).

4.7 NSP6 connects DMVs with the ER

NSP6 is one of the proteins involved in RO formation along with NSP3 and NSP4. Because of the similarity of the ER zipper with the "ER connectors" between ER and DMVs in SARS-CoV-2-infected cells⁶⁶, we analyzed the relationship between NSP6 and DMVs.

First, HeLa cells were transfected with HA-NSP3 and mCherry-NSP4 alone and then co-expressed to assess their cellular localization.

When NSP3 and NSP4 are expressed alone, they have a diffuse distribution in the ER, but when they are co-expressed, they colocalize completely in point structures (Fig. 31a, b). To understand the morphology of these structures, EM analysis was performed on cells co-expressing HA-NSP3 and mCherry-NSP4. EM images revealed that these structures correspond to clusters of vesicles with a diameter of 50-100 nm, surrounded by two membranes (DMVs), with a visible intermembrane space (Fig. 31c).

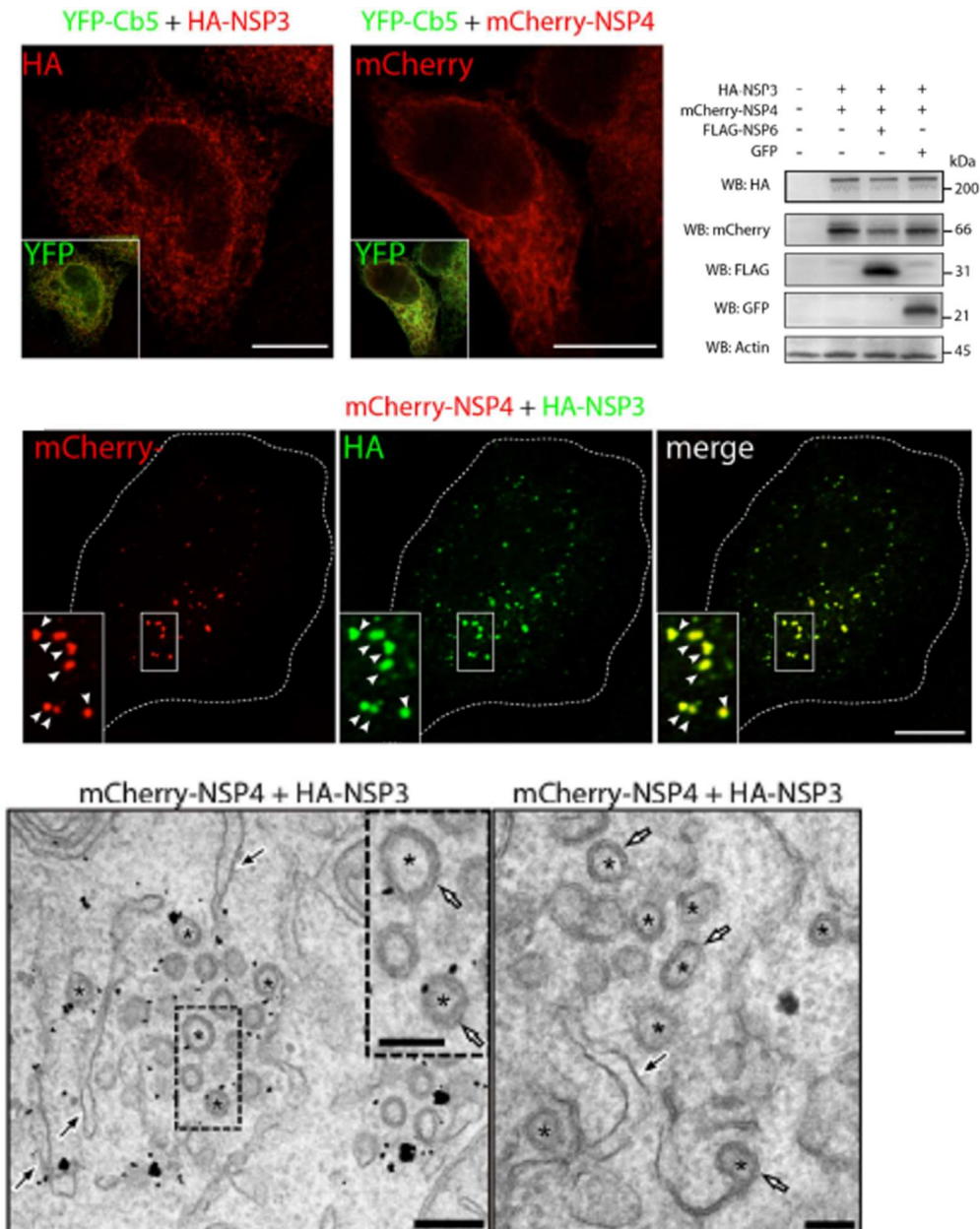


Figure 31. Upper, Fluoromicrographs of HeLa cells expressing YFP-Cb5 with HA-NSP3 (anti-HA immunostaining) or mCherry-NSP4. Insets merge with YFP-Cb5. Upper (right), Western blot (WB) of total lysates from HeLa cells expressing HA-NSP3, mCherry-NSP4, Flag-NSP6, or GFP as indicated. Actin was used as a loading control. Middle, Fluoromicrographs of HeLa cells expressing HA-NSP3 and mCherry-NSP4. Insets, enlargement of the boxed area. Arrowheads, NSP3/NSP4-positive structures. Dashed lines delineate cell boundaries. Bottom, IEM of HeLa cells co-transfected with HA-NSP3 and mCherry-NSP4. Anti-HA labeling shows gold particles decorating DMVs, indicated by asterisks. Black arrows, ER. Inset, magnification of boxed area. White arrows in d and e show double membranes. The average DMV size is 92 ± 30 nm. Scale bars, 10 μ m.

Therefore, from the results obtained, NSP3-NSP4 and NSP6 can individually reproduce the two main features of SARS-CoV-2: DMV and connectors. To understand the relationship between these three proteins, HA-NSP3, mCherry-NSP4, and Flag-NSP6 were co-expressed in HeLa and Calu-3 cells. Immunofluorescence analysis of the combined expression of all three membrane NSPs showed that the spots of NSP3-NSP4 are always in close proximity to the NSP6 compartment, but never overlapping with it (Fig. 32).

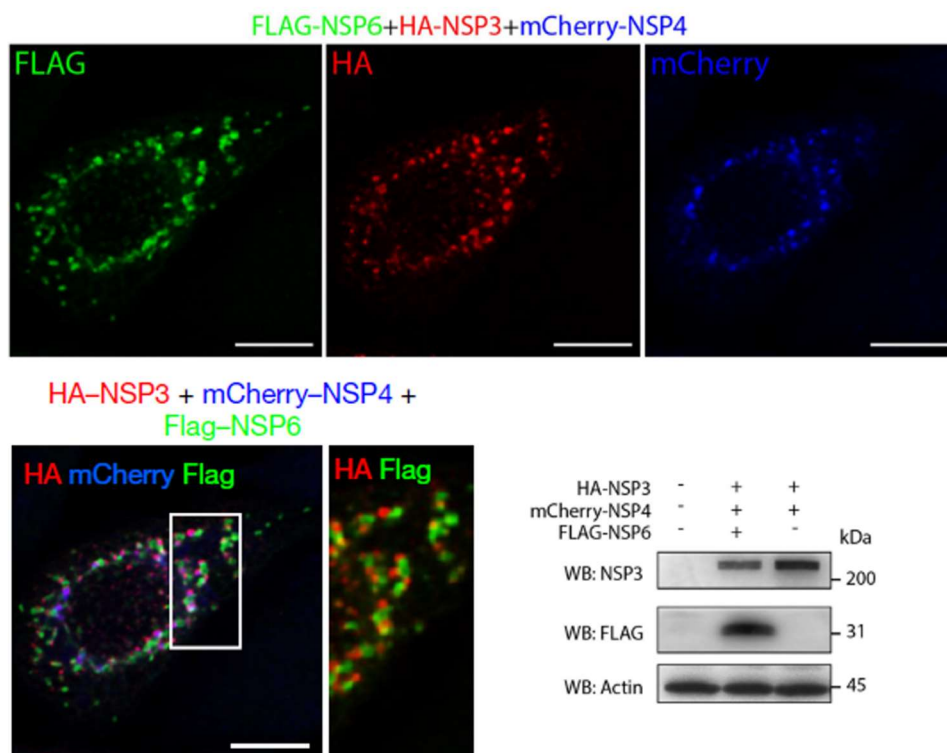


Figure 32. Upper, Individual fluoromicrographs of a Calu-3 cell co-transfected with Flag-NSP6, HA-NSP3, and mCherry-NSP4. Bottom, The enlargement of the boxed area shows HA and Flag immunolabelling. Bottom, (right), Western blot of total lysates from HeLa cells expressing HA-NSP3, mCherry-NSP4, or Flag-NSP6 as indicated. Actin was used as a loading control. Scale bars, 10 μ m.

To corroborate the results obtained by transient transfection of NSPs, Calu-3 cells were infected, by the group of Patricia Bozza with whom we collaborated, with an early line or gamma variant of SARS-CoV-2. Subsequently, NSP3 and NSP6 were labeled with antibodies (Fig. 33). From the results obtained, NSP3 spots are near the NSP6 compartment, suggesting that simple transfection of NSPs proteins can serve as a tool to reproduce the phenotype of infected cells.

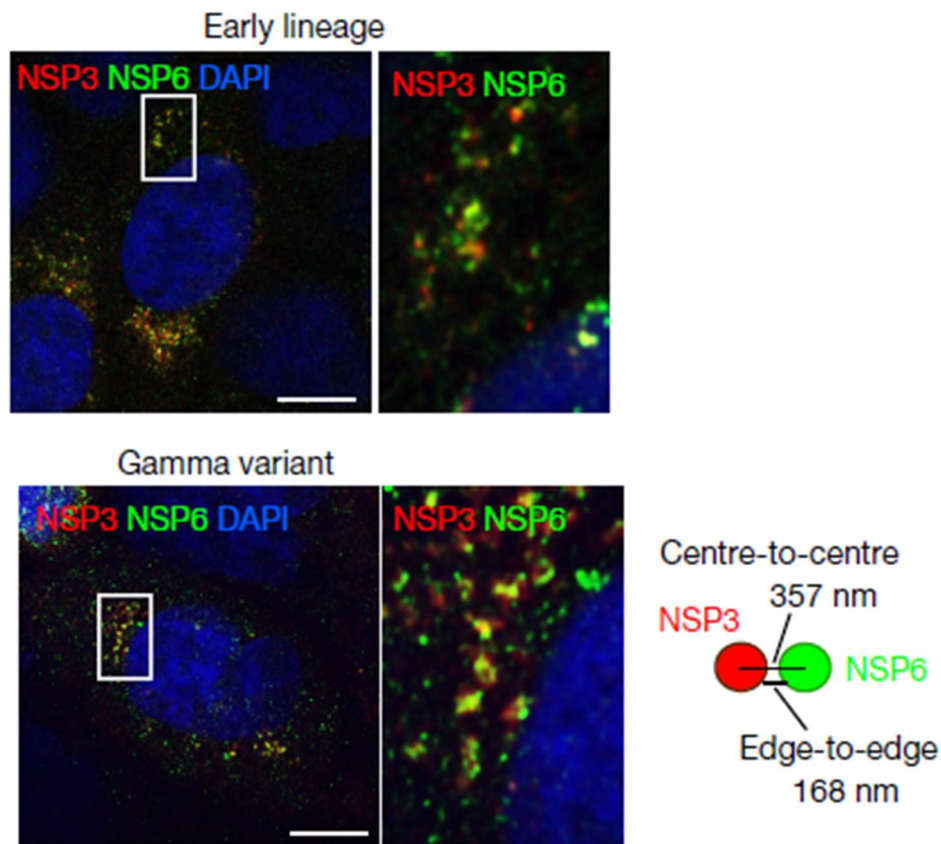


Figure 33. Calu-3 cells infected with early lineage and Gamma variant SARS-CoV-2. Values represent mean NSP3- and NSP6-structure distances in nm. Scale bars, 10 μ m.

To analyze the morphology of the structures detected by immunofluorescence, CLEM was performed on cells co-expressing HA-NSP3, mCherry-NSP4, and GFP-NSP6. The dots of NSP3-NSP4 corresponded to clusters of DMVs, while the structures of NSP6 corresponded to zippered ER tracts, which were distinct but often close and connected to DMVs (Fig. 34).

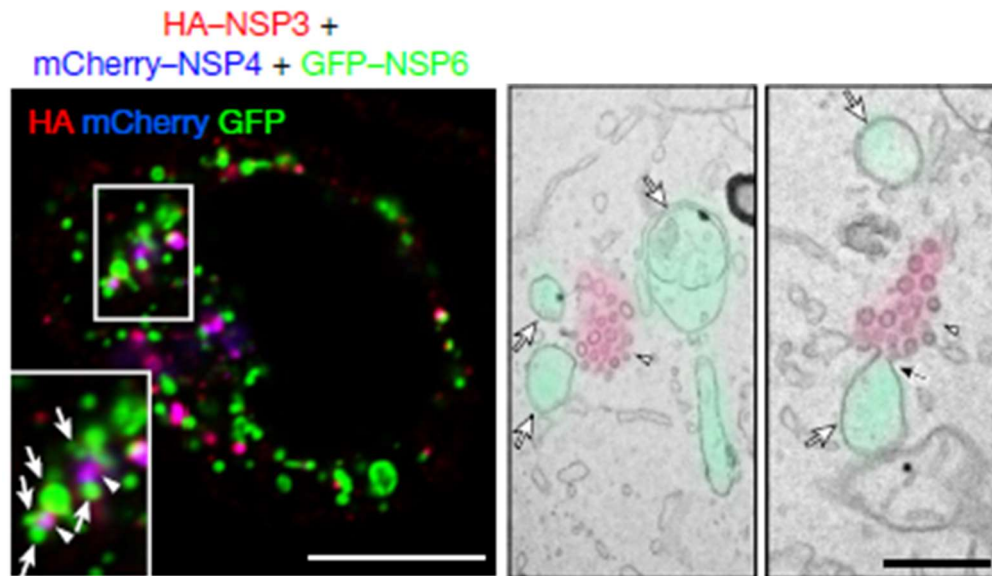


Figure 34. Left Fluoromicrograph and Right EM serial section of an HA-NSP3 + mCherry-NSP4 + GFP-NSP6-expressing cell. Arrowheads, NSP3/NSP4 co-localization; arrows, NSP6 compartments; black arrow, NSP6 compartment connection with NSP3/NSP4 DMVs. Scale bars, 10 μ m (a); 470 nm (b). Experiments were performed by Lena Polishchuk.

In addition, immuno-EM analysis revealed that clusters of NSP3-NSP4-positive DMVs were associated with NSP6-positive zippered ER membranes. The DMVs appeared to be organized in "graph-like" clusters, sometimes with reciprocal connections. Sections of zippered ER formed connections between the DMV clusters and the regular ER, similar to those observed in SARS-CoV-2-infected cells⁶⁶. NSP6-induced zippered connectors would be able to ensure membrane-selective continuity of the replication niche with the ER.

4.8 NSP6 organizes the DMVs cluster

Since we observed that NSP6 zippered structures directly connect DMV clusters to the ER, we asked if there might be functional consequences of these connections. HeLa cells were transfected with NSP3-NSP4 or NSP3-NSP4-NSP6 and DMVs were analyzed by immunofluorescence, assessing their

number and distribution. Notably, NSP3-NSP4 spots were more numerous and more homogeneously distributed in the cytoplasm of cells expressing NSP3-NSP4-NSP6, both with the WT NSP6 and the NSP6 (Δ SGF) version, than those expressing just NSP3-NSP4, suggesting that NSP6 might provide a cue for the positioning and organization of DMVs (Fig. 35).

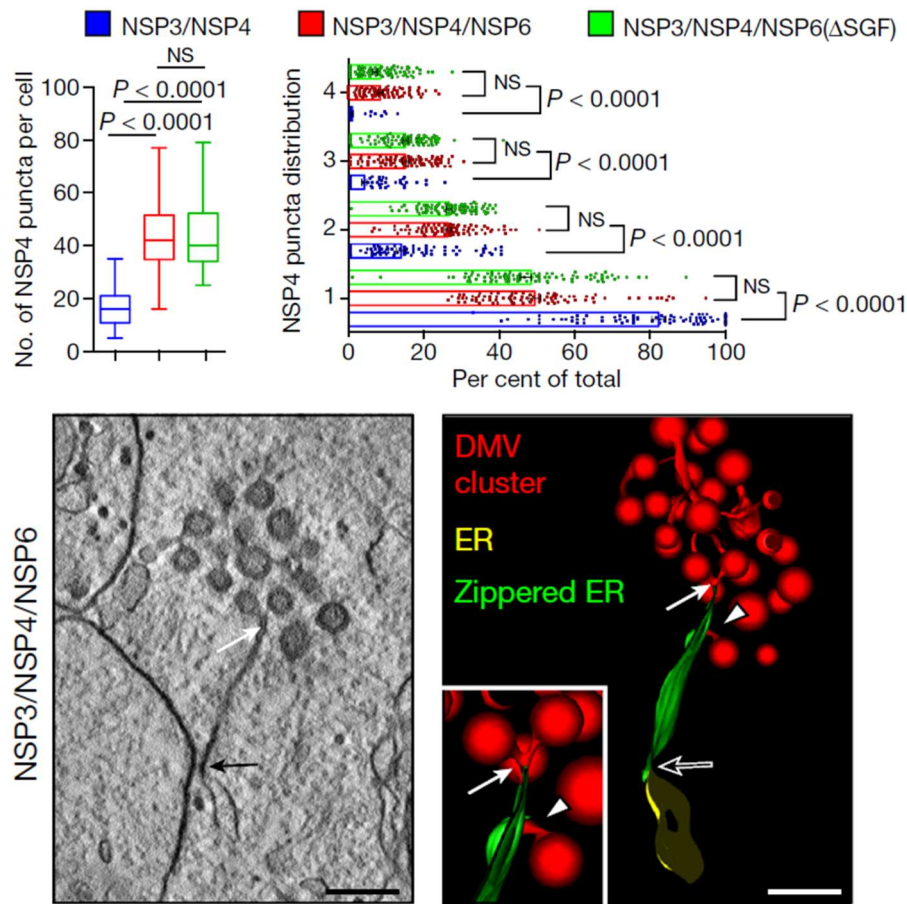


Figure 35. Upper Number, and distribution of NSP4 puncta in cells expressing the indicated NSPs. Tomogram (Bottom) and three-dimensional (3D) reconstruction showing connections of zippered ER to DMVs (white arrow and arrowhead) and the regular ER (black arrow). Box plots represent the 25th to 75th percentiles of the data. Scale bars, 160 nm. One-way ANOVA with Tukey's or Emmeans posthoc test. Tomographic analysis was performed by Roman Polishchuk.

In addition, the same cells were analyzed by electron tomography, which revealed that in the absence of NSP6, the connections of the DMVs with the ER were short and tubular with a clearly detectable lumen (Fig. 36).

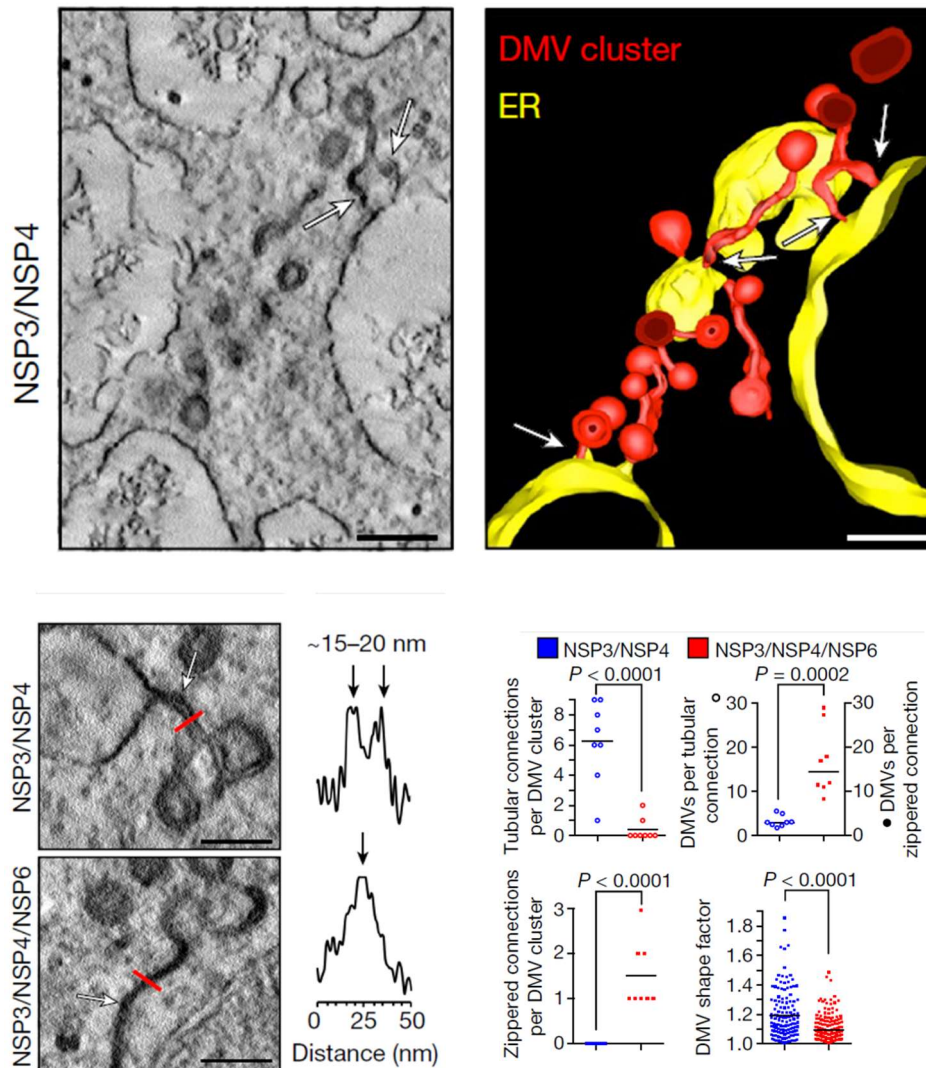


Figure 36. Upper Tomograms and 3D reconstruction showing multiple short DMV–ER tubular connections (white arrows) in an NSP3/NSP4-expressing cell. Bottom, Tomograms from NSP3/NSP4 and NSP3/NSP4/NSP6-expressing cells showing DMV–ER connections (arrows). Bottom middle, Intensity profiles along the red lines., Bottom right, Morphometry of NSP3/NSP4- or NSP3/NSP4/NSP6-expressing cells. Scale bars, 160 nm; 100 nm. Unpaired two-tailed t-test. Tomographic analysis was performed by Roman Polishchuk.

By contrast, in the presence of NSP6, DMV clusters were connected to the ER through much longer sheet-like zippered domains, as shown in Fig 36. The number of DMVs per connection was also different: an average of about 3 DMVs per tubular connection without NSP6 and about 15 DMVs per zippered connection with NSP6. In addition, the shape of DMVs was more regular, their

size more uniform, and their packing within each cluster was denser in the presence of NSP6 (Fig. 37).

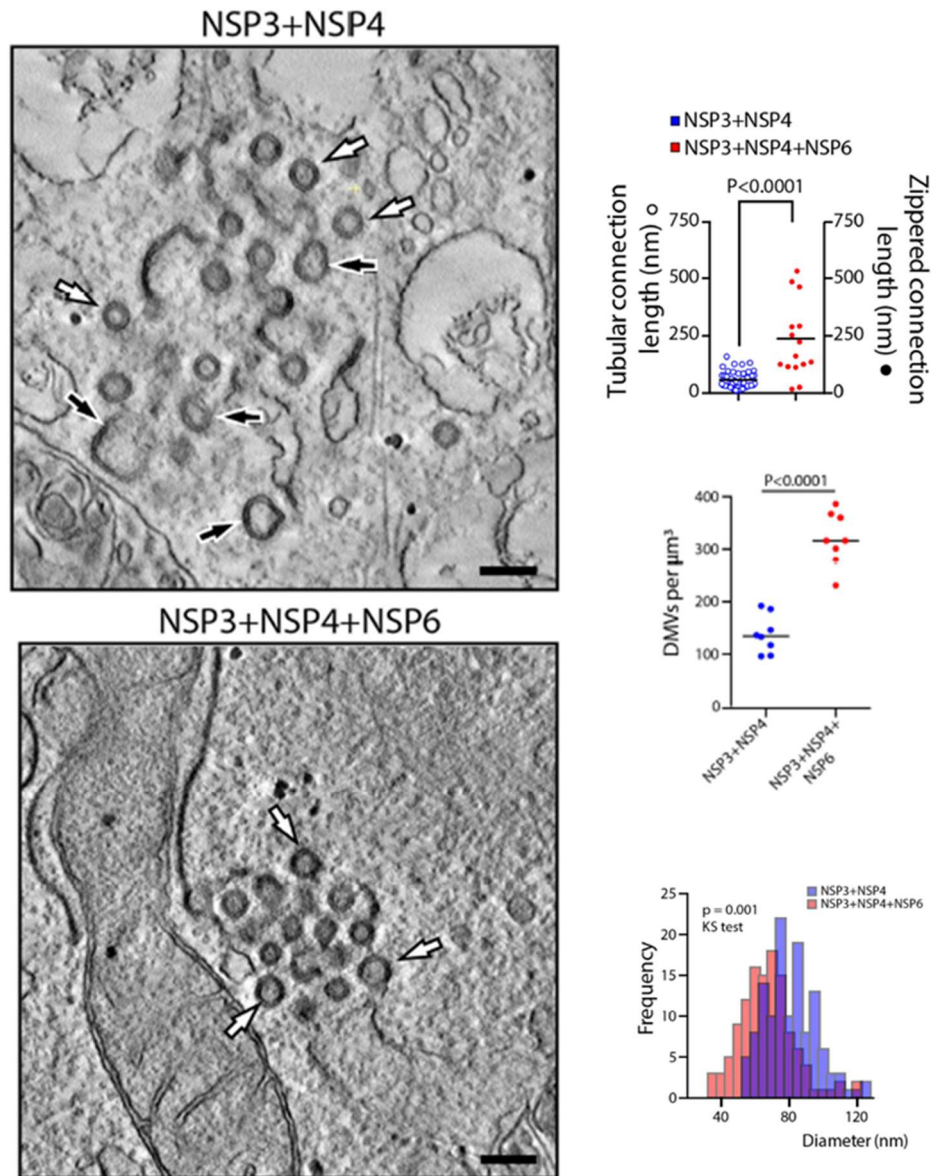


Figure 37. Upper, Tomographic slice of a HeLa cell expressing HA-NSP3/mCherry-NSP4 or HA-NSP3/mCherry-NSP4/Flag-NSP6, showing DMV clusters with regular round DMVs (white arrows) and large and elongated DMVs (black arrows). Upper right, Length of DMV-ER tubular or zippered connections in NSP3/NSP4 or in NSP3/NSP4/NSP6-expressing cells, respectively. Single values are plotted. Medians are shown ($n \geq 14$ connections), two-tailed unpaired t-test. Middle graph, DMV densities were calculated in tomograms as the number of vesicles per μm^3 in a volume occupied by a DMV cluster; Single values are plotted, Median is shown, and a two-tailed unpaired t-test. Bottom graph, Frequency histograms of DMV diameter measured from tomograms of cells expressing NSP3/NSP4 (average diameter 80.87 nm) or NSP3/NSP4/NSP6 (average diameter 67.50 nm). Nonparametric Kolmogorov-Smirnov (KS) test. $n \geq 135$ vesicles. Scale bar, 180 nm. Experiment performed by Roman Polishchuk.

These results indicate that co-expressed NSP3-NSP4-NSP6 produce DMV clusters that reproduce replication-like structures (ROLS) and that NSP6 organizes these clusters.

4.9 K22 blunts the activity of NSP6 on DMVs and interferes with SARS-CoV-2 replication

Because K22 treatment showed altered zippering activity of NSP6, its effect was also analyzed on ROLS. HeLa cells were transfected with NSP3-NSP4 or NSP3-NSP4-NSP6 and treated with 40 uM K22 overnight. The cells were then analyzed by immunofluorescence to determine any effect on the number and distribution of NSP3-NSP4-positive spots (Fig. 38). No effect was observed on the number and distribution of spots in cells transfected with NSP3-NSP4. In contrast, in cells transfected with NSP3-NSP4-NSP6, no increase in NSP3-NSP4 spots was observed, suggesting that NSP6 activity was interfered with by K22 treatment.

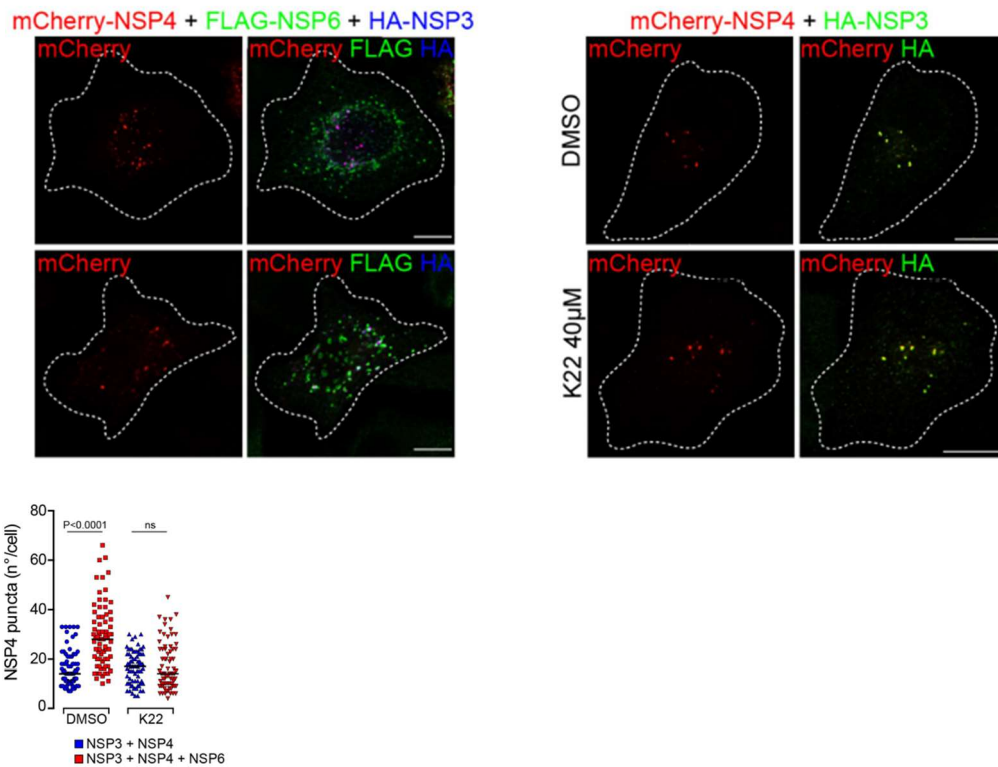


Figure 38. Upper, HeLa cells transfected with HA-NSP3 and mCherry-NSP4 for 5 h were further transfected or not with Flag-NSP6 and treated with DMSO or K22 (40 μ M, 16 h) followed by immunostaining as indicated. Bottom, Quantification of the number of NSP4 puncta/cell. Single values are plotted. The median value is shown. One-way ANOVA test with Tukey's posthoc. ns, not significant. Scale bar, 10 μ m.

In addition, analysis conducted by EM in cells transfected with NSP3-NSP4-NSP6 with K22 treatment revealed that DMV clusters in these cells contained significantly fewer vesicles with a less regular shape that lost zippered connections (Fig. 39).

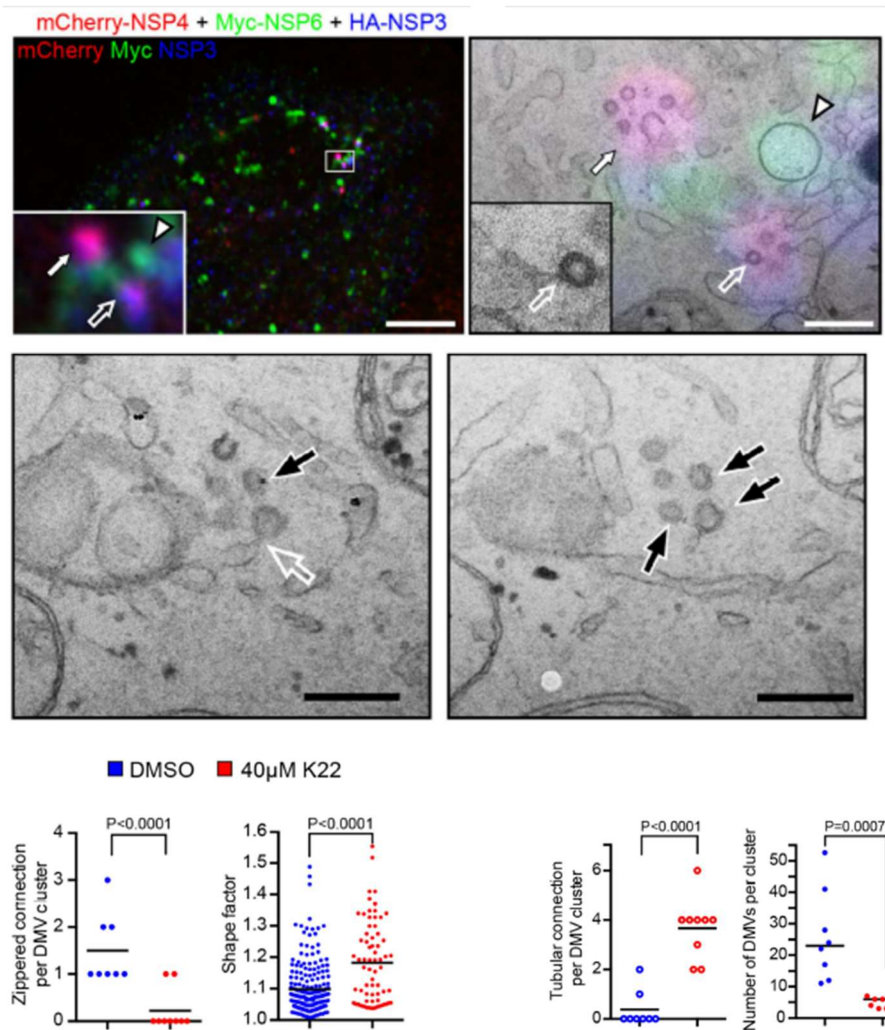


Figure 39. CLEM analysis of K22-treated cells. Upper, Fluoromicrograph of HeLa cell expressing HA-NSP3, mCherry-NSP4, and Myc-NSP6. The inset corresponds to the boxed area and shows NSP3/NSP4-positive structures (arrows) close to the NSP6 compartment (arrowhead). The NSP6 compartment corresponds to a circular zippered ER structure (arrowhead) close to but not connected with the NSP3/NSP4 puncta that correspond to DMVs (arrows). The empty arrow indicates a tubular connection of a DMV to the regular ER (magnified in the inset). Middle, Ultrastructure of DMV clusters in K22-treated cells expressing HA-NSP3, mCherry-NSP4, and Myc-NSP6. Serial sections show a DMV cluster with irregular elongated DMVs (black arrows). The empty arrow indicates a tubular connection of a DMV with a regular ER. Bottom, Morphometric analysis of serial sections from untreated (NT) and K22-treated cells to quantify the number of DMVs per cluster, DMV shape factor, and the number of tubular or zippered connections per DMV cluster. Single values are plotted, Medians are shown, and two-tailed unpaired t-tests. scale bar, 4.4 μm ; 370 nm; 320 nm. CLEM analysis was performed by Lena Polishchuk.

To confirm and corroborate these results, Calu-3 SARS-CoV-2 infected cells were treated with K22. We found that K22, at the (relatively high) concentration

of 40 μM , but not at lower concentrations¹⁰⁷, interferes with ROLS biogenesis, inhibiting SARS-CoV-2 replication (Fig. 40).

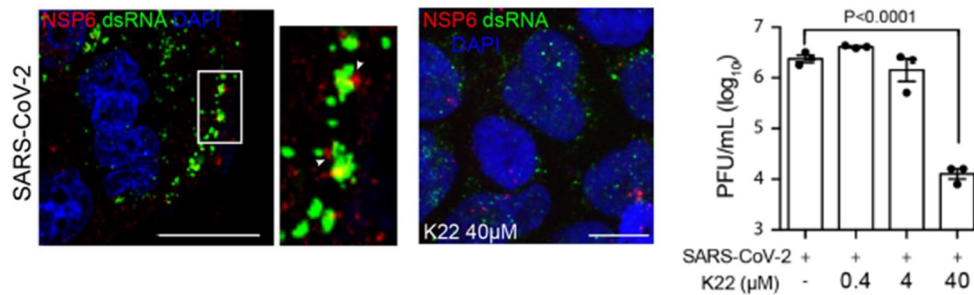


Figure 40. Antiviral activity of K22. Calu-3 cells infected with SARS-CoV-2 without (left panels) or with (right panel) K22 treatment. Right, cells were immunostained for dsRNA and NSP6. Nuclei were stained with DAPI. Scale bar, 20 μm . Experiment was performed by Patricia Bozza.

4.10 NSP6 (ΔSGF) exerts more organization on DMVs than the reference one

To analyze the effect of NSP6 (ΔSGF) on DMVs, HeLa cells were co-transfected with NSP3-NSP4-NSP6 (ΔSGF). From EM and tomographic analysis, NSP6 (ΔSGF) also enhances and organizes NSP3-NSP4 puncta formation. In particular, each DMV cluster contains a more significant number of DMVs of a more homogeneous size, showing a more developed zippered connection system than the reference NSP6 (Fig. 41).

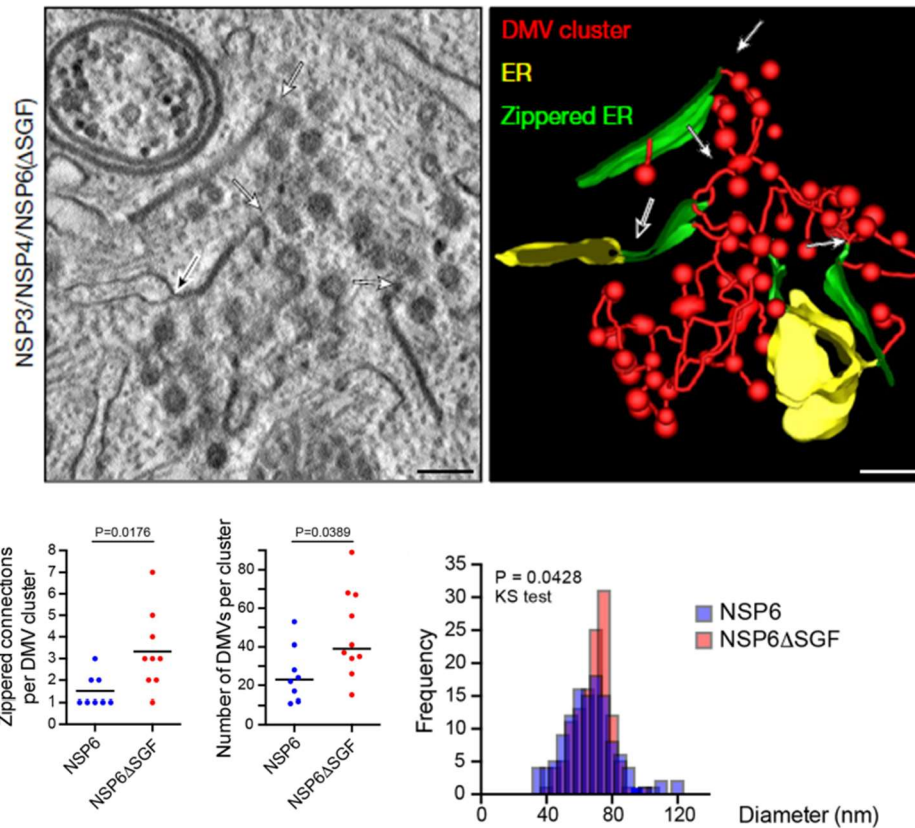


Figure 41. Upper, Tomogram and 3D reconstruction of an NSP3/NSP4/NSP6(Δ SGF)-expressing cell, showing numerous zippered ER domains connected to DMVs (white arrows) and regular ER (black arrows). Bottom, quantification of the number of ER zippered connections per DMV cluster and number of DMVs per cluster. Single values are plotted, and Medians are shown. Bottom right, Frequency histograms of DMV diameter measured from tomograms of cells expressing NSP3/NSP4/NSP6 (average diameter 67.50 nm) or NSP3/NSP4/NSP6(Δ SGF) (average diameter 68.51 nm). The histograms were analyzed using the non-parametric Kolmogorov-Smirnov (KS) test. $n \geq 123$ vesicles. Two-tailed unpaired t-test. Scale bar, 160 nm. Tomographic analysis was performed by Roman Polishchuk.

Finally, to understand whether the effect of NSP6 deletions could increase the formation of zippered connectors in infected cells, these structures were compared in an early line and the Gamma SARS-CoV-2 variant (which contains the SGF deletion in NSP6) in Calu-3-infected cells by EM analysis.

Notably, the Gamma strain showed a much more extensive zippered connector system linking DMVs to each other and the ER (Fig. 42). It could be hypothesized that the enhanced zippered closure activity of NSP6 (Δ SGF) plays a role in creating a more functional and better-shielded replication organelle, providing one of the multiple mechanisms contributing to the reported

differences in replication dynamics and immune evasion of NSP6 (Δ SGF)-carrying VOCs^{108,109}.

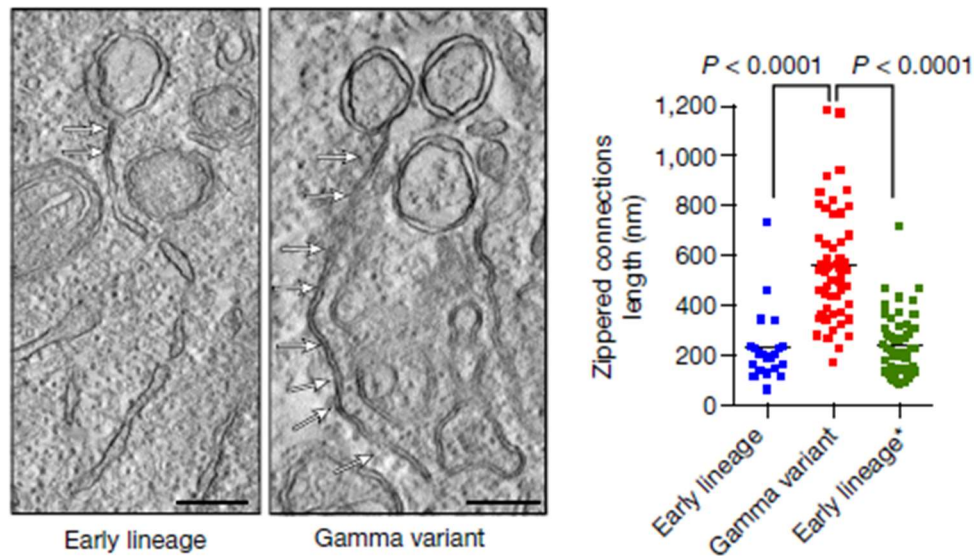


Figure 42. Left, Tomograms showing zippered ER connections (arrows) to DMVs in Calu-3 cells infected with early lineage and Gamma variant SARS-CoV-2. Right, Length of zippered ER connected to DMVs in infected cells ($N = 10$, $n \geq 20$), and from early lineage* (Bavpat1/2020) data in EMPIAR-10490 (29 tomograms). Scale bars, 200 μ m. EM analysis was performed by Roman Polishchuk.

4.11 NSP6 mediates replication organelle-LD association

As previously noted, the C-terminal tail of NSP6, specifically an 80-amino acid fragment (NSP6-C80), cannot induce the formation of the NSP6 compartment. This deletion form of NSP6-C80 was expressed in HeLa cells and showed association with a compartment of round cytoplasmic structures.

To understand the localization of NSP6-C80, differential staining for endosomes, Golgi, and mitochondria was performed but was found to be

negative. Surprisingly, NSP6-C80 appeared to colocalize completely with the lipid droplets (LDs) (Fig. 43).

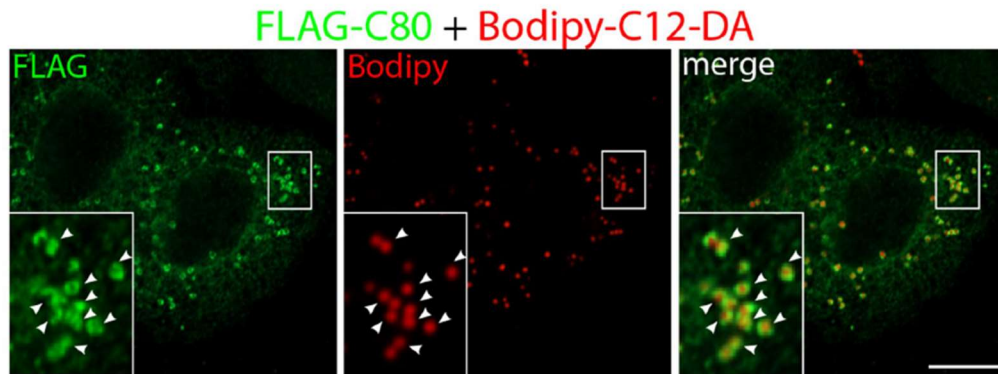


Figure 43. Fluoromicrographs of HeLa cells expressing Flag-NSP6-C80 (i.e., the last 80 amino acids of NSP6). Anti-Flag antibody and staining for LDs using BODIPY C12. Insets, enlargement of boxed areas. Arrowheads, colocalizing structures. Scale bars, 10 μ m.

Interestingly, in HeLa cells expressing the mutated version of NSP6-C80 (NSP6-C80(F220Q/T222W)) that lost the amphiphilic properties of its amphipathic helix, no association with LDs was observed, showing a diffuse distribution, suggesting that this association is due to the amphipathic helix (Fig. 44).

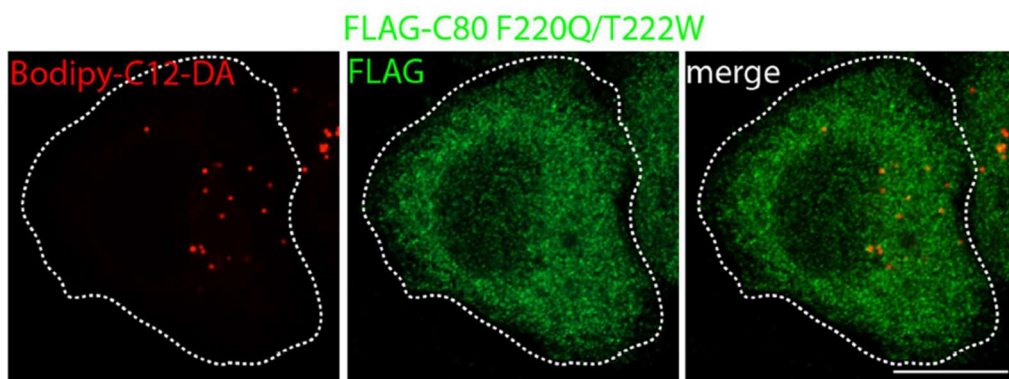


Figure 44. NSP6-C80 mutated in residues that abrogate the amphiphilic properties of the AH fail to associate with LDs. Cells were immunostained with anti-Flag Ab (green) and BODIPY-DA-C12 (red). Scale bars, 10 μ m.

To better characterize the role of LDs in viral replication, we found that 40% of the areas of viral replication labeled by double-stranded RNA (dsRNA) and NSP6 are associated with LDs in Calu-3 cells infected with SARS-CoV-2. Furthermore, the DGAT-1 inhibitor A922500-a inhibited LD biogenesis and significantly reduced viral load, suggesting that LDs are required for SARS-CoV-2 replication in Calu-3 cells (data not shown).

Next, to characterize the ratio of LDs and NSPs, HeLa and Calu-3 cells were co-transfected with NSP3-NSP4-NSP6, NSP3-NSP4, or NSP6 and analyzed by LD staining. As observed in the infected cells, LDs were found in the vicinity of ROLS but not in cells expressing only NSP3-NSP4. Interestingly, LDs were located very close to NSP6 structures in cells expressing only NSP6, indicating that the association of LDs with ROLS is mediated by NSP6, as shown in Fig. 45.

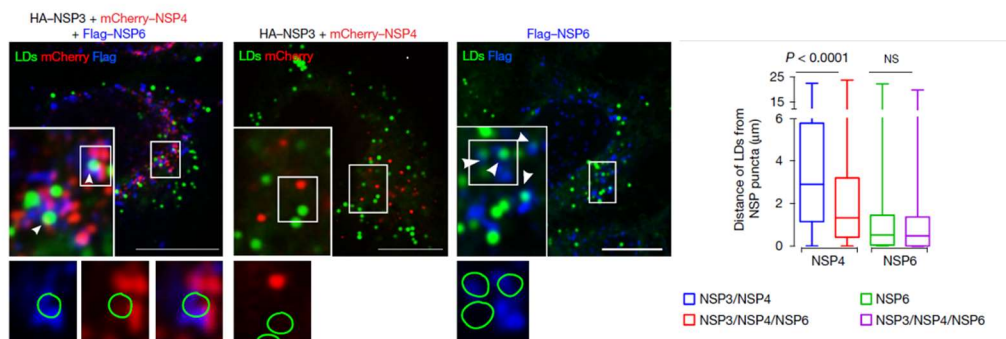


Figure 45. Left, HeLa cells expressing the indicated NSPs stained with BODIPY-488 for LDs (green). Insets, enlargement of the boxed area; arrowheads, LDs close to ROLS (left) to NSP6 (right). Bottom panels and green circles delineate the position of LDs. Right, the Distance of LDs from NSP4 and NSP6 puncta was measured in whole cells expressing the indicated NSPs. LD to NSP4 puncta. Scale bars, 10 µm, Box plots represent the 25th to 75th percentiles of the data (center line, median; whiskers, minima, and maxima).

4.12 DFCP1 tethers LDs to the ROLS compartment

We examined several proteins among the various molecular actors that could promote the association of LDs with the reticular membranes of which ROLS is composed^{110,111}. We found the involvement of DFCP1 and RAB18 (Fig. 46). Specifically, in HeLa cells co-transfected with NSP3-NSP4-NSP6-DFCP1, DFCP1 was recruited by NSP6; differently, it was not recruited on NSP3-NSP4 structures in cells co-transfected with NSP3-NSP4-DFCP1. Similarly, in HeLa cells co-transfected with RAB18 and NSP6, RAB18 turns out to be fully recruited on the structures of NSP6 (data not shown).

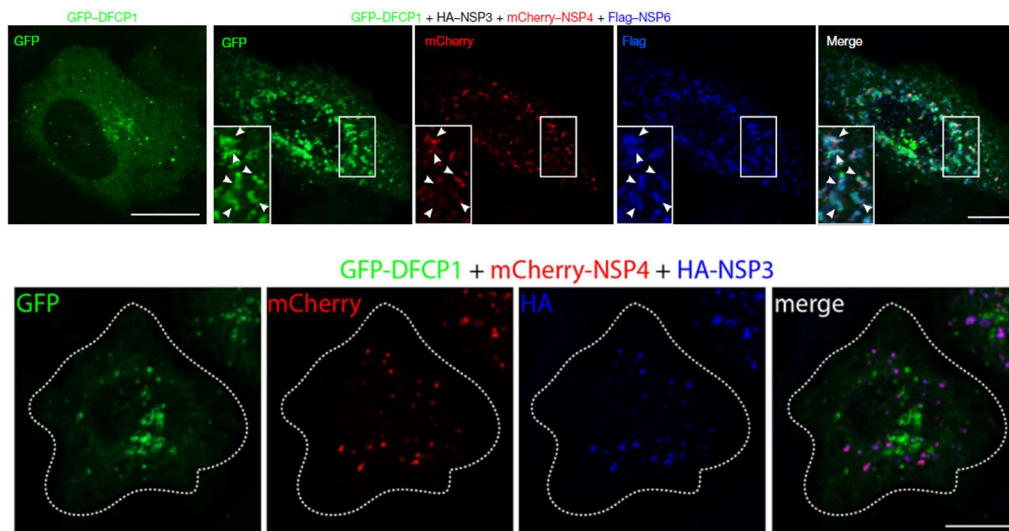


Figure 46. HeLa cells expressing GFP-DFCP1 alone or with mCherry-NSP4 + HA-NSP3 + Flag-NSP6. Arrowheads, DFCP1 signal in the NSP6 compartment. Bottom, Individual fluoromicrographs and merge of cells co-expressing GFP-DFCP1, mCherry-NSP4, and HA-NSP3 (anti-HA immunostaining). Scale bars, 10 μ m.

The interaction between NSP6 and DFCP1 was further confirmed by the intense FRET signal measured in cells expressing GFP-NSP6 and mCherry-DFCP1. Through biochemistry experiments, the ability of DFCP1 to pull down NSP6 from the lysates of cells expressing HA-NSP6 was confirmed (data not shown).

Interestingly, co-transfection of NSP6(1-157) and DFCP1 does not show recruitment of DFCP1 onto NSP6, suggesting that it is the C-terminal domain of NSP6 that mediates recruitment (Fig. 47).

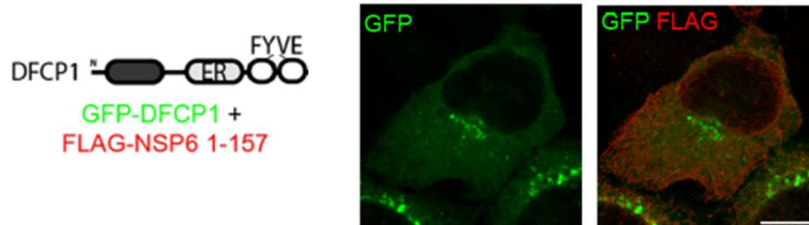


Figure 47. Fluoromicrographs of cells co-expressing GFP-DFCP1 and Flag-NSP6(1–157). Scale bar, 10 μ m.

4.13 DFCP1 recruitment to NSP6 structures is independent of PtdIns3P

Since DFCP1 is known to play a role in autophagy, particularly in omegasome biogenesis through a phosphatidylinositol 3-phosphate-dependent process (REF), we wanted to ascertain whether the recruitment of DFCP1 on NSP6 structures behaved similarly. Therefore, we generated a mutant of DFCP1 (DFCP1(Δ 1-416)) that lacks the N-terminal domain but includes the ER-targeting domain and the two FYVE domains¹¹². We co-transfected HeLa cells with Flag-NSP6 and mCherry-DFCP1(Δ 1-416), and observed that they are still recruited to the NSP6 compartment. We subsequently generated the FYVE domain mutant C654S/C770S, which cannot bind phosphatidylinositol 3-phosphate (PtdIns3P), which, co-transfected with NSP6, still shows recruitment onto the NSP6 compartment. Finally, the single point mutant W543A in the ER domain, when co-transfected with NSP6, is no longer recruited to NSP6-positive structures (Fig. 48).

Thus, unlike recruitment to the omegasome (the site of autophagosome formation), recruitment of DFCP1 to the ROLS is independent of PtdIns3P.

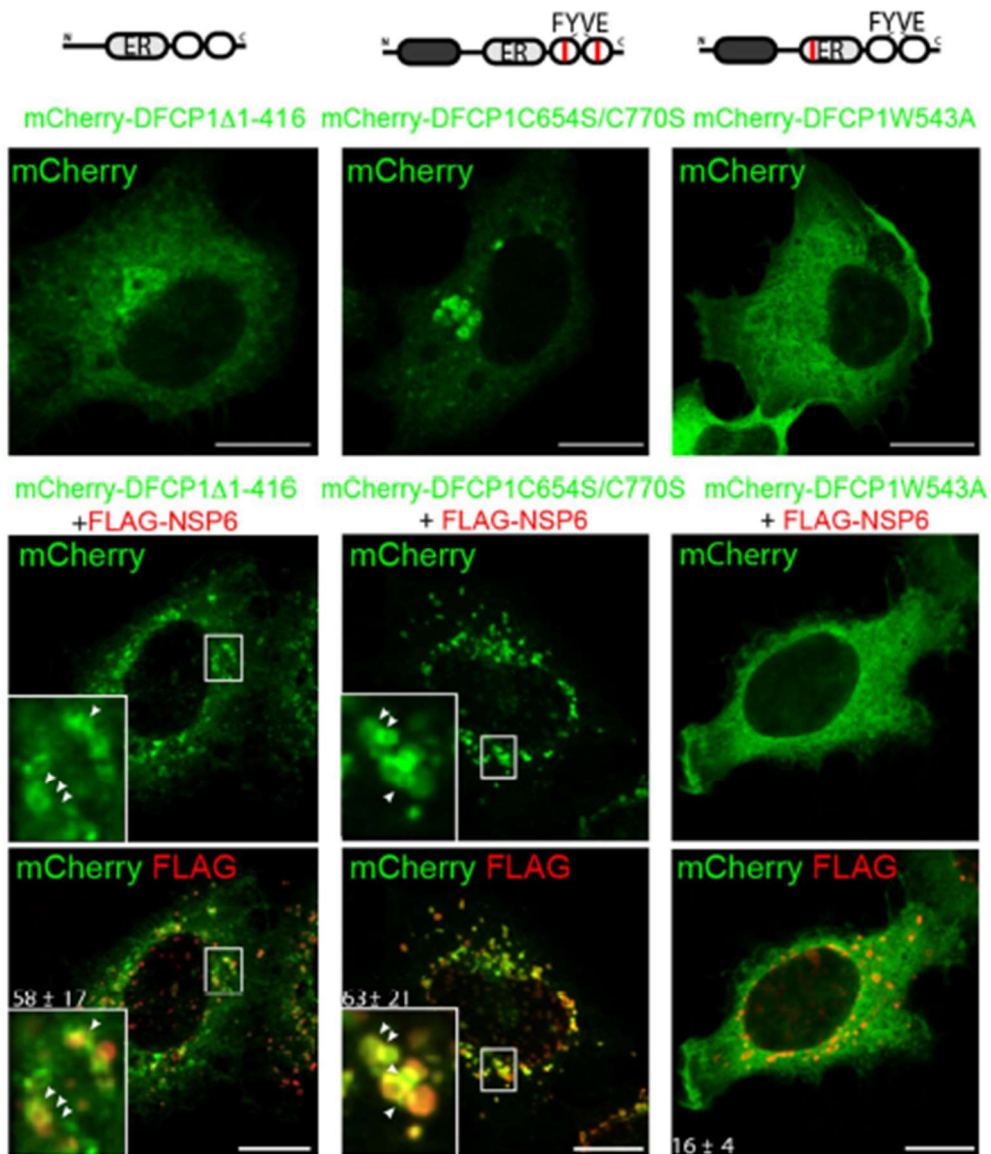


Figure 48. Fluorescent images of HeLa cells transfected with the indicated DFCP1 mutants alone or in combination with NSP6 (as shown). A schematic representation of DFCP1 mutants is reported on top. Arrowheads, DFCP1 signal in the NSP6 compartment. Insets, an enlarged merge of boxed areas. Numbers indicate the percentage of colocalization between DFCP1 mutants and NSP6. Mean \pm SD. Scale bar, 10 μ m.

Furthermore, we treated cells co-expressing NSP6 and DFCP1 with PI3K inhibitors wortmannin or SAR405, preventing the generation of PtdIns3P (Fig. 49). We found that treatment did not affect the recruitment of DFCP1 to the NSP6 compartment. SAR405 did not impair NSP6 compartment formation, which excludes a role for PtdIns3P in this process.

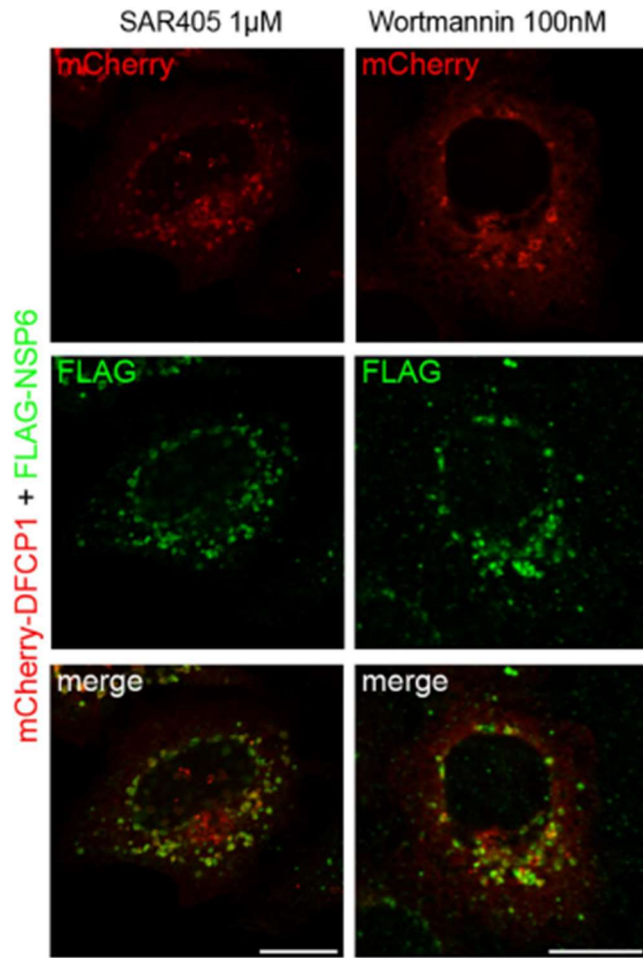


Figure 49. Fluorescent micrographs of cells expressing mCherry-DFCP1 and Flag-NSP6 treated with SAR405 or wortmannin. Anti-Flag immunostaining. Scale bar, 10µm.

In support of an autophagy-independent role of DFCP1 recruitment by NSP6, the number of autophagosomes labeled with an LC3 antibody in cells expressing NSP6 was comparable to that in non-transfected cells (data not shown).

4.14 LDs fuel SARS-CoV-2 replication via the NSP6 protein

LDs, as anticipated in the introduction, play a load-bearing role in the replication of many viruses by supporting their replication and promoting the formation of the replicative complex. In the case of SARS-CoV-2, we found the proximity of

LDs to ROLs, suggesting a role for lipids in the replicative process. To understand whether functional LDs could be "utilized" by ROLs, we expressed NSP3-NSP4 or NSP3-NSP4-NSP6, or NSP6 alone. We assessed the area of individual LDs by staining Bodipy, a fluorescent fatty acid incorporated into LDs.

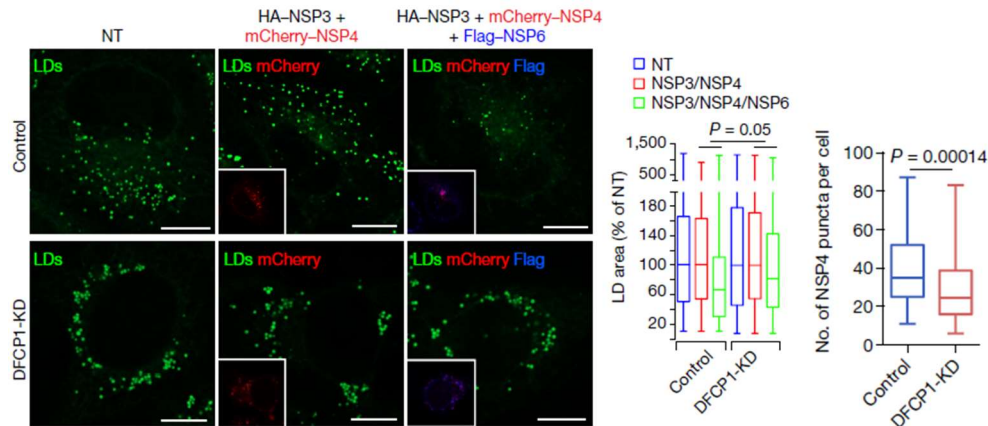


Figure 50. Left, LD staining (BODIPY-488, green) of control (mock-transfected) and DFCP1-knockdown (DFCP1-KD) cells expressing mCherry-NSP4 + HA-NSP3, mCherry-NSP4 + HA-NSP3 + Flag-NSP6 or non-transfected (NT). Insets, mCherry-NSP4 fluorescence (red), and anti-Flag immunostaining (blue). Middle, Graph, quantification of LD area in cells. Values are normalized to the NT-cells in either the control or the DFCP1-KD condition. Right, Number of NSP4 puncta per cell in mCherry-NSP4 + HA-NSP3 + Flag-NSP6-transfected cells without (control) or with DFCP1-KD. Wilcoxon test; unpaired two-tailed Mann-Whitney test. NS, not significant. Box plots represent the 25th to 75th percentiles of the data (center line, median, whiskers, minima, and maxima). Scale bars, 10 μ m.

Specifically, we found that LDs are consumed during ROLS formation in cells expressing NSP3-NSP4-NSP6 and in cells expressing only NSP6, but not in cells expressing NSP3-NSP4. In addition, we used a fluorescent fatty acid incorporated into LDs capable of being metabolized and transferred to different compartments⁹⁷, which shows more efficient transfer to NSP3-NSP4 structures in the presence of NSP6 (data not shown).

This suggests that NSP6 has a role in conveying LD-derived lipids to ROLS. Interestingly, NSP6-dependent LD consumption and ROLS formation were both inhibited by DFCP1 knockdown (Fig. 50).

Finally, consistent with recent reports¹¹³, DFCP1 depletion also inhibited SARS-CoV-2 replication, confirming that LD availability is necessary to sustain viral replication (data not shown).

5. Discussion

As of December 2019, the rapid spread and transmission of Coronavirus Disease-19 (COVID-19) among the world population has reached pandemic proportions affecting all continents, so much so that the epidemic has been declared a global pandemic. In the past two years, most of the research on SARS-CoV-2 has been conducted to understand the mechanism of virus entry, focusing on the binding between the Spike protein and the ACE2 receptor, acting on inhibition of virus-host cell fusion vector binding. In this context, in this work we tried to expand the knowledge about non-structural proteins, known to play a role during viral intracellular pathways, but whose mechanisms are often not well understood. One of the key steps in the SARS-CoV2 cell cycle is replication, a highly organized and poorly understood process. Although the function (as reported in the introduction) of the non-structural proteins that drive the replication and transcription complex is known, little is known about the compartment in which this process occurs: the replication organelle. In particular, when we started our research, the role of NSP3-NSP4 in SARS-CoV2 had not been defined. Instead, it was known for SARS-CoV that both proteins were necessary for DMV. For this reason, we focused on SARS-CoV2 NSP3, NSP4 and especially NSP6 for which we defined a novel role for NSP6 during replication organelle formation. In previous works, NSP6 protein was usually tagged at the C-terminus, showing a diffuse ER localization. By tagging the protein at the N-terminus, we showed that NSP6 was able to induce the formation of roundish or linear structures, colocalizing with the ER reporter protein Cb5. By analyzing the structure of the NSP6 compartment using EM,

immuno-EM, and CLEM techniques, we confirmed that such structures are composed of zippered ER (juxtaposed membranes leaving a small luminal space) and demonstrated that they work as connectors between the ER and DMVs. Furthermore, these NSP6-induced tubules appear to be necessary to organize DMVs and to promote their unique association with the ER.

In addition, we have shown that NSP6 connectors mediate the association of replication organelles with LDs. SARS-CoV-2 is not the only virus to use LDs for replication; in fact, Flaviviruses also recruit LDs to the replicative and assembly compartment, and inhibition of LDs synthesis impairs both replication and virion packaging¹¹⁴.

In the case of SARS-CoV-2, the role of LDs could be in releasing free lipids for membrane biogenesis on the one hand and for expanding the intracellular membrane surface to form DMVs on the other.

In particular, it was shown in the work of Dias et al. (2020) that lipid droplets fuel SARS-CoV-2 replication and that SARS-CoV-2 infection triggers the formation of LDs in several human cell lines. These LDs were found in close apposition with SARS-CoV-2 double-stranded (ds)-RNA in infected Vero cells. Inhibition of LD formation synthesis by targeting DGAT-1 with A922500 blocks SARS-CoV-2 replication⁹⁵.

In this thesis, we characterized this process by unraveling the mechanism of replicative compartment association to LDs by establishing the particular role of NSP6 in mediating this connection. This process is closely linked to the C-terminal amphipathic tail of NSP6 that docks LDs. In fact, the mutant with deletion of the C-terminal part of NSP6 is unable to redistribute to LDs.

We further demonstrated that recruitment of lipids to the DMVs is pivotal for viral replication. These results open a new scenario in the study of the role of lipids in SARS-CoV-2 infection. In the future, a fuller understanding of the role of specific lipids into the biogenesis of the RO could represent a key player to target in the treatment of patients. Moreover, this approach could be translatable

to many other viral pathogens that generate ROs similar to the structures described here for SARS-CoV-2.

The relevance of NSP6 activity in the pathogenesis of SARS-CoV-2 is also demonstrated by the convergent evolution of several viral strains, which appear to be the most virulent, that share the same tri-amino acid deletion in the NSP6 protein¹⁰². Specifically, in this work we have shown that the NSP6(Δ SGF) mutant, which has a deletion of amino acids 106-108 in the second luminal loop of NSP6, (which has undergone convergent evolution in VOCs Alpha, Beta, Gamma, Eta, Iota, and Lambda) has high homodimerization efficiency and increased ER zippering activity. Moreover, the recent and highly infectious BA.2 (omicron) variant also shows a deletion in the second and longer luminal loop of NSP6 (LSGF: 105-108) that harbors a consensus motif of O-glycosylation, which could act as a spacer forming luminal bridges. Therefore, deletion of SGF could also convey increased zippering activity by shortening the 'spacer' and/or preventing its O-glycosylation. This result suggests that the zippering activity of NSP6 could increase and make the replicative rate more efficient, resulting in the most infectious viral strains.

In accordance with what has been demonstrated, abolishing the zippering activity of NSP6 interferes with the replication activity of SARS-CoV-2. Indeed, we have shown that K22, a drug known for its antiviral activity in coronavirus infections, interferes with NSP6 structures in both transfected and infected cells¹⁰⁵. In this work, we characterized NSP6 as a key player in RO formation, suggesting that it might be a promising target to combat COVID-19. This result could represent an important milestone in the treatment of COVID-19, as it provides a potentially actionable new drug and demonstrates that targeting NSP6 activity could be beneficial for the cellular response to infection.

Moreover, in this work, we also determined that NSP6 connectors are inaccessible to all ER proteins that have a large luminal portion. In contrast,

membrane proteins or those with small luminal tracts can cross the connectors, similarly to lipids. This mechanism of action of NSP6 is probably due to safeguarding the formation of DMVs by filtering out proteins that may or may not access the structures, depending on their structure or size. This activity of NSP6 could represent a way of escaping the host cell's protective pathway that would lead to the degradation of the viral genome, among them the activation of the UPR pathway. In mammals, UPR signaling may be mediated by the activation of three signal transducers located in the ER: activating transcription factor 6 (ATF6); double-stranded RNA-activated protein kinase (PKR)-like ER kinase (PERK); and inositol-requiring enzyme 1 (IRE1)¹¹⁵. In our work, we have shown that ATF6 is completely excluded from NSP6 structures, and because each of these proteins has a bulky ER-luminal domain by which ER stress conditions are sensed, it is very likely that PERK and IRE1 are also completely excluded.

Open questions

UPR pathway in SARS-CoV2 infection

In SARS-CoV2 infection, there are discordant works on the activation of ER stress mediated by IRE1, ATF6 or PERK.

Specifically, in the work of Nguyen et al 2022, IRE1 α is activated by autophosphorylation, but its RNase activity fails to cleave XBP1. Suggesting that SARS-CoV2 can control and modulate this pathway to escape the host immune response¹¹⁶. In the work of Echavarria-Consuegra et al., 2021, IRE1 α and ATF6 are activated during infection and their inhibition blocks SARS-CoV2 replication¹¹⁷.

Future studies need to clarify whether and how the UPR pathway may be modulated by SARS-CoV2 infection. It may be possible that in the early stages of infection, to promote the formation of the replication complex and viral RNA

replication there is modulation and inhibition of the pathway. Subsequently, once the replicative rate increases, and the amount of viral protein produced, the host cell tries to deal with the stress and activates a defense response.

Definitely, this stands as a new potential target for implementing anti-COVID-19 drugs. It will be of interest to observe the effect of ER stress induction in our transient transfection cell system of NSP3-4-6, to actively study morphological and structural alterations of DMV compartments and connectors. In addition, future studies will aim to elucidate the accessibility of PERK and IRE1 to NSP6 structures and their subsequent activation.

Role of lipids in RO biogenesis

The characteristic of NSP6 to act as a molecular filter could also select lipids. Indeed, it is reported that many viruses developed numerous strategies to exploit existing lipid signaling, especially to determine the compartmentalization of organelles and their different functions. In fact, RO membrane curvature may be related to either site-specific accumulation of lipids during viral infection, by viral proteins or by exploiting host membrane proteins that induce membrane curvature. Therefore, targeting lipid membrane composition/metabolism could represent relevant targets to inhibit viral infection.

Interestingly, commonly to all *Flaviviridae*, the incorporation of cholesterol in HCV replication membranes may alter the biophysical properties of the membrane and facilitate the assembly of HCV¹¹⁸. Indeed, HCV infection stimulates cellular PI4P production by PI4-kinase III-alpha to promote ROs. In particular, PI4P is recruited to the viral replication site to allow the recruitment of lipid transfer proteins like OSBP and CERT, which may facilitate the enrichment of cholesterol into the membranous web of replication and assembly¹¹⁹⁻¹²¹. In this regard, the use of drugs such as β -cyclodextrins have

been shown to disrupt the structure of the membranous web and inhibit viral replication^{122–124}. Similarly, the use of the chemical inhibitor PIK93 or siRNA of PI4KIII α activity results in the formation of an aberrant replication compartment^{125,126}.

Regarding coronaviruses and particularly SARS-CoV2, it is still unclear what contribution lipids may make to RO biogenesis. The most explored stage of the CoV life cycle has been viral entry, which has been shown to be mediated by the S protein that binds cholesterol to HDL particles, and that uptake of HDL by SR-B1 facilitates viral entry into cells co-expressing the ACE2 receptor¹²⁷.

In addition, cholesterol depletion with methyl- β -cyclodextrins has been shown to decrease viral entry of several coronaviruses, including SARS-CoV-2¹²⁸. It might be interesting to understand how to translate this type of drug treatment to patients to combat COVID-19.

Lipidomic analyses revealed an increase in polyunsaturated glycosphingolipid levels induced by SARS-CoV2 infection, while saturated lipids decreased, suggesting that viral membrane structures require a particularly high level of fluidity. As reported, sphinganine, sphingosine, GA1 and GM3 levels are significantly increased after SARS-CoV2 infection. This specific lipid enhancement seems to be essential for viral replication as it can be inhibited by treatment with glucosylceramide synthase inhibitors^{129–131}. Recently, in the work of Tabata et al. 2021, acyl-glycerophosphate acyltransferases (AGPAT) 1 and 2, two enzymes that catalyze the formation of phosphatidic acid (PA), were found to be recruited on DMVs of SARS-CoV-2 and also HCV. Probably, LPA-PA conversion by AGPATs contributes to negative membrane curvature of DMVs. Importantly, the pharmacological inhibition of PA synthesis impaired HCV and SARS-CoV-2 replication as well as formation of DMVs¹³².

To understand whether the RO compartment is accessible to lipids and whether these play a role in dictating the structure of ROs would be an interesting avenue

of research to pursue. Using the transient transfection system, one can faithfully reproduce the structure of ROs and especially the defects that may arise from inhibition of lipids critical for biogenesis.

Host factors involved in RO biogenesis

In the work of Mingming et al. 2022, it was shown that TMEM41B and VMP1 are required for DMV formation. These two proteins act as ER scramblases that can shuttle between phospholipids in the bilayer membrane.

In particular, VMP1 appears to play a role in the distribution of phosphatidylserine (PS). DMVs generated in VMP1 KO cells are altered, hypothesizing an important role of this protein.

In TMEM41B-deficient cells, altered autophagosome formation, enlarged lipid droplets, and reduced β -oxidation of fatty acids are observed. In the case of SARS-CoV2 infection, TMEM41B KO cells show an altered DMV phenotype, hypothesizing that TMEM41B facilitates ER membrane remodeling to form ROs¹³³.

It will need to be clarified whether these two proteins are necessary as host cofactors in participating in the biogenesis of DMVs or whether their role is related to proper lipid distribution that promotes the structure of DMVs.

Certainly, the missing piece of the puzzle is understanding the lipid and protein composition of DMVs. In the future, immuno-isolation of this compartment and subsequent mass spectrometry and lipidomic analysis may shed light on a little-explored phase of SARS-CoV2. In particular, given the molecular filter function of NSP6, it will be important to understand what contribution it may make to the composition of DMVs and how this may translate to replication step.

In addition, future studies will aim to use an inducible cell system expressing the SARS-CoV2 replicon to examine the host factors and lipid contribution to the replicative process and constitution of DMVs. The choice of the SARS-CoV2

replicon allows, in a transient and more manageable system, to study a much more infection-like context.

As mentioned earlier, TMEM41B plays a role in autophagosome formation. In our work, we demonstrated that DFCEP1, a protein closely involved in the recruitment of autophagy machinery for autophagosome formation, is fully recruited on NSP6 structures. We have, however, shown that the role of DFCEP1 is independent from the autophagy pathway, as mutants of DFCEP1 that are unable to bind PI3P remain recruited to NSP6 structures.

Despite the similarity of the double membrane structure compartment between the autophagosome and DMVs, which might have suggested a common biosynthesis pathway, we did not observe the involvement of the autophagic pathway in our experiments. In fact, inhibition of PI3K, which drives the autophagic process, does not affect at all with the formation of NSP3-4-6 structures. In addition, NSP6 as well as NSP3 and NSP4 show no colocalization with LC3 puncta and do not promote its increase. We cannot exclude the possibility that some other partners involved in autophagy may be used as host factors in viral infection, so further studies will be aimed at clarifying this aspect.

6. Conclusion

The results of the work performed in this thesis have provided solid data on the role of SARS-CoV-2 NSP3 and NSP4 proteins in creating the specialized DMVs that represent the RO where the viral genome is replicated, but more importantly report mechanistic details on the role of NSP6 in this process. Up until now, practically nothing was known about NSP6. Here, I have given insight into its structure and function in promoting the formation of zippered ER membranes as connectors between DMVs and ERs, as observed in infected SARS-CoV-2 cells. NSP6 can organize the development of DMVs in space and time. I also identified host factors that impact on RO formation by refurbishing them with LD-derived lipids. Validation of some of the findings were validated in SARS CoV-2 infected cells.

In addition, NSP6 is promoted as a therapeutic target by inhibiting the formation of zippered structures using a small molecule called K22. This inhibition of the zippering activity of NSP6 results in a decrease and morphological alteration of DMVs, suggesting a pivotal role of NSP6 in the proper biogenesis of this compartment, which has also been confirmed in infected cells. In addition to dissecting aspects of the SARS-CoV-2 life cycle, the high level of conservation of NSP6 in other coronaviruses could provide the possibility to develop broader antiviral therapies.

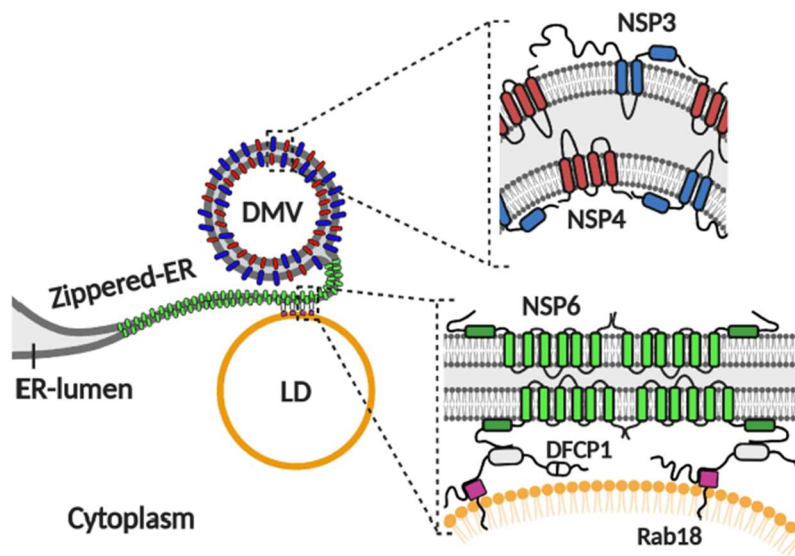


Figure 51. NSP6-induced zippered connectors are cues and organizers for NSP3/NSP4-induced DMV formation acting as selective communication tracks with the ER. In addition, the connectors might also serve as fast tracks to refurbish the actively growing subpopulation of DMVs with lipids derived from LDs.

7. List of publications:

Ricciardi, S., Guarino, A.M., Giaquinto, L. *et al.* The role of NSP6 in the biogenesis of the SARS-CoV-2 replication organelle. *Nature* **606**, 761–768 (2022). <https://doi.org/10.1038/s41586-022-04835-6>

8. Bibliography

1. Woo, P. C. Y. *et al.* Discovery of seven novel Mammalian and avian coronaviruses in the genus deltacoronavirus supports bat coronaviruses as the gene source of alphacoronavirus and betacoronavirus and avian coronaviruses as the gene source of gammacoronavirus and deltacoronavirus. *J Virol* **86**, 3995–4008 (2012).
2. Kuiken, T. *et al.* Newly discovered coronavirus as the primary cause of severe acute respiratory syndrome. *Lancet* **362**, 263–270 (2003).
3. Drosten, C. *et al.* Identification of a novel coronavirus in patients with severe acute respiratory syndrome. *N Engl J Med* **348**, 1967–1976 (2003).
4. Zhu, N. *et al.* A Novel Coronavirus from Patients with Pneumonia in China, 2019. *N Engl J Med* **382**, 727–733 (2020).
5. Donnelly, C. A. *et al.* Epidemiological determinants of spread of causal agent of severe acute respiratory syndrome in Hong Kong. *Lancet* **361**, 1761 (2003).
6. Gorbalenya, A. E. *et al.* The species Severe acute respiratory syndrome-related coronavirus: classifying 2019-nCoV and naming it SARS-CoV-2. *Nat Microbiol* **5**, 536–544 (2020).
7. Lu, R. *et al.* Genomic characterisation and epidemiology of 2019 novel coronavirus: implications for virus origins and receptor binding. *The Lancet* **395**, 565–574 (2020).
8. Guan, Y. *et al.* Isolation and characterization of viruses related to the SARS coronavirus from animals in southern China. *Science* **302**, 276–278 (2003).
9. Zhou, J. *et al.* Human intestinal tract serves as an alternative infection route for Middle East respiratory syndrome coronavirus. *Sci Adv* **3**, (2017).
10. Zhou, P. *et al.* A pneumonia outbreak associated with a new coronavirus of probable bat origin. *Nature* **2020 579:7798 579**, 270–273 (2020).

11. Dong, R., Pei, S., Yin, C., He, R. L. & Yau, S. S. T. Analysis of the Hosts and Transmission Paths of SARS-CoV-2 in the COVID-19 Outbreak. *Genes (Basel)* **11**, 1–16 (2020).
12. Baj, J. *et al.* Clinical Medicine COVID-19: Specific and Non-Specific Clinical Manifestations and Symptoms: The Current State of Knowledge. doi:10.3390/jcm9061753.
13. Wu, F. *et al.* A new coronavirus associated with human respiratory disease in China. *Nature* **2020 579:7798** **579**, 265–269 (2020).
14. Wang, Q. *et al.* Structural Basis for RNA Replication by the SARS-CoV-2 Polymerase. *Cell* **182**, 417-428.e13 (2020).
15. Pachetti, M. *et al.* Emerging SARS-CoV-2 mutation hot spots include a novel RNA-dependent-RNA polymerase variant. *J Transl Med* **18**, (2020).
16. Ogando, N. S. *et al.* The Enzymatic Activity of the nsp14 Exoribonuclease Is Critical for Replication of MERS-CoV and SARS-CoV-2. *J Virol* **94**, (2020).
17. SARS-CoV-2 variants of concern as of 8 December 2022. <https://www.ecdc.europa.eu/en/covid-19/variants-concern>.
18. Zhao, J., Qiu, J., Aryal, S., Hackett, J. L. & Wang, J. The RNA Architecture of the SARS-CoV-2 3'-Untranslated Region. *Viruses* **12**, (2020).
19. Miao, Z., Tidu, A., Eriani, G. & Martin, F. Secondary structure of the SARS-CoV-2 5'-UTR. *RNA Biol* **18**, 447–456 (2021).
20. Wang, D. *et al.* The SARS-CoV-2 subgenome landscape and its novel regulatory features. *Mol Cell* **81**, 2135-2147.e5 (2021).
21. Masters, P. S. The molecular biology of coronaviruses. *Adv Virus Res* **66**, 193–292 (2006).
22. Chen, Y., Liu, Q. & Guo, D. Emerging coronaviruses: Genome structure, replication, and pathogenesis. *J Med Virol* **92**, 418–423 (2020).
23. Khrustalev, V. V. *et al.* Translation-Associated Mutational U-Pressure in the First ORF of SARS-CoV-2 and Other Coronaviruses. *Front Microbiol* **11**, (2020).
24. Gorbalenya, A. E., Koonin, E. v., Donchenko, A. P. & Blinov, V. M. Coronavirus genome: prediction of putative functional domains in the non-structural polyprotein by comparative amino acid sequence analysis. *Nucleic Acids Res* **17**, 4847 (1989).
25. Konno, Y. *et al.* SARS-CoV-2 ORF3b Is a Potent Interferon Antagonist Whose Activity Is Increased by a Naturally Occurring Elongation Variant. *Cell Rep* **32**, (2020).

26. Cubuk, J. *et al.* The SARS-CoV-2 nucleocapsid protein is dynamic, disordered, and phase separates with RNA. *Nature Communications* 2021 12:1 **12**, 1–17 (2021).
27. Ksiazek, T. G. *et al.* A novel coronavirus associated with severe acute respiratory syndrome. *N Engl J Med* **348**, 1953–1966 (2003).
28. Villoutreix, B. O., Calvez, V., Marcelin, A. G. & Khatib, A. M. In Silico Investigation of the New UK (B.1.1.7) and South African (501Y.V2) SARS-CoV-2 Variants with a Focus at the ACE2–Spike RBD Interface. *International Journal of Molecular Sciences* 2021, Vol. 22, Page 1695 **22**, 1695 (2021).
29. Ke, Z. *et al.* Structures and distributions of SARS-CoV-2 spike proteins on intact virions. *Nature* 2020 588:7838 **588**, 498–502 (2020).
30. Inoue, Y. *et al.* Clathrin-dependent entry of severe acute respiratory syndrome coronavirus into target cells expressing ACE2 with the cytoplasmic tail deleted. *J Virol* **81**, 8722–8729 (2007).
31. Knoops, K. *et al.* SARS-Coronavirus Replication Is Supported by a Reticulovesicular Network of Modified Endoplasmic Reticulum. *PLoS Biol* **6**, e226 (2008).
32. Lo, C.-Y. *et al.* Interaction of coronavirus nucleocapsid protein with the 5' and 3' ends of the coronavirus genome is involved in genome circularization and negative-strand RNA synthesis. doi:10.1111/febs.14863.
33. Yan, L. *et al.* Architecture of a SARS-CoV-2 mini replication and transcription complex. *Nature Communications* 2020 11:1 **11**, 1–6 (2020).
34. Ivanov, K. A. *et al.* Multiple Enzymatic Activities Associated with Severe Acute Respiratory Syndrome Coronavirus Helicase. *J Virol* **78**, 5619–5632 (2004).
35. Park, G. J. *et al.* The mechanism of RNA capping by SARS-CoV-2. *Nature* 2022 609:7928 **609**, 793–800 (2022).
36. Lu, S. *et al.* The SARS-CoV-2 nucleocapsid phosphoprotein forms mutually exclusive condensates with RNA and the membrane-associated M protein. *Nat Commun* **12**, (2021).
37. Yao, H. *et al.* Molecular Architecture of the SARS-CoV-2 Virus. *Cell* **183**, 730–738.e13 (2020).
38. Carlson, C. R. *et al.* Phosphoregulation of Phase Separation by the SARS-CoV-2 N Protein Suggests a Biophysical Basis for its Dual Functions. *Mol Cell* **80**, 1092–1103.e4 (2020).

39. Luo, H. *et al.* Severe acute respiratory syndrome coronavirus membrane protein interacts with nucleocapsid protein mostly through their carboxyl termini by electrostatic attraction. *Int J Biochem Cell Biol* **38**, 589 (2006).
40. Arndt, A. L., Larson, B. J., Hogue, B. G. & Program, M. G. A Conserved Domain in the Coronavirus Membrane Protein Tail Is Important for Virus Assembly. *J Virol* **84**, 11418–11428 (2010).
41. Huang, Y., Yang, Z.-Y., Kong, W.-P. & Nabel, G. J. 22 Mailing address: Vaccine Research Center, NIAID, National Institutes of Health, Bldg. 40, Room 4502, MSC 3005, 40 Convent Dr. *J Virol* **78**, 496 (2004).
42. de Haan, C. A. M., Smeets, M., Vernooij, F., Vennema, H. & Rottier, P. J. M. Mapping of the Coronavirus Membrane Protein Domains Involved in Interaction with the Spike Protein. *J Virol* (1999).
43. Yuan, Z. *et al.* The E3 Ubiquitin Ligase RNF5 Facilitates SARS-CoV-2 Membrane Protein-Mediated Virion Release. *mBio* **13**, (2022).
44. Boson, B. *et al.* The SARS-CoV-2 envelope and membrane proteins modulate maturation and retention of the spike protein, allowing assembly of virus-like particles. *J Biol Chem* **296**, (2021).
45. Plescia, C. B. *et al.* SARS-CoV-2 viral budding and entry can be modeled using BSL-2 level virus-like particles. *J Biol Chem* **296**, (2021).
46. Nal, B. *et al.* Differential maturation and subcellular localization of severe acute respiratory syndrome coronavirus surface proteins S, M and E. *J Gen Virol* **86**, 1423–1434 (2005).
47. Sarkar, M. & Saha, S. Structural insight into the role of novel SARS-CoV-2 E protein: A potential target for vaccine development and other therapeutic strategies. *PLoS One* **15**, e0237300 (2020).
48. Venkatagopalan, P., Daskalova, S. M., Lopez, L. A., Dolezal, K. A. & Hogue, B. G. Coronavirus envelope (E) protein remains at the site of assembly. *Virology* **478**, 75–85 (2015).
49. Ye, Y. & Hogue, B. G. Role of the Coronavirus E Viroporin Protein Transmembrane Domain in Virus Assembly. *J Virol* **81**, 3597 (2007).
50. Verdiá-Báguena, C. *et al.* Coronavirus E protein forms ion channels with functionally and structurally-involved membrane lipids. *Virology* **432**, 485–494 (2012).
51. Mandala, V. S. *et al.* Structure and drug binding of the SARS-CoV-2 envelope protein transmembrane domain in lipid bilayers. *Nature Structural & Molecular Biology* **27**:12 **27**, 1202–1208 (2020).

52. Pearson, G. J., Broncel, M., Snijders, A. P. & Carlton, J. G. Exploitation of the Secretory Pathway by SARS-CoV-2 Envelope. *bioRxiv* 2021.06.30.450614 (2021) doi:10.1101/2021.06.30.450614.
53. Huang, Y., Yang, Z., Kong, W. & Nabel, G. J. Generation of Synthetic Severe Acute Respiratory Syndrome Coronavirus Pseudoparticles: Implications for Assembly and Vaccine Production. *J Virol* **78**, 12557 (2004).
54. Griffiths, G. & Rottier, P. Cell biology of viruses that assemble along the biosynthetic pathway. *Semin Cell Biol* **3**, 367–381 (1992).
55. Ruch, T. R. & Machamer, C. E. The Coronavirus E Protein: Assembly and Beyond. *Viruses* **4**, 363 (2012).
56. Ghosh, S. *et al.* b-Coronaviruses Use Lysosomes for Egress Instead of the Biosynthetic Secretory Pathway. doi:10.1016/j.cell.2020.10.039.
57. Saraste, J. & Prydz, K. A New Look at the Functional Organization of the Golgi Ribbon. *Front Cell Dev Biol* **7**, 171 (2019).
58. Romero-Brey, I. & Bartenschlager, R. Membranous Replication Factories Induced by Plus-Strand RNA Viruses. *Viruses* **6**, 2826 (2014).
59. Kujala, P. *et al.* Biogenesis of the Semliki Forest Virus RNA Replication Complex. *J Virol* **75**, 3873 (2001).
60. Gillespie, L. K., Hoenen, A., Morgan, G. & Mackenzie, J. M. The endoplasmic reticulum provides the membrane platform for biogenesis of the flavivirus replication complex. *J Virol* **84**, 10438–10447 (2010).
61. Welsch, S. *et al.* Composition and three-dimensional architecture of the dengue virus replication and assembly sites. *Cell Host Microbe* **5**, 365–375 (2009).
62. Knoops, K. *et al.* SARS-Coronavirus Replication Is Supported by a Reticulovesicular Network of Modified Endoplasmic Reticulum. *PLoS Biol* **6**, e226 (2008).
63. Romero-Brey, I. *et al.* Three-Dimensional Architecture and Biogenesis of Membrane Structures Associated with Hepatitis C Virus Replication. *PLoS Pathog* **8**, e1003056 (2012).
64. Limpens, R. W. A. L. *et al.* The transformation of enterovirus replication structures: a three-dimensional study of single- and double-membrane compartments. *mBio* **2**, (2011).
65. Knoops, K. *et al.* SARS-Coronavirus Replication Is Supported by a Reticulovesicular Network of Modified Endoplasmic Reticulum. *PLoS Biol* **6**, e226 (2008).

66. Cortese, M. *et al.* Integrative Imaging Reveals SARS-CoV-2-Induced Reshaping of Subcellular Morphologies. *Cell Host Microbe* **28**, 853-866.e5 (2020).
67. Snijder, E. J. *et al.* A unifying structural and functional model of the coronavirus replication organelle: Tracking down RNA synthesis. *PLoS Biol* **18**, e3000715 (2020).
68. Klein, S. *et al.* SARS-CoV-2 structure and replication characterized by in situ cryo-electron tomography. *Nature Communications* **2020 11:1** **11**, 1–10 (2020).
69. Melia, C. E. *et al.* The Origin, Dynamic Morphology, and PI4P-Independent Formation of Encephalomyocarditis Virus Replication Organelles. *mBio* **9**, (2018).
70. Snijder, E. J. *et al.* A unifying structural and functional model of the coronavirus replication organelle: Tracking down RNA synthesis. *PLoS Biol* **18**, e3000715 (2020).
71. Wolff, G. *et al.* A molecular pore spans the double membrane of the coronavirus replication organelle. *Science* **369**, 1395–1398 (2020).
72. Klein, S. *et al.* SARS-CoV-2 structure and replication characterized by in situ cryo-electron tomography. *Nature Communications* **2020 11:1** **11**, 1–10 (2020).
73. Snijder, E. J. *et al.* A unifying structural and functional model of the coronavirus replication organelle: Tracking down RNA synthesis. *PLoS Biol* **18**, (2020).
74. Wolff, G., Melia, C. E., Snijder, E. J. & Bárcena, M. Double-Membrane Vesicles as Platforms for Viral Replication. *Trends Microbiol* **28**, 1022–1033 (2020).
75. Oudshoorn, D. *et al.* Expression and Cleavage of Middle East Respiratory Syndrome Coronavirus nsp3-4 Polyprotein Induce the Formation of Double-Membrane Vesicles That Mimic Those Associated with Coronaviral RNA Replication. *mBio* **8**, 1658–1675 (2017).
76. Angelini, M. M., Akhlaghpour, M., Neuman, B. W. & Buchmeier, M. J. Severe Acute Respiratory Syndrome Coronavirus Nonstructural Proteins 3, 4, and 6 Induce Double-Membrane Vesicles. *mBio* **4**, (2013).
77. Roingard, P. *et al.* The double-membrane vesicle (DMV): a virus-induced organelle dedicated to the replication of SARS-CoV-2 and other positive-sense single-stranded RNA viruses. *Cellular and Molecular Life Sciences* **79**, 1–9 (2022).

78. Hagemeyer, M. C. *et al.* Membrane rearrangements mediated by coronavirus nonstructural proteins 3 and 4. *Virology* **458–459**, 125–135 (2014).
79. Lavigne, M. *et al.* SARS-CoV-2 Nsp3 unique domain SUD interacts with guanine quadruplexes and G4-ligands inhibit this interaction. *Nucleic Acids Res* **49**, 7695–7712 (2021).
80. Yang, H. & Rao, Z. Structural biology of SARS-CoV-2 and implications for therapeutic development. *Nat Rev Microbiol* **19**, 685–700 (2021).
81. Lei, J., Kusov, Y. & Hilgenfeld, R. Nsp3 of coronaviruses: Structures and functions of a large multi-domain protein. *Antiviral Res* **149**, 58–74 (2018).
82. Alhammad, Y. M. O. *et al.* The SARS-CoV-2 Conserved Macrodomain Is a Mono-ADP-Ribosylhydrolase. *J Virol* **95**, (2021).
83. Santerre, M., Arjona, S. P., Allen, C. N., Shcherbik, N. & Sawaya, B. E. Why do SARS-CoV-2 NSPs rush to the ER? *J Neurol* **268**, 2013–2022 (2021).
84. Oostra, M. *et al.* Topology and membrane anchoring of the coronavirus replication complex: not all hydrophobic domains of nsp3 and nsp6 are membrane spanning. *J Virol* **82**, 12392–12405 (2008).
85. Gadlage, M. J. *et al.* Murine Hepatitis Virus Nonstructural Protein 4 Regulates Virus-Induced Membrane Modifications and Replication Complex Function. *J Virol* **84**, 280 (2010).
86. Gadlage, M. J. *et al.* Murine hepatitis virus nonstructural protein 4 regulates virus-induced membrane modifications and replication complex function. *J Virol* **84**, 280–290 (2010).
87. Sakai, Y. *et al.* Two-amino acids change in the nsp4 of SARS coronavirus abolishes viral replication. *Virology* **510**, 165 (2017).
88. Cottam, E. M. *et al.* Coronavirus nsp6 proteins generate autophagosomes from the endoplasmic reticulum via an omegasome intermediate. *Autophagy* **7**, 1335–1347 (2011).
89. Cottam, E. M., Whelband, M. C. & Wileman, T. Coronavirus NSP6 restricts autophagosome expansion. *Autophagy* **10**, 1426–1441 (2014).
90. Zhang, Y., Liu, S., Xu, Q., Li, H. & Lu, K. Cleavage of the selective autophagy receptor SQSTM1/p62 by the SARS-CoV-2 main protease NSP5 prevents the autophagic degradation of viral membrane proteins. *Molecular biomedicine* **3**, (2022).
91. Sun, X. *et al.* SARS-CoV-2 non-structural protein 6 triggers NLRP3-dependent pyroptosis by targeting ATP6AP1. *Cell Death & Differentiation* **29:6** **29**, 1240–1254 (2022).

92. Jansen, M. *et al.* Role of ORPs in Sterol Transport from Plasma Membrane to ER and Lipid Droplets in Mammalian Cells. *Traffic* **12**, 218–231 (2011).
93. Kim, D. K. *et al.* A Comprehensive, Flexible Collection of SARS-CoV-2 Coding Regions. *G3 (Bethesda)* **10**, 3399–3402 (2020).
94. Venditti, R. *et al.* Molecular determinants of ER–Golgi contacts identified through a new FRET–FLIM system. *J Cell Biol* **218**, 1055 (2019).
95. da Silva Gomes Dias, S. *et al.* Lipid droplets fuel SARS-CoV-2 replication and production of inflammatory mediators. *PLoS Pathog* **16**, (2020).
96. Venditti, R. *et al.* The activity of Sac1 across ER–TGN contact sites requires the four-phosphate-adaptor-protein-1. *J Cell Biol* **218**, 783 (2019).
97. Rambold, A. S., Cohen, S. & Lippincott-Schwartz, J. Fatty acid trafficking in starved cells: regulation by lipid droplet lipolysis, autophagy, and mitochondrial fusion dynamics. *Dev Cell* **32**, 678–692 (2015).
98. (10) (PDF) A guided tour into subcellular colocalization analysis in light microscopy.
https://www.researchgate.net/publication/282056578_A_guided_tour_into_subcellular_colocalization_analysis_in_light_microscopy.
99. Gilles, J. F., dos Santos, M., Boudier, T., Bolte, S. & Heck, N. DiAna, an ImageJ tool for object-based 3D co-localization and distance analysis. *Methods* **115**, 55–64 (2017).
100. Polishchuk, E. v. & Polishchuk, R. S. Pre-embedding labeling for subcellular detection of molecules with electron microscopy. *Tissue Cell* **57**, 103–110 (2019).
101. Gautier, R., Douguet, D., Antonny, B. & Drin, G. HELIQUEST: a web server to screen sequences with specific alpha-helical properties. *Bioinformatics* **24**, 2101–2102 (2008).
102. Hadfield, J. *et al.* Nextstrain: real-time tracking of pathogen evolution. *Bioinformatics* **34**, 4121–4123 (2018).
103. Venditti, R. *et al.* Molecular determinants of ER–Golgi contacts identified through a new FRET–FLIM system. *J. Cell Biol* **218**, 1055–1065 (2019).
104. Dobson, L., Reményi, I. & Tusnády, G. E. CCTOP: a Consensus Constrained TOPOlogy prediction web server. *Nucleic Acids Res* **43**, W408 (2015).
105. Lundin, A. *et al.* Targeting membrane-bound viral RNA synthesis reveals potent inhibition of diverse coronaviruses including the middle East respiratory syndrome virus. *PLoS Pathog* **10**, (2014).

106. Hartenian, E. *et al.* The molecular virology of coronaviruses. *J Biol Chem* **295**, 12910–12934 (2020).
107. Holwerda, M., V'kovski, P., Wider, M., Thiel, V. & Dijkman, R. Identification of an Antiviral Compound from the Pandemic Response Box that Efficiently Inhibits SARS-CoV-2 Infection In Vitro. *Microorganisms* **2020**, Vol. 8, Page 1872 **8**, 1872 (2020).
108. Lee, J. Y. *et al.* Absolute quantitation of individual SARS-CoV-2 RNA molecules provides a new paradigm for infection dynamics and variant differences. *Elife* **11**, (2022).
109. Thorne, L. G. *et al.* Evolution of enhanced innate immune evasion by SARS-CoV-2. *Nature* **2021** 602:7897 **602**, 487–495 (2021).
110. Gao, G., Sheng, Y., Yang, H., Chua, B. T. & Xu, L. DFCP1 associates with lipid droplets. *Cell Biol Int* **43**, 1492–1504 (2019).
111. Li, D. *et al.* The ER-Localized Protein DFCP1 Modulates ER-Lipid Droplet Contact Formation. *Cell Rep* **27**, 343-358.e5 (2019).
112. Ridley, S. H. *et al.* FENS-1 and DFCP1 are FYVE domain-containing proteins with distinct functions in the endosomal and Golgi compartments. *J Cell Sci* **114**, 3991–4000 (2001).
113. Twu, W. I. *et al.* Contribution of autophagy machinery factors to HCV and SARS-CoV-2 replication organelle formation. *Cell Rep* **37**, (2021).
114. Samsa, M. M. *et al.* Dengue virus capsid protein usurps lipid droplets for viral particle formation. *PLoS Pathog* **5**, (2009).
115. Hiramatsu, N., Joseph, V. T. & Lin, J. H. Monitoring and Manipulating Mammalian Unfolded Protein Response. *Methods Enzymol* **491**, 183 (2011).
116. Nguyen, L. C. *et al.* SARS-CoV-2 diverges from other betacoronaviruses in only partially activating the IRE1 α /XBP1 ER stress pathway in human lung-derived cells. *bioRxiv* (2022) doi:10.1101/2021.12.30.474519.
117. Echavarría-Consuegra, L. *et al.* Manipulation of the unfolded protein response: A pharmacological strategy against coronavirus infection. *PLoS Pathog* **17**, e1009644 (2021).
118. Deng, Y., Almsherqi, Z. A., Ng, M. M. L. & Kohlwein, S. D. Do viruses subvert cholesterol homeostasis to induce host cubic membranes? *Trends Cell Biol* **20**, 371–379 (2010).
119. Peretti, D., Dahan, N., Shimoni, E., Hirschberg, K. & Lev, S. Coordinated lipid transfer between the endoplasmic reticulum and the Golgi complex requires

- the VAP proteins and is essential for Golgi-mediated transport. *Mol Biol Cell* **19**, 3871–3884 (2008).
120. Targeting Lipid Metabolism in the Treatment of Hepatitis C Virus Infection on JSTOR. <https://www.jstor.org/stable/30087700>.
 121. Sakamoto, H. *et al.* Host sphingolipid biosynthesis as a target for hepatitis C virus therapy. *Nat Chem Biol* **1**, 333–337 (2005).
 122. Sagan, S. M. *et al.* The influence of cholesterol and lipid metabolism on host cell structure and hepatitis C virus replication. *Biochem Cell Biol* **84**, 67–79 (2006).
 123. Aizaki, H. *et al.* Critical Role of Virion-Associated Cholesterol and Sphingolipid in Hepatitis C Virus Infection. *J Virol* **82**, 5715 (2008).
 124. Amako, Y., Sarkeshik, A., Hotta, H., Yates, J. & Siddiqui, A. Role of Oxysterol Binding Protein in Hepatitis C Virus infection †. *J Virol* **83**, 9237–9246 (2009).
 125. Tai, A. W. & Salloum, S. The Role of the Phosphatidylinositol 4-Kinase PI4KA in Hepatitis C Virus-Induced Host Membrane Rearrangement. *PLoS One* **6**, e26300 (2011).
 126. Berger, K. L., Kelly, S. M., Jordan, T. X., Tartell, M. A. & Randall, G. Hepatitis C Virus Stimulates the Phosphatidylinositol 4-Kinase III Alpha-Dependent Phosphatidylinositol 4-Phosphate Production That Is Essential for Its Replication. *J Virol* **85**, 8870–8883 (2011).
 127. Wei, C. *et al.* HDL-scavenger receptor B type 1 facilitates SARS-CoV-2 entry. *Nature Metabolism* **2020 2:12** **2**, 1391–1400 (2020).
 128. Bezerra, B. B. *et al.* Hydroxypropyl-beta-cyclodextrin (HP-BCD) inhibits SARS-CoV-2 replication and virus-induced inflammatory cytokines. *Antiviral Res* **205**, 105373 (2022).
 129. Torretta, E. *et al.* Severity of covid-19 patients predicted by serum sphingolipids signature. *Int J Mol Sci* **22**, (2021).
 130. Vitner, E. B., Avraham, R., Politi, B., Melamed, S. & Israely, T. Elevation in sphingolipid upon SARS-CoV-2 infection: possible implications for COVID-19 pathology. *Life Sci Alliance* **5**, (2022).
 131. Vitner, E. B. *et al.* Glucosylceramide synthase inhibitors prevent replication of SARS-CoV-2 and influenza virus. *J Biol Chem* **296**, (2021).
 132. Tabata, K. *et al.* Convergent use of phosphatidic acid for hepatitis C virus and SARS-CoV-2 replication organelle formation. *Nature Communications* **2021 12:1** **12**, 1–15 (2021).

133. Ji, M. *et al.* VMP1 and TMEM41B are essential for DMV formation during β -coronavirus infection. (2022) doi:10.1083/jcb.202112081.

9. List of tables and figures

Table 1. Summary of VOIs described in the last year.	9
Table 2. Summary of VOCs described in the last year.	9
Figure 1. The RNA genome encodes NSPs, structural and accessory proteins. The nonstructural proteins are encoded by ORF1a and ORF1b. Cap-dependent translation begins at ORF1a and produces pp1a, formed by NSP1–11, or pp1ab, a more extended polypeptide that includes NSP12–16. The structural and accessory proteins are synthesized by translating their respective subgenomic mRNAs. Reprinted from “Replication of the coronavirus genome: A paradox among positive-strand RNA viruses”, Grellet <i>et al.</i> , 2021, <i>Journal of biological chemistry</i>	10
Figure 2. Schematic representation of SARS-CoV2 life cycle: Entry, Replication, Assembly and Egress. A, The coronavirus virion is composed of structural proteins: spike (S), envelope (E), membrane (M), nucleocapsid (N). Inside the capsid is located the single-stranded positive RNA genome. B, Entry is mediated by S interactions with cellular receptors such as angiotensin-converting enzyme 2 (ACE2), together with host factors (such as the cell surface serine protease TMPRSS2) or through the endosomal pathway. Once entered, the genome is released into the cytosol and genomic RNA is immediately translated into ORF1a and ORF1b from which the polyproteins pp1a and pp1ab are derived. Pp1a and pp1ab are processed into the individual nonstructural proteins (NSPs) that form the viral replication and transcription complex. The nsps direct the biogenesis of the viral replication organelles, the double membrane vesicles (DMVs). The translated structural proteins translocate to the ER-Golgi intermediate compartment (ERGIC), where RNA is encapsidated within the virion. Finally, virions are secreted from the infected cell by exocytosis. Reprinted from the “Coronavirus biology and replication: implications for SARS-CoV-2”, V’kovski <i>et al.</i> , 2020, <i>nature reviews microbiology</i>	12
1.3.1 Entry	12
Figure 3. SARS-CoV-2 Spike protein binds to the angiotensin-converting enzyme 2 (ACE2) to enter target cells. After receptor binding (1), the virus S protein is cleaved by proteases such as furin/TMPRSS2 into S1 and S2 subunits (2) that mediates S2-assisted fusion (3) and the release of the viral genome (4)—reprinted from “In silico investigation of the new UK (B.1.1.7) and South African (501Y.V2) SARS-CoV-2 variants with a focus at the ACE2-Spike RBD interface”, by Villoutreix <i>et al.</i> , 2021, <i>International Journal of Molecular Sciences</i>	14
Figure 4. Structures of pre-fusion and post-fusion trimers of the S protein. (b) Possible conformations of the pre-fusion trimer. It is reprinted from “Structures and distributions of SARS-CoV-2 spike proteins on intact virions”, by Ke, Z., <i>et al.</i> , 2020, <i>Nature</i> , 588, 498–502.	15

Figure 5. Entry of SARS-CoV-2. Membrane fusion, upon binding to the host cell receptor ACE2, the SARS-CoV-2 spike protein can be cleaved at the S1/S2 site by furin, which leads to conformational changes that expose the S2' site for cleavage by TMPRSS2, that results in viral-human cell fusion at the plasma membrane. Endocytosis, if separation of both sites does not occur at the cell surface after receptor binding, the virion may be endocytosed. Cathepsins within the endosome or lysosome can then cleave the spike protein to activate the spike protein and, then, the membrane fusion. Reprinted from “Cell entry by SARS-CoV-2”, by Peng et al., 2021, Trends in Biochemical Sciences..... 15

Figure 6. Discontinuous transcription. The RdRp complex initiates transcription at the 3' end of the positive-sense genome (1). Upon copying the TRS-B sequence (2), the RdRp complex may “jump” to the TRS-L sequence (3) owing to the complementarity between the TRS-B sequence on the nascent sg RNA and the end TRS-L sequence on the genome. Transcription is resumed on the new template, and the leader sequence (shown in red) is copied to complete the negative-strand sg RNA. The RdRp complex does not always switch templates at TRS-B sequences, resulting in the synthesis of genome-length negative-strand RNA. The negative-strand RNAs serve as templates for synthesizing genome-length positive-strand RNAs or sg mRNAs. Reprinted from “The molecular virology of coronaviruses” by Hartenian et al., 2020, JCB Review. 17

Figure 7. Shown is a model of how the different proteins in the coronavirus replisome come together on the viral negative-strand while synthesizing the positive-strand RNA. The core replicase is predicted to consist of the RdRp (NSP12), processivity factors (NSP7-8), and ExoN complex (NSP14, NSP10). The helicase is shown to be unwinding the dsRNA ahead of the replisome, and the SSB (NSP9) is shown as a dimer protecting single-stranded regions of the RNA. The 29-O-MTase (NSP16), which is predicted to be involved in RNA capping, is also indicated. Reprinted from “The molecular virology of coronaviruses” by Hartenian et al., 2020, JCB Review. 18

Figure 8. The sequential enzymatic action performed during viral mRNA 5' capping. NSP13 removes the 5'γ-phosphate from the 5' nucleotide generating the ppN-RNA; a GTase adds GMP to the 5'-terminus of ppN-RNA; NSP10 and NSP14 cooperate to add a methyl group to form the cap0 structure; NSP10 and NSP16. Methyl donor group: S-adenosyl methionine (SAM). Reprinted from “A Structural View of SARS-CoV-2 RNA Replication Machinery: RNA Synthesis, Proofreading and Final Capping”, Romano, M., et al., 2020, Cells, 9(5), 1267. 19

Figure 9. Schemes and membrane topology of the structural SARS-CoV-2 proteins nucleoprotein (N) (A), membrane (M) (B), viroporin envelope (E) (C), and spike (S). Reprinted from “Betacoronavirus Assembly: Clues and Perspectives for Elucidating SARS-CoV-2 Particle Formation and Egress” by Bracquemond et al., 2021, American Society for microbiology”. 23

Figure 10. Egress of the CoV viral particles. Lower panel: After the replication of mRNAs in the DMVs, viral structural proteins mediate the formation of viral-like particles (VLP). Vesicle accumulation occurs at the intermediate compartment membranes and then is released to the extracellular space via 3 different routes. Reprinted from “The life cycle and enigmatic egress of coronaviruses”, by Prydz et al., 2022, Molecular Microbiology..... 25

Figure 11. Invaginated spherules and double-membrane vesicles (DMVs) by electron tomography. Reprinted from “Multiscale Electron Microscopy for the Study of Viral Replication Organelles”, by Wolff et al., 2021, <i>Viruses</i>	26
Figure 12. Pathways hypothesized for the formation of Double-Membrane Vesicle (DMV) and Representative 3D Models. Path1, possible intermediates observed during Picornavirus infection. Path2, hypothetical intermediates observed during Nidovirus infection. Reprinted from "Double-Membrane Vesicles as Platforms for Viral Replication," by Wolff et al., 2020, <i>Trends in Microbiology</i>	29
Figure 13. HeLa cells expressing YFP-Cb5 alone, co-expressing C- or N-terminally Flag-tagged NSP6, or co-expressing untagged NSP6. Insets, enlarged merged images of boxed areas; arrowheads, NSP6 compartments; dashed lines, cell boundaries. Scale bars, 10 μ m.	45
Figure 14. HeLa cells transfected with Flag-NSP6 immunostained with anti-Flag, lysosome marker (anti-LAMP1), endosome, and autophagosome marker (anti-EEA1 or anti-LC3). Scale bars, 10 μ m.	46
Figure 15. Fluoromicrographs of HeLa cells expressing YFP-Cb5 and either IBV NSP6-Flag (upper panels) or IBV-Flag-NSP6 (lower panels). Cells immunostained with anti-Flag antibody (red). Scale bars, 10 μ m.	47
Figure 16. Left, IEM (anti-haemagglutinin (HA) immunolabelling) and EM of HeLa cells expressing HA-NSP6. White arrowheads, linear zippered ER membranes; black arrowheads, circular zippered ER membranes; black arrows, continuity between zippered and regular ER membranes. The regular ER is shown in green. The average size of circular NSP6-positive ER structures is 623 ± 231 nm. Right, Morphometric analysis of NSP6-expressing cells (percentage of the ER surface associated with regular cisternae or zippered domains). Mean \pm s.d. Scale bars, 120 nm. Experiments were performed by Roman and Lena Polishchuk.....	48
Figure 17. Upper, Immuno-CLEM analysis of the NSP6 compartments. Fluoromicrograph of HA-NSP6. With the enlargement of NSP6-labelled structures 1–7 that were identified on EM serial sections. Bottom, Serial sections of structure 6. Black arrows, NSP6-positive linear zippered membrane connections with ER cisternae. White arrows, NSP6-positive circular zippered structures. Scale bars, 4 μ m (Upper, left); 1.1 μ m (Upper, middle and right); 250 nm (Bottom). Experiments were performed by Lena Polishchuk.....	49
Figure 18. Fluoromicrographs of HeLa cells expressing CLRT-mCherry, GFP- KDEL, GFP-ERGIC53, GFP-ATF6, GFP-ATL2, GFP-KDEL alone (left panel) or with GFP-NSP6 and mCherry-NSP6 (middle and right panel). Small panels, enlargements of boxed areas, and arrowheads indicate co-localization. Scale bars, 10 μ m.	50
Figure 19. HeLa cells expressing C-terminal or N-terminal Flag-tagged NSP6 immunostained with anti-Flag antibody and an antibody against a luminal epitope of TGN46 after permeabilization with digitonin and subsequently with Triton-X-100. Scale bar, 10 μ m. Experiment performed by Andrea Maria Guarino.....	52
Figure 20. Left, Predicted secondary structure of NSP6. The Δ SGF deletion and truncation site (at residue 157) are indicated. Right, Model of the amphipathic helix of NSP6 according to HELIQUEST. Apolar residues are in yellow, and polar residues and	

glycine have been given different colors. The arrow indicates the hydrophobic moment ($\mu H = 0.409$). Numbers indicate the amino acid positions of the NSP6 protein.....53

Figure 21. Upper, HeLa cells untransfected (left panel) or expressing Myc-NSP6 were immunostained for VAP-A or Myc. Insets show the Myc-NSP6 signal. The number indicates the fraction of VAP-A associated with the NSP6 structures. Mean \pm SD. Middle, HeLa cells expressing Myc-NSP6 (inset) and/or Flag-NSP6(1-157). The fraction of NSP6 (1-157) associated with NSP6 structures is indicated. Mean \pm s.d. Bottom (left), Model of the F220Q/T222W NSP6 mutant helix ($\mu H = 0.191$) according to HELIQUEST. Mutations that abolish the amphipathic character of the helix are in red. Bottom (right), HeLa cells expressing GFP-NSP6 F220Q/T222W mutant. Scale bar, 10 μm54

Figure 22. Left, Immunoprecipitation (IP) and western blot (WB) from GFP-NSP6 and HA-NSP6 co-expressing cells. Right, Cell lysates (input) and immunoprecipitates (IP, with anti-HA or anti-Flag antibodies) from HeLa cells, untransfected or expressing the indicated NSPs were analyzed by western blot with anti-HA, anti-Flag, or anti-GFP antibodies as appropriate. Images are representative of three independent experiments. Experiment performed by Giuseppe Di Tullio.....55

Figure 23. Left, Fluoromicrographs of HeLa cells expressing GFP-NSP6(1-157) alone or with mCherry-NSP6. Right, Cell lysates (input) and immunoprecipitates (IP, with anti-HA or anti-Flag antibodies) from HeLa cells, untransfected or expressing the indicated NSPs were analyzed by western blot with anti-HA, anti-Flag, or anti-GFP antibodies as appropriate Scale bar, 10 μm . WB experiment was performed by Giuseppe Di Tullio.56

Figure 24. Stably transfected Flag-NSP6 clone induced with doxycycline and treated with DMSO or K22 for 24 h. K22 reduced the number of NSP6 structures and resulted in elongated structures in a percentage of the cells (right panel, number of cells exhibiting these structures. Mean \pm SD). Two-tailed unpaired t-test with Welch's correction. Scale bars, 10 μm . Experiment performed by Laura Giaquinto.57

Figure 25. Immuno-CLEM of HA-NSP6-expressing cells treated with K22 for 24 h. Right, Fluoromicrograph showing NSP6 (anti-HA immunostaining) in elongated structures (arrows 1, 2) close to the nucleus (asterisk). Scale bars, 7.5 μm , inset 200 nm. Experiment performed by Lena Polishchuk.57

Figure 26. Left, Radial layout of a phylogenetic tree of 3,508 SARS-CoV-2 genomes. VOCs are indicated, and the percentage of each genome containing Δ SGF is reported. Black branches highlight the appearance of the deletion. Right, Mutations are involved in the branching and specificity of each VOC. Arrows, the appearance of the Δ SGF, and mutations in the spike (S) protein. Experiments were performed by Francesco Panariello.....58

Figure 27. Left, Time course analysis of stably expressing Flag-NSP6 or Flag-NSP6(Δ SGF) cells induced with doxycycline. Fluoromicrographs at 3-5-8-24 h. Right, Quantification of the NSP6-structures. Upper number and areas of NSP6-positive structures. Bottom, NSP6 in structures as a percentage of the total NSP6 in the cell (mean \pm s.e.m.). Scale bars, 10 μm . Experiments were performed by Laura Giaquinto.59

Figure 28. Cell lysates (input) of cells expressing GFP-NSP6 with HA-NSP6, or GFPNSP6 (Δ SGF) with HA-NSP6(Δ SGF), were immunoprecipitated (IP) with anti-HA antibody and analyzed by western blot with anti-HA and anti-GFP antibodies. The graph shows the co-IP efficiency of NSP6 (Δ SGF) relative to NSP6, which was set as 1. Mean \pm SEM, Two-tailed unpaired t-test with Welch's correction. Experiments were performed by Andrea Maria Guarino and Giuseppe Di Tullio.60

Figure 29. Doxycycline-induced clone expressing Flag-NSP6 (Δ SGF) treated with DMSO or K22 for 24 h. A number of NSP6 structures (middle panel) and cells with elongated NSP6 structures (right panel) induced by K22. The number indicates the percentage (Mean \pm SD) of cells exhibiting the elongated structures. Single values are plotted, Means \pm SEM is shown, and a two-tailed unpaired t-test with Welch's correction. Scale bars, 10 μ m. Experiments were performed by Laura Giaquinto.....60

Figure 30. EM (Upper) and IEM (Middle) anti-HA immunolabelling of HA-NSP6(Δ SGF)-expressing HeLa cells. White arrowheads, linear zippered ER structures; black arrowheads, circular zippered ER structures. The regular ER is shown in green. Upper (Right), Morphometric analysis of IEM images. Quantification of gold particles at zippered ER. Middle (Right), the surface area of zippered ER normalized for the total number of gold particles. Bottom, Immuno-CLEM of cells expressing HA-NSP6(Δ SGF) with inset. and IEM, in which arrows 1–4 indicate overlap of the fluorescent an immuno-gold signals in the zippered NSP6-positive-structures. g, magnification of the structure indicated by arrow 1. Scale bars, 250 nm; 3.7 μ m; 480 nm; 250 nm. Unpaired two-tailed t-test. Experiments were performed by Roman and Lena Polishchuk.61

Figure 31. Upper, Fluoromicrographs of HeLa cells expressing YFP-Cb5 with HA-NSP3 (anti-HA immunostaining) or mCherry-NSP4. Insets merge with YFP-Cb5. Upper (right), Western blot (WB) of total lysates from HeLa cells expressing HA-NSP3, mCherry-NSP4, Flag-NSP6, or GFP as indicated. Actin was used as a loading control. Middle, Fluoromicrographs of HeLa cells expressing HA-NSP3 and mCherry-NSP4. Insets, enlargement of the boxed area. Arrowheads, NSP3/NSP4-positive structures. Dashed lines delineate cell boundaries. Bottom, IEM of HeLa cells co-transfected with HA-NSP3 and mCherry-NSP4. Anti-HA labeling shows gold particles decorating DMVs, indicated by asterisks. Black arrows, ER. Inset, magnification of boxed area. White arrows in d and e show double membranes. The average DMV size is 92 ± 30 nm. Scale bars, 10 μ m.63

Figure 32. Upper, Individual fluoromicrographs of a Calu-3 cell co-transfected with Flag-NSP6, HA-NSP3, and mCherry-NSP4. Bottom, The enlargement of the boxed area shows HA and Flag immunolabelling. Bottom, (right), Western blot of total lysates from HeLa cells expressing HA-NSP3, mCherry-NSP4, or Flag-NSP6 as indicated. Actin was used as a loading control. Scale bars, 10 μ m.....64

Figure 33. Calu-3 cells infected with early lineage and Gamma variant SARS-CoV-2. Values represent mean NSP3- and NSP6-structure distances in nm. Scale bars, 10 μ m.65

To analyze the morphology of the structures detected by immunofluorescence, CLEM was performed on cells co-expressing HA-NSP3, mCherry-NSP4, and GFP-NSP6. The dots of NSP3-NSP4 corresponded to clusters of DMVs, while the structures of NSP6

corresponded to zippered ER tracts, which were distinct but often close and connected to DMVs (Fig. 34).65
 Figure 34. Left Fluoromicrograph and Right EM serial section of an HA–NSP3 + mCherry–NSP4 + GFP–NSP6–expressing cell. Arrowheads, NSP3/NSP4 co-localization; arrows, NSP6 compartments; black arrow, NSP6 compartment connection with NSP3/NSP4 DMVs. Scale bars, 10 μ m (a); 470 nm (b). Experiments were performed by Lena Polishchuk.....66
 Figure 35. Upper Number, and distribution of NSP4 puncta in cells expressing the indicated NSPs. Tomogram (Bottom) and three-dimensional (3D) reconstruction showing connections of zippered ER to DMVs (white arrow and arrowhead) and the regular ER (black arrow). Box plots represent the 25th to 75th percentiles of the data. Scale bars, 160 nm. One-way ANOVA with Tukey’s or Emmeans posthoc test. Tomographic analysis was performed by Roman Polishchuk.67
 Figure 36. Upper Tomograms and 3D reconstruction showing multiple short DMV–ER tubular connections (white arrows) in an NSP3/NSP4-expressing cell. Bottom, Tomograms from NSP3/NSP4 and NSP3/NSP4/NSP6-expressing cells showing DMV–ER connections (arrows). Bottom middle, Intensity profiles along the red lines., Bottom right, Morphometry of NSP3/NSP4- or NSP3/NSP4/NSP6-expressing cells. Scale bars, 160 nm; 100 nm. Unpaired two-tailed t-test. Tomographic analysis was performed by Roman Polishchuk.68
 Figure 37. Upper, Tomographic slice of a HeLa cell expressing HA-NSP3/mCherry-NSP4 or HA-NSP3/mCherry-NSP4/Flag-NSP6, showing DMV clusters with regular round DMVs (white arrows) and large and elongated DMVs (black arrows). Upper right, Length of DMV–ER tubular or zippered connections in NSP3/NSP4 or in NSP3/NSP4/NSP6-expressing cells, respectively. Single values are plotted. Medians are shown ($n \geq 14$ connections), two-tailed unpaired t-test. Middle graph, DMV densities were calculated in tomograms as the number of vesicles per μ m³ in a volume occupied by a DMV cluster; Single values are plotted, Median is shown, and a two-tailed unpaired t-test. Bottom graph, Frequency histograms of DMV diameter measured from tomograms of cells expressing NSP3/NSP4 (average diameter 80.87 nm) or NSP3/NSP4/NSP6 (average diameter 67.50 nm). Nonparametric Kolmogorov-Smirnov (KS) test. $n \geq 135$ vesicles. Scale bar, 180 nm. Experiment performed by Roman Polishchuk.....69
 Figure 38. Upper, HeLa cells transfected with HA-NSP3 and mCherry-NSP4 for 5 h were further transfected or not with Flag-NSP6 and treated with DMSO or K22 (40 μ M, 16 h) followed by immunostaining as indicated. Bottom, Quantification of the number of NSP4 puncta/cell. Single values are plotted. The median value is shown. One-way ANOVA test with Tukey’s posthoc. ns, not significant. Scale bar, 10 μ m.71
 Figure 39. CLEM analysis of K22-treated cells. Upper, Fluoromicrograph of HeLa cell expressing HA-NSP3, mCherry-NSP4, and Myc-NSP6. The inset corresponds to the boxed area and shows NSP3/NSP4-positive structures (arrows) close to the NSP6 compartment (arrowhead). The NSP6 compartment corresponds to a circular zippered ER structure (arrowhead) close to but not connected with the NSP3/NSP4 puncta that correspond to DMVs (arrows). The empty arrow indicates a tubular connection of a DMV to the regular ER (magnified in the inset). Middle, Ultrastructure of DMV clusters

in K22-treated cells expressing HA-NSP3, mCherry-NSP4, and Myc-NSP6. Serial sections show a DMV cluster with irregular elongated DMVs (black arrows). The empty arrow indicates a tubular connection of a DMV with a regular ER. Bottom, Morphometric analysis of serial sections from untreated (NT) and K22-treated cells to quantify the number of DMVs per cluster, DMV shape factor, and the number of tubular or zippered connections per DMV cluster. Single values are plotted, Medians are shown, and two-tailed unpaired t-tests. scale bar, 4.4 μm ; 370 nm; 320 nm. CLEM analysis was performed by Lena Polishchuk.....72

Figure 40. Antiviral activity of K22. Calu-3 cells infected with SARS-CoV-2 without (left panels) or with (right panel) K22 treatment. Right, cells were immunostained for dsRNA and NSP6. Nuclei were stained with DAPI. Scale bar, 20 μm . Experiment was performed by Patricia Bozza.....73

Figure 41. Upper, Tomogram and 3D reconstruction of an NSP3/NSP4/NSP6(Δ SGF)-expressing cell, showing numerous zippered ER domains connected to DMVs (white arrows) and regular ER (black arrows). Bottom, quantification of the number of ER zippered connections per DMV cluster and number of DMVs per cluster. Single values are plotted, and Medians are shown. Bottom right, Frequency histograms of DMV diameter measured from tomograms of cells expressing NSP3/NSP4/NSP6 (average diameter 67.50 nm) or NSP3/NSP4/NSP6(Δ SGF) (average diameter 68.51 nm). The histograms were analyzed using the non-parametric Kolmogorov-Smirnov (KS) test. $n \geq 123$ vesicles. Two-tailed unpaired t-test. Scale bar, 160 nm. Tomographic analysis was performed by Roman Polishchuk.....74

Figure 42. Left, Tomograms showing zippered ER connections (arrows) to DMVs in Calu-3 cells infected with early lineage and Gamma variant SARS-CoV-2. Right, Length of zippered ER connected to DMVs in infected cells ($N = 10$, $n \geq 20$), and from early lineage* (Bavpat1/2020) data in EMPIAR-10490 (29 tomograms). Scale bars, 200 μm . EM analysis was performed by Roman Polishchuk.....75

Figure 43. Fluoromicrographs of HeLa cells expressing Flag-NSP6-C80 (i.e., the last 80 amino acids of NSP6). Anti-Flag antibody and staining for LDs using BODIPY C12. Insets, enlargement of boxed areas. Arrowheads, colocalizing structures. Scale bars, 10 μm76

Figure 44. NSP6-C80 mutated in residues that abrogate the amphiphilic properties of the AH fail to associate with LDs. Cells were immunostained with anti-Flag Ab (green) and BODIPY-DA-C12 (red). Scale bars, 10 μm76

Figure 45. Left, HeLa cells expressing the indicated NSPs stained with BODIPY-488 for LDs (green). Insets, enlargement of the boxed area; arrowheads, LDs close to ROLS (left) to NSP6 (right). Bottom panels and green circles delineate the position of LDs. Right, the Distance of LDs from NSP4 and NSP6 puncta was measured in whole cells expressing the indicated NSPs. LD to NSP4 puncta. Scale bars, 10 μm , Box plots represent the 25th to 75th percentiles of the data (center line, median; whiskers, minima, and maxima).....77

Figure 46. HeLa cells expressing GFP-DFCP1 alone or with mCherry-NSP4 + HA-NSP3 + Flag-NSP6. Arrowheads, DFCP1 signal in the NSP6 compartment. Bottom, Individual fluoromicrographs and merge of cells co-expressing GFP-DFCP1, mCherry-NSP4, and HA-NSP3 (anti-HA immunostaining). Scale bars, 10 μm78

Figure 47. Fluoromicrographs of cells co-expressing GFP-DFCP1 and Flag-NSP6(1–157). Scale bar, 10µm.	79
Figure 48. Fluorescent images of HeLa cells transfected with the indicated DFCP1 mutants alone or in combination with NSP6 (as shown). A schematic representation of DFCP1 mutants is reported on top. Arrowheads, DFCP1 signal in the NSP6 compartment. Insets, an enlarged merge of boxed areas. Numbers indicate the percentage of colocalization between DFCP1 mutants and NSP6. Mean ± SD. Scale bar, 10µm.	80
Figure 49. Fluorescent micrographs of cells expressing mCherry-DFCP1 and Flag-NSP6 treated with SAR405 or wortmannin. Anti-Flag immunostaining. Scale bar, 10µm.	81
Figure 50. Left, LD staining (BODIPY-488, green) of control (mock-transfected) and DFCP1-knockdown (DFCP1-KD) cells expressing mCherry-NSP4 + HA-NSP3, mCherry-NSP4 + HA-NSP3 + Flag-NSP6 or non-transfected (NT). Insets, mCherry-NSP4 fluorescence (red), and anti-Flag immunostaining (blue). Middle, Graph, quantification of LD area in cells. Values are normalized to the NT-cells in either the control or the DFCP1-KD condition. Right, Number of NSP4 puncta per cell in mCherry-NSP4 + HA-NSP3 + Flag-NSP6-transfected cells without (control) or with DFCP1-KD. Wilcoxon test; unpaired two-tailed Mann-Whitney test. NS, not significant. Box plots represent the 25th to 75th percentiles of the data (center line, median, whiskers, minima, and maxima). Scale bars, 10 µm.	82
Figure 51. NSP6-induced zippered connectors are cues and organizers for NSP3/NSP4-induced DMV formation acting as selective communication tracks with the ER. In addition, the connectors might also serve as fast tracks to refurbish the actively growing subpopulation of DMVs with lipids derived from LDs.	92